Texas A&M University
Mechanical Engineering Department
Turbomachinery Laboratory
Tribology Group

A FE MODEL FOR STATIC LOAD IN TILTING PAD JOURNAL BEARINGS WITH PAD FLEXIBILITY

Research Progress Report to the TAMU Turbomachinery Research Consortium

TRC-B&C-02-2014

By

Yingkun Li
Graduate Research Assistant

Luis San Andrés
Mast-Childs Chair Professor
Principal Investigator

November 2014

COMPUTATIONAL MODEL FOR TILTING PAD JOURNAL BEARINGS
TEES Project 32513/15196B

EXECUTIVE SUMMARY

A FE Model for Static Load in Tilting Pad Journal Bearings with Pad Flexibility

Yinkun Li and Luis San Andrés

Tilting pad journal bearings (TPJBs) supporting high performance turbomachinery rotors have undergone steady design improvements to satisfy ever stringent operating conditions that include large specific loads, due to smaller footprints, and high surface speeds that promote flow turbulence and hence larger drag power losses. Simultaneously, predictive models continuously evolve to include minute details on bearing geometry, pads and pivots' configurations, oil delivery systems, etc. In general, predicted TPJB rotordynamic force coefficients correlate well with experimental data for operation with small to moderately large unit loads (1.7 MPa). Experiments also demonstrate bearing dynamic stiffnesses are frequency dependent, best fitted with a stiffness-mass like model whereas damping coefficients are adequately represented as of viscous type. However, for operation with large specific loads (> 1.7 MPa), poor correlation of predictions to measured force coefficients is common. Recently, an experimental effort [1] produced test data for three TPJB sets, each having three pads of unequal thickness, to quantify the effect of pad flexibility on the bearings' force coefficients, in particular damping, over a range of load and rotational speed conditions. This paper introduces a fluid film flow model accounting for both pivot and pad flexibility to predict the bearing journal eccentricity, drag power loss, lubricant temperature rise and force coefficients of typical TPJBs. A FE pad structural model including the Babbitt layer is coupled to the thin film flow model to determine the mechanical deformation of the pad surface. Predictions correlate favorably with test data, also demonstrating that pad flexibility produces a reduction of up to 50% in damping for the bearing with the thinnest pads relative to that with the thickest pads. A parametric study follows to quantify the influence of pad thickness on the rotordynamic force coefficients of a sample TPJB with three pads of increasing preload, $\overline{r}_p$ =0, 0.25 (baseline) and 0.5. The bearing pads are either rigid or flexible by varying their thickness. For design considerations, dimensionless static and dynamic characteristics of the bearings

are presented versus the Sommerfeld number (*S*). Pad flexibility shows a more pronounced effect on the journal eccentricity and the force coefficients of a TPJB with null pad preload than for the bearings with larger pad preloads (0.25 and 0.5), in particular for operation with a small load or at a high surface speed (S>0.8).

Turbulent flow may occur in (large size) hydrodynamic bearings operating at high rotational speeds and with low viscosity lubricants. Appendix A describes a turbulent bulk-flow model for thin films and presents predictions from the model for a large size four-pad water lubricated TPJB. The agreement with test data is remarkable as the bearing operating with turbulent flow has a much larger power loss and temperature rise.

Hydrodynamic bearings commonly use Babbitt layer as the liner to protect the surfaces of rotors while ensuring low friction. As a substitute for Babbitt, PTFE (polytetrafluoroethylene) shows better performance at high temperatures while offering a low breakaway friction. However, the high flexibility of PTFE does affect the static and dynamic forced performance of a hydrodynamic bearing. Appendix B describes a simple model for the liner elastic deformation due to hydrodynamic pressure and temperature differential. This deformation changes the operating clearance thus affecting the bearing performance. The model predictions are in good agreement with other model predictions in the literature. Liner flexibility reduces the peak film pressure and journal eccentricity.

Lastly, an addendum provides a (practical) graphical overview on the creation of the pad structural stiffness matrix using a commercial finite element software.

NOMENCLATURE

A	Cross-sectional area of a pad [m^2]
C_B	Bearing radial clearance [m]
C_p	Pad radial clearance [m]
C_{XX}, C_{YY}	Bearing damping force coefficients [N·s/m], $c=C\Omega C_p/W$
D	Bearing diameter [m]
E	Material elastic modulus [N/m^2]
E_{eq}	Equivalent elastic modulus of composite material [N/m^2]
e	Journal eccentricity [m]
f	Drag friction coefficient
h	Fluid film thickness [m]
h_X, h_Y, h_δ, h_ξ, h_η	Perturbed film thickness components due to pad motions
I	$Lt^3/12$. Pad area moment of inertia [m^4]
K_{XX}, K_{YY}	Bearing stiffness coefficients [N/m]
	$k=KC_p/W$
K_{piv}	Pivot stiffness [N/m] , $k_{piv}=K_{piv}C_p/W_{max}$
K_{pad}	Pad bending stiffness [N/m]
	$k_{pad}= K_{pad}C_p(LD)/W$
L	Bearing length [m]
M_b	Bending moment [N·m]
M_{XX}, M_{YY}	Bearing virtual mass force coefficients [kg] $m=M\Omega^2C_p/W$
N	Journal rotational speed [rev/s], $N=\Omega/2\pi$
P	Pressure field on pad surface [Pa]
P_X, P_Y, P_δ, P_ξ, P_η	Perturbed (first-order) pressure fields due to journal and pad motions [Pa/m]
$\overline{p}$	Uniform pressure applied on a pad [Pa]
R, R_B	Journal and bearing radii [m]
R_d	Distance from pivot to bearing center [m]
R_{eq}, R_n	Neutral axis of arc pad, single and two materials [m]

R_p	Pad radius [m]
R	$(R+t)/R$. Ratio of pad inner & outer radii
r_p	Pad dimensional preload [m], $r_P=C_P-C_B$ $\overline{r}_p=r_P/C_P$
S	Sommerfeld number, $S=\mu NDL(R/C_P)^2/W$
T	Fluid film temperature [°C]
T_{orque}	Bearing drag torque [N.m]
T	Pad thickness [m]
U	Pad surface nodal displacement [m]
u_t	Deformation at pad edges [m]
W	Static load applied on the bearing [N]
Z	$K + i\ \omega C$. Complex dynamic stiffness coefficients [N/m]
$\tilde{Z}_{\alpha\beta}$	Fluid film complex dynamic stiffness coefficients [N/m, Nm/rad] $\alpha,\beta=X, Y, \delta, \zeta, \eta$
δ_P	Pad tilt angle [rad]
$\Delta\sigma$	Perturbation in parameter σ
ΔW	External dynamic force [N]
η_{piv}	Pad transvers displacement [m]
Θ_p	Pad arc length [rad]
θ_P	Pivot angular position [rad]
μ	Oil viscosity [Pa.s]
ξ_{piv}	Pad radial displacement [m]
ρ	Oil density [kg/m^3]
Ω	Journal rotational speed [rad/s]
ω	Excitation frequency [rad/s]

Coordinate Systems

(X,Y)	Cartesian coordinates for journal center displacements
(ξ,η)	Pad pivot local coordinates
(r,θ,z)	Cylindrical coordinates for pad finite element structural model

Vectors and Matrices

$\mathbf{A}$	Matrix of element surfaces
$\bar{\mathbf{F}}$	Reduced external force vector
$\mathbf{K}$	Pad stiffness matrix
$\bar{\mathbf{K}}$	Reduced stiffness matrix
$\mathbf{L}$	Lower triangular form
$\mathbf{P}$	Pressure filed
$\mathbf{S}$	Surface traction vector
$\mathbf{U}$	Pad displacement vector
$\bar{\mathbf{u}}$	Reduced pad displacement vector

Superscripts

G	Global matrix
K	k^{th} pad

Subscripts

0	Static equilibrium position
α,β,σ	$X,Y,\delta,\ \xi,\eta$
P	Pad upper surface

Acronyms

DOF	Degree of freedom
FE	Finite element
LOP	Load on pad
LBP	Load between pad
TPJB	Tilting pad journal bearing

LIST OF CONTENTS

EXECUTIVE SUMMARY. 2
NOMENCLATURE...4
LIST OF FIGURES..8
LIST OF TABLES...11
INTRODUCTION...12
REYNOLDS EQUATION FOR THIN FILM BEARINGS...16
ANALYSIS FOR PAD MECHANICAL DEFORMATIONS..18
PERTURBATION ANALYSIS OF THE THIN FILM FLOW EQUATION.................21
COMPARISON OF PREDICTIONS AGAINST TEST DATA......................................24
PARAMETRIC STUDY ON THE EFFECT OF PAD FLEXIBILITY ON TPJB PERFORMANCE...41
CONCLUSION..53
REFERENCES...55
APPENDIX A HIRS TURBULENT FLOW MODEL...58
APPENDIX B A MODEL FOR BEARING LINER DEFORMATION.........................65

ADDENDUM. A Guide to get a pad structural stiffness matrix in ANSYS

LIST OF FIGURES

Figure 1 Schematic view of an idealized TPJB. Film thickness (h), pad deflection (u_p), pad rotation (δ_p) and pivot deflections (ξ_{piv},η_{piv}) greatly exaggerated. 17

Figure 2 (a) Typical FE model and mesh for a bearing pad, and (b) boundary conditions on pad as modeled in Ref. [14]. u_r, u_θ, u_z are the nodal displacements along the radial, angular, axial directions, respectively. 19

Figure 3 Load configuration for three pad TPJB and photograph of one pad...........25

Figure 4 Illustration of three pad bearing and set up for measurement of pivot stiffness...26

Figure 5 Journal eccentricity (e_Y) along the load direction versus unit load $W/(LD)$. Journal speed Ω=6 krpm and 12 krpm. Predictions (without and with pad flexibility) and test data from Gaines [1]. Results shown for thin, medium and thick pads. 27

Figure 6 Maximum pad-surface temperature versus unit load $W/(LD)$. Journal speed Ω=6 krpm and 12 krpm. Predictions (without and with pad flexibility) and test data from Gaines [1]. Inlet oil temperature, T_{in} = 49°C. Results shown for thin, medium and thick pads..28

Figure 7 Real part of complex stiffnesses for TPJBs with pads of thickness (a) t=8.5 mm (b) t=10 mm (c) t=11.5 mm. Shaft speed Ω=6 krpm and unit load $W/(LD)$=1,726 kPa. Test data from Gaines [1] and predictions (with and without pad flexibility)...30

Figure 8 Real part of complex stiffnesses for TPJBs with pads of thickness (a) t=8.5 mm (b) t=10 mm (c) t=11.5 mm. Shaft speed Ω=12 krpm and unit load $W/(LD)$=1,726 kPa. Test data from Gaines [1] and predictions (with and without pad flexibi..32

Figure 9 Imaginary part of complex stiffnesses for TPJBs with pads of thickness (a) t=8.5 mm (b) t=10 mm (c) t=11.5 mm. Shaft speed Ω=6 krpm and unit load $W/(LD)$=1,726 kPa. Test data from Gaines [1] and predictions (with and without pad flexibility)..34

Figure 10 Imaginary part of complex stiffnesses for TPJBs with pads of thickness (a) t=8.5 mm (b) t=10 mm (c) t=11.5 mm. Shaft speed Ω=12 krpm and unit load $W/(LD)$=1,726 kPa. Test data from Gaines [1] and predictions (with and without pad flexibility)..35

Figure 11 Direct stiffnesses (k_{XX} and k_{YY}) versus unit load and two shaft speeds. Predictions (without and with pad flexibility) and test data from Gaines [1]. Results shown for thin, medium and thick pads.)....................................37

Figure 12 Predicted film pressure and film thickness at bearing mid plane. Operation with unit load $W/(LD)$=172 kPa and shaft speed Ω=6 krpm. Location of the maximum film pressure for each pad: θ_1=33° (pad 1), θ_2=153° (pad 2) and θ_3=273° (pad 3). Location of the minimum film thickness for each pad:

θ_1=53° (pad 1), θ_2=173° (pad 2) and θ_3=301° (pad 3)...............................38

Figure 13 Direct damping coefficients (c_{XX} and c_{YY}) versus unit load and two shaft speeds. Predictions (without and with pad flexibility) and test data from Gaines [1]. Results shown for thin, medium and thick pads......................39

Figure 14 Direct virtual mass coefficients (m_{XX} and m_{YY}) versus unit load and shaft speed= 6krpm. Predictions (without and with pad flexibility) and test data from Gaines [1]. Results shown for thin, medium and thick pads.............40

Figure 15 Three-pad TPJB journal eccentricity (e/C_p) vs. Sommerfeld number (S). Pad stiffness k_{pad} = 3.15, 7.33, ∞ (rigid) and k_{piv} = 16. Pad preload varies: LBP and LOP configurations. Specific load $W/(LD)$=689 kPa, rotor speed Ω=500 rpm to 12,000 rpm...44

Figure 16 Three-pad TPJB drag friction coefficient (f) vs. Sommerfeld number. Pad stiffness k_{pad} = 3.15, 7.33, ∞ (rigid) and k_{piv} = 16. Pad preload varies: LBP and LOP configurations. Specific load $W/(LD)$=689 kPa, rotor speed Ω=500 rpm to 12,000 rpm...45

Figure 17 Three-pad TPJB stiffness coefficients (k_{XX}, k_{YY}) vs. Sommerfeld number (S). Pad stiffness k_{pad} = 3.15, 7.33, ∞ (rigid) and k_{piv} = 16. Pad preload $\bar{r}_p$ =0, 0.5: LBP configuration. Specific load $W/(LD)$=689 kPa, rotor speed Ω=500 rpm to 12,000 rpm...47

Figure 18 Three-pad TPJB stiffness coefficients (k_{XX}, k_{YY}) vs. Sommerfeld number (S). Pad stiffness k_{pad} = 3.15, 7.33, ∞ (rigid) and k_{piv} = 16. Pad preload $\bar{r}_p$ =0.25: LOP and LBP configurations. Specific load $W/(LD)$=689 kPa, rotor speed Ω=500 rpm to 12,000 rpm...48

Figure 19 Three-pad TPJB damping coefficients (c_{XX}, c_{YY}) vs. Sommerfeld number. Pad stiffness k_{pad} = 3.15, 7.33, ∞ (rigid) and k_{piv} = 16. Pad preload $\bar{r}_p$ =0, 0.5: LBP configuration. Specific load $W/(LD)$=689 kPa, rotor speed Ω=500 rpm to 12,000 rpm...49

Figure 20 Three-pad TPJB damping coefficients (c_{XX}, c_{YY}) vs. Sommerfeld number (S). Pad stiffness k_{pad} = 3.15, 7.33, ∞ (rigid) and k_{piv} = 16. Pad preload $\bar{r}_p$ =0.25: LOP and LBP configurations. Specific load $W/(LD)$=689 kPa, rotor speed Ω=500 rpm to 12,000 rpm..50

Figure 21 Three-pad TPJB virtual mass coefficients (m_{XX}, m_{YY}) vs. Sommerfeld number (S). Pad stiffness k_{pad} = 3.15, 7.33, ∞ (rigid) and k_{piv} = 16. Pad preload $\bar{r}_p$ =0, 0.5: LBP configuration. Specific load $W/(LD)$=689 kPa, rotor speed Ω=500 rpm to 12,000 rpm...51

Figure 22 Three-pad TPJB damping coefficients (m_{XX}, m_{YY}) vs. Sommerfeld number (S). Pad stiffness k_{pad} = 3.15, 7.33, ∞ (rigid) and k_{piv} = 16. Pad preload $\bar{r}_p$ =0.25: LOP and LBP configurations. Specific load $W/(LD)$=689 kPa, rotor speed Ω=500 rpm to 12,000 rpm. 52

Figure A.1 Schematic view of large four-pad TPJB in Ref [A.5] 61

Figure A.2 Film thickness at mid-plane of pads #1 and #2. Current predictions and results in Ref. [A.5]. $W/(LD)$=1,252 kPa,Ω=3 krpm, average Re=2,043.

....61

Figure A.3 Pressure profile at the mid-plane of pads #1 and #2. Current predictions and results in Ref. [A.5]. *W*/(*LD*)=1,252 kPa,**Ω**=3 krpm, average Re=2,043. 62

Figure A.4 Temperature at the mid-plane of pads #1 and #2. Current predictions and results in Ref. [A.5]. *W*/(*LD*)=1,252 kPa,**Ω**=3 krpm, average Re=2,043. 62

Figure A.5 Bearing friction loss at *W*/(*LD*)=1,252 kPa. Speed varing 1200 rpm to 4200 rpm. Current predictions and results in Ref. [A.5]. average Re from 1201 to 4774...63

Figure B.1 Schematic view of plain journal bearing with a liner, as per Ref. [B.1] 66

Figure B.2 Fluid film thickness at the bearing mid-plane. Static load *W*/(*LD*)=3,073 kPa, rotor speed **Ω**=900 rpm. Current predictions and data from Ref. [B.1]. 68

Figure B.3 Fluid film pressure at the bearing mid-plane. Static load *W*/(*LD*)=3,073 kPa, rotor speed **Ω**=900 rpm. Current predictions and data from Ref. [B.1]. 68

Figure B.4 (a) Maximum pressure, (b) minimum fluid film thickness and (c) eccentricity ratio and (d) maximum temperature at different load. 504 kPa<*W*/(*LD*)<6,297 kPa. **Ω**=900rpm. Current predictions and data from Ref. [B.1]...69

LIST OF TABLES

Table 1 Geometry, lubrication properties, and operating conditions of three test TPJBs [1]....................24
Table 2 Estimated average pivot stiffness for each pad set configuration in Ref. [1]. 26
Table 3 Cases to assess effect of pad flexibility on the performance of a TPJB......41
Table A.1 Geometry and lubricant properties of the test TPJB in Ref.[A.5]...............60
Table B.1 Parameters of a plain journal bearing in Ref. [B.1]....................................66
Table B.2 PTFE liner properties in Ref. [B.1]..67
Table B.3 Cases to assess effect of liner flexibility on the performance of a plain journal bearing..67

INTRODUCTION

Tilting pad journal bearings (TPJBs) offer rotor dynamically stable performance, a distinct advantage over fixed geometry fluid film bearings [2]. This feature is attractive for high speed rotating machinery applications where high levels of damping are desirable with absence of (destabilizing) cross-coupling hydrodynamic effects. During the last decade there have been various test programs aiming to quantify the rotordynamic force coefficients of TPJBs while also elucidating the importance of excitation frequency dependence. Amongst these concerted efforts, Refs. [3-7] report that the actual damping offered by TPJBs is lower than predicted; possibly degrading with increasing rotor speed and applied load. Discrepancies between predictions and experimentally identified force coefficients, in particular under a heavy static load, $W/(LD)$ >2.0 MPa, are attributed to the physical model(s) not accounting for either pad and/or pivot flexibility [6,7].

Refer to San Andrés et al. [8,9] for a review on the effects of pivot stiffness on the force coefficients of TPJBs, the description of a predictive model and its validation against test force coefficients available in the literature, and a discussion on the impact of pivot flexibility on the performance of TPJBs.

Analyses including pad surface flexibility on the modeling of the forced response of TPJBs are well documented. In a few analyses, pad flexibility is modeled with a moment-bending stiffness derived from beam theory and a change in pad curvature that reduces the pad mechanical preload as the applied load increases [6,7,9-12]. In other analyses, the whole pad structure is modeled with finite elements (FE), for example, and active degrees of freedom synthetized to produce a system of algebraic equations relating the hydrodynamic pressure to a pad surface deformation field that affects the film thickness [13-16]. In 1978, Nilsson [10] predicts single pad force coefficients for arc lengths varying from 60° to 120° and realizes that the pad with the longest arc length bends more and affects more the damping coefficients. At a specific journal eccentricity (e/C_B=0.5), the direct damping coefficient along the load direction decreases by 6% for a 60° arc pad and by 21% for a 120° arc pad. Ettles [11] in 1980 produces a computational one-dimensional beam model for pad deflections due to both a hydrodynamic film pressure and thermally induced stresses. Ettles contrasts the force coefficients of TPJBs with rigid pads against those with flexible pads, and finds an apparent reduction in damping (up to 40%) due to pad flexibility, further aggravated as the applied static load increases. Ettles notes that pad flexibility has a negligible effect on the journal eccentricity (and minimum film thickness), the maximum fluid film temperature; and for actual thick pads configurations, has no discernible effect on the bearing stiffnesses. In 1987, Lund and Pederson [12] detail a perturbation analysis to derive the bearing dynamic force coefficients including both pad and pivot flexibility. The authors find that the more flexible a pad is, the more is the reduction in the bearing damping coefficients.

To include for pad axial deformations, in 1989 Brugier and Pascal [13] build a three-dimensional (3D) finite element (FE) structural pad model to predict the elastic deformation of the pads. Predictions for a large scale three-pad TPJB with a diameter of 0.75 m and a slender ratio (*L*/*D*) of 0.75 show that both pad flexibility and pivot flexibility reduce significantly the bearing force coefficients, yet only produce a small decrease in the maximum film temperature and the minimum film thickness of the most loaded pad. The authors also predict an increase in direct stiffness coefficients at low loads due to both pad and pivot flexibility. Later in 1995, Desbordes *et al*. [14] evaluate predictions using two-dimensional (2D) and three-dimensional (3D) FE structural pad models and realize that pad deflections along the axial direction are not negligible in a heavily loaded TPJB.

Neglecting the variation of the pad mechanical deformation along the axial direction, in 1990 Earles *et al*. [15] use a two-dimensional (2D), plane strain FE model to evaluate pad flexibility effects on the forced performance of TPJBs. By assuming a pad keeps its original curvature, the complex multiple degree of freedom (DOF) system is reduced to one single parameter which reflects as change in pad radius. Frequency reduced dynamic force coefficients for a single pad correlate well, within 5% difference, with those obtained by Lund and Pedersen [12]. Earles *et al*. [16] also implement a “Pad Assembly Method” to obtain the dynamic force coefficients of a TPJB. With pivot flexibility modeled using Hertzian contact theory, the TPJB stiffness and damping matrices contain each $(3N_{pad}+2)^2$ coefficients. Using synchronous speed reduced TPJB force coefficients in a particular rotor-bearing system, the authors report that pad flexibility produces a reduction of 6% in the predicted onset speed of instability.

Childs and students [1,3,5-7,17] utilize a test rig for measurement of the static and dynamic load performance of hydrodynamic bearings. This test rig comprises of a rigid rotor supported on rolling element bearings and with a softly supported (floating) bearing cartridge holding the test bearing element at the rotor mid span. Operators perform sets of tests spanning a range of applied static loads for one or more shaft speed conditions. Importantly enough, most tests are conducted with a constant lubricant supply rate, irrespective of the shaft speed or load condition. Orthogonally placed external shakers deliver multiple frequency dynamic loads exciting the test element over a prescribed frequency range. Bearing force coefficients – stiffness, mass and damping (K, C, M), are extracted from curve fits to experimentally derived complex stiffness functions. Recently, Wilkes [7] reports both measurements and predictions for a load on pad (LOP), five-pad TPJB with 50% pad pivot offset. Wilkes' predictions point to pad flexibility having a more pronounced effect under large loads. Do notice that Wilkes' meticulous work produces a method to measure pad flexibility by inducing moments on the leading and trailing edges of a pad and recording the pad strain. Wilkes plots the pad bending stiffness versus the applied bending moment curves and obtains the bending stiffness for the pad in his test bearing. Wilkes uses this bending stiffness to predict pad flexibility and regards the pad deformation as a change in pad clearance.

Based on the urge of Wilkes [7] to assess systematically the effect of pad flexibility on the dynamic force coefficients of TPJBs, Gaines [1] conducts a concerted effort to quantify the influence of pad thickness, e.g. its flexibility, on the static and dynamic forced performance of a three pad TPJB installed in a load between pads (LBP) configuration. Gaines used three sets of pads, each with an arc length of 90^o, and varying in thickness t=8.5 mm, 10 mm and 11.5 mm. The unit load $W/(LD)$ applied to the bearings increases from 1,72 kPa to 1,724 kPa while operating at three rotor speeds: 6, 9 and 12 krpm (32, 48, and 64 m/s). Test data show that the direct damping coefficients decrease up to 20% as pad flexibility increases. The reduction in direct damping coefficients due to pad flexibility prevails as the rotor speed increases but keeps nearly constant as the unit load varies. However, the effect of pad flexibility on the bearing direct stiffnesses is minor. Similar to Brugier and Pascal's findings [13], Gaines also notices up to a 12% increase in direct stiffnesses as pad flexibility increases for operation with a low unit load, $W/(LD)<689$ kPa. Even at the largest unit load of $W/(LD)=1{,}726$ kPa, the direct stiffnesses of the TPJB with thin pad sets ($t=8.5$ mm) is only 3% smaller than those of the TPJB with thick pad sets ($t=11.5$ mm). Refer to Gaines [1] for a lucid review of the archival literature on experiments related to pad flexibility and its effects on TPJB force coefficients. See also Ref. [17] for an abridged version of the original reference and a discussion on the effects of pad flexibility within the context of practical TPJB configurations.

The current analysis extends the physical model in Refs. [8,9] to include pad flexibility to predict a TPJB static performance (e.g., journal eccentricity and minimum film thickness, fluid film temperature, etc.) and its dynamic force coefficients. A FE pad structural model including the Babbitt layer is coupled to the thin film flow model to determine the mechanical deformation of the pad surface. Exhaustive predictions are compared to the test data reported by Gaines [1]. The discussion produces relevant correlations while still stressing differences. Lastly, a parametric study follows to investigate the effects of pad and pivot stiffnesses, pad preload, and load orientation on TPJB force performance, static and dynamic. The graphs constructed using dimensionless parameters provide a bearing designer with a guide to estimate the effect of pad flexibility on journal eccentricity, drag friction coefficient, and the stiffness, damping and virtual mass force coefficients.

REYNOLDS EQUATION FOR THIN FILM BEARINGS

Figure 1 depicts a schematic view of an idealized TPJB with its major components and reference coordinate systems. The external static load (W) forces the journal spinning with rotational speed (Ω) to displace to eccentricity (e_X, e_Y) away from the bearing center. The pads in the bearing generate a fluid film hydrodynamic pressure (P) that acts on the journal to oppose the applied load. The pressure also acts on each pad, tilting the pad about its pivot with rotation δ_p and displaces the pad pivot to ξ_{piv} and η_{piv}. The pressure field also deforms elastically the pads. Of importance is u_p the deformation field on the pad surface facing the fluid film.

An extended Reynolds equation[1] [8,9] with temporal fluid inertia effects governs the generation of hydrodynamic pressure (P^k) in the k^{th} pad with film thickness h^k,

$$\vec{\nabla}\bullet\left\{\frac{\left(h^k\right)^3}{12\mu}\vec{\nabla}P^k\right\}=\frac{\partial h^k}{\partial t}+\frac{\Omega}{2}\frac{\partial h^k}{\partial\theta}+\frac{\rho\left(h^k\right)^2}{12\mu}\frac{\partial^2 h^k}{\partial t^2} \tag{1}$$

where (z, θ) are the axial and circumferential coordinates on the plane of the bearing. The film thickness h^k is

$$\begin{aligned} h^k &= u_p^k + C_P + e_X\cos\theta + e_Y\sin\theta \\ &\quad + \left(\xi_{piv}^k - r_P\right)\cos\left(\theta-\theta_p^k\right) + \left(\eta_{piv}^k - R_d\delta_p^k\right)\sin\left(\theta-\theta_p^k\right) \end{aligned} \tag{2}$$

where C_P and C_B are the pad machined radial clearance and bearing assembly clearance, respectively, and $r_P=(C_P-C_B)$ is the pad mechanical preload. Above $R_d=R_P+t$ is the sum of the pad machined radius and pad thickness at the pivot location. The pad surface deflection field $\left(u_p^k>0\right)$ increases the film thickness.

---

[1] The model includes for flow turbulence and thermal energy transport effects. The analysis (equations) for these flow conditions are not included for brevity.

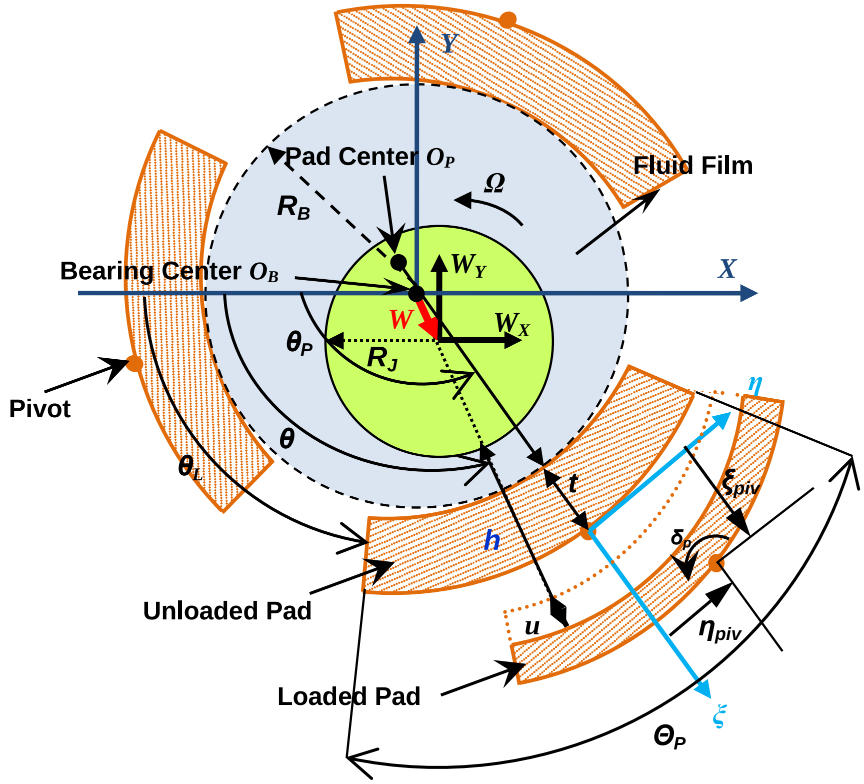
Y
Pad Center O_P
Ω
Fluid Film
R_B
Bearing Center O_B
X
W_Y
W
W_X
θ_P
R_J
Pivot
θ
θ_L
t
η
ξ_{piv}
h
δ_p
Unloaded Pad
u
η_{piv}
Loaded Pad
ξ
Θ_P

Figure 1 Schematic view of an idealized TPJB. Film thickness (h), pad deflection (u_p), pad rotation (δ_p) and pivot deflections (ξ_{piv},η_{piv}) greatly exaggerated.

ANALYSIS FOR PAD MECHANICAL DEFORMATIONS

A structural FE analysis predicts the displacements of the k^{th} pad upper surface caused by the fluid film pressure field (P). Figure 2(a) depicts a typical pad assembling a number of brick-like finite elements. The equation for the deflection field ($\mathbf{u^G}$) due to an applied load ($\mathbf{F^G}$) is [14]:

$$\mathbf{K}^{\mathbf{G}}\mathbf{u}^{\mathbf{G}} = \mathbf{F}^{\mathbf{G}} + \mathbf{S}^{\mathbf{G}} \tag{3}$$

where $\mathbf{K^G}$ is a global stiffness matrix and $\mathbf{S^G}$ is a vector of surface tractions. Desbordes *et al*. [14] introduce appropriate boundary conditions for an ideal tilting pad, i.e., one with infinite pivot stiffness. Figure 2(b) depicts in graphical form the lines where boundary conditions are specified. The solid line denotes the pivot (line contact) and all FE nodes are constrained to a null displacement; $u_r=u_\theta=u_z=0$, along the radial, circumferential, and axial directions. The two dashed lines parallel to the line contact denote nodes with no radial displacement, $u_r=0$ only. On these lines, the nodes can take circumferential (transverse) and axial displacements.

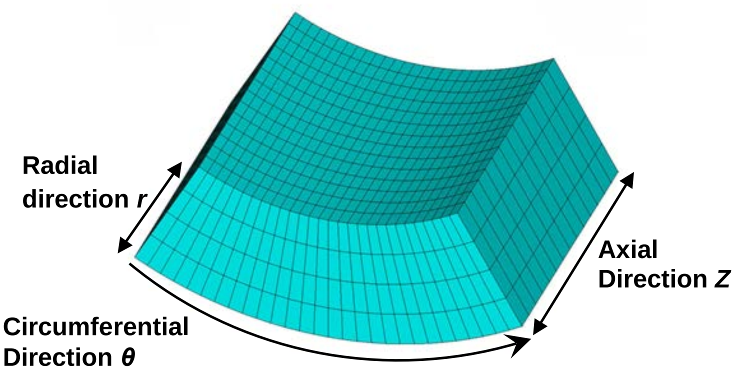

(a) Pad assembled by finite elements

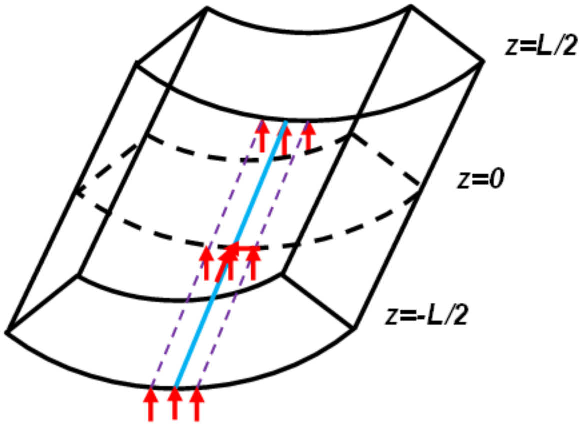

(b) Boundary conditions at pivot line

Figure 2(a) Typical FE model and mesh for a bearing pad, and (b) boundary conditions on pad as modeled in Ref. [14]. u_r**,** u_θ**,** u_z **are the nodal displacements along the radial, angular, axial directions, respectively.**

Once the pivot boundary conditions are assigned, the global system of equations reduces to

$$\bar{\mathbf{K}}^{\mathrm{G}}\bar{\mathbf{u}}^{\mathrm{G}} = \bar{\mathbf{F}}^{\mathrm{G}} \tag{4}$$

where $\bar{\mathbf{K}}^{\mathrm{G}}$ is a reduced (non-singular) stiffness matrix, and $\bar{\mathbf{u}}^{\mathrm{G}}$ and $\bar{\mathbf{F}}^{\mathrm{G}}$ are the vectors of global displacements and forces. The external load generated by the film pressure acts on the (upper) surface of the pad. Thus, further manipulation to reduce Eq. (4) is warranted. Write the vectors of displacements and generalized force in terms of active and inactive degrees of freedom, i.e.,

$$\bar{\mathbf{u}}^{\mathrm{G}} = \begin{bmatrix}\mathbf{u}_{\mathbf{p}} & \bar{\mathbf{u}}\end{bmatrix}^{\mathrm{T}}; \qquad \bar{\mathbf{F}}^{\mathrm{G}} = \begin{bmatrix}\mathbf{f}(P) & \mathbf{0}\end{bmatrix}^{\mathrm{T}} \tag{5}$$

where $\mathbf{u_p}$ denotes the vector of radial displacements on the pad upper surface which are active DOFs, and $\bar{\mathbf{u}}$ is the vector of displacements of other nodes, $\mathbf{f}(P)$=($\mathbf{AP}$) is the vector of nodal forces generated by the pressure field $\mathbf{P}$ with $\mathbf{A}$ as a square matrix containing element surfaces. The reduced global stiffness matrix $\bar{\mathbf{K}}^{\mathrm{G}}$ can be partitioned as

$$\bar{\mathbf{K}}^{G} = \left[\begin{array}{c:c} \bar{\mathbf{K}}_{\mathbf{p}} & \bar{\mathbf{K}}_{\mathbf{s}} \\ \hdashline \bar{\mathbf{K}}_{\mathbf{s}} & \bar{\mathbf{K}}_{\mathbf{na}} \end{array}\right] \tag{6}$$

with these definitions, Eq. (4) can be written as

$$\begin{aligned} \bar{\mathbf{K}}_{\mathbf{p}}\ \mathbf{u}_{\mathbf{p}} + \bar{\mathbf{K}}_{\mathbf{s}}\,\bar{\mathbf{u}} &= \mathbf{f}(P) \\ \bar{\mathbf{K}}_{\mathbf{s}}\mathbf{u}_{\mathbf{p}} + \bar{\mathbf{K}}_{\mathbf{na}}\bar{\mathbf{u}} &= \mathbf{0} \end{aligned} \tag{7}$$

From Eq. (7a), $\bar{\mathbf{u}} = -\left[\bar{\mathbf{K}}_{\mathbf{na}}\right]^{-1}\bar{\mathbf{K}}_{\mathbf{s}}\mathbf{u}_{\mathbf{p}}$ and the displacements on the pad surface are obtained from

$$\mathbf{K}_{\mathbf{p}}\,\mathbf{u}_{\mathbf{p}} = \mathbf{f}(P) \tag{8}$$

where $\mathbf{K}_{\mathbf{p}} = \left(\bar{\mathbf{K}}_{\mathbf{p}} - \bar{\mathbf{K}}_{\mathbf{s}}\left[\bar{\mathbf{K}}_{\mathbf{na}}\right]^{-1}\bar{\mathbf{K}}_{\mathbf{s}}\right)$ is a positive definite symmetric matrix, easily decomposed into its lower and upper triangular forms, $\mathbf{K}_{\mathbf{p}} = \mathbf{L}\mathbf{L}^{\mathbf{T}}$. Hence, Eq. (8) is rewritten as

$$\mathbf{L}\left(\mathbf{L}^{\mathbf{T}}\mathbf{u}_{\mathbf{p}}\right) = \mathbf{f}(P) \tag{9}$$

Let $\mathbf{u}_{\mathbf{p}}^{*} = \mathbf{L}^{\mathbf{T}}\mathbf{u}_{\mathbf{p}}$; a backward substitution procedure solves first $\mathbf{L}\mathbf{u}_{\mathbf{p}}^{*} = \mathbf{f}(P)$ to give $\mathbf{u}_{\mathbf{p}}^{*}$; and next, a forward substitution procedure solves $\mathbf{L}^{\mathbf{T}}\mathbf{u}_{\mathbf{p}} = \mathbf{u}_{\mathbf{p}}^{*}$ to determine $\mathbf{u}_{\mathbf{p}}$, i.e., the vector of radial displacement at the pad surface. The vector $\mathbf{u}_{\mathbf{p}}$ is used to update the film thickness (*h*), Eq. (2), for solution of the Reynolds Eq. (1) to find the pressure field (*P*). Note that the FE structural pad model and its end result, the **L** matrix, needs to be performed only once, preferably outside of the main computational program.

PERTURBATION ANALYSIS OF THE THIN FILM FLOW EQUATION

At a constant shaft speed (Ω), the static load $\mathbf{W_0}=\left(W_{X_0},W_{Y_0}\right)^{\mathrm{T}}$ displaces the journal to it equilibrium position $\mathbf{e_0}=\left(e_{X_0},e_{Y_0}\right)^{\mathrm{T}}$ with the generated fluid film pressure (P_0^k) acting on each pad surface. The k^{th} pad reaches its equilibrium position $\left(\delta_{p_0}^k,\xi_{piv_0}^k,\eta_{piv_0}^k\right)^{\mathrm{T}}$ and the deflection of the pad upper surface is $u_{p_0}^k$.

An external dynamic force, $\mathbf{\Delta W}=(\Delta W_X,\ \Delta W_Y)^{\mathrm{T}}\, e^{i\omega t}$ with excitation frequency (ω) acts on the journal and causes the journal center to displace to $\mathbf{\Delta e}=(\Delta e_X,\ \Delta e_Y)^{\mathrm{T}}\, e^{i\omega t}$ away from $\mathbf{e_0}$, i.e., $\mathbf{e}_{(t)}=\mathbf{e_0}+\ \mathbf{\Delta e}\ e^{i\omega t}$ [18]. The journal motion leads to changes in the pad pivot displacements and the pad surface deformation as

$$\left(\delta_p^k,\xi_{piv}^k,\eta_{piv}^k\right)^{\mathrm{T}}=\left(\delta_{p_0}^k,\xi_{piv_0}^k,\eta_{piv_0}^k\right)^{\mathrm{T}}+\left(\Delta\delta_p^k,\Delta\xi_{piv}^k,\Delta\eta_{piv}^k\right)^{\mathrm{T}}e^{i\omega t} \tag{10a}$$

$$u_P^k=u_{P_0}^k+\Delta u_P^k e^{i\omega t},\ k=1,\ldots,N_{pad} \tag{10b}$$

On the k^{th} pad, the changes in journal center position and pad displacements cause a change in the film thickness as

$$h^k=h_0^k+\Delta h^k e^{i\omega t},\ k=1,\ldots,N_{pad} \tag{11a}$$

where

$$\Delta h^k=\{h_X^k\Delta e_X+h_Y^k\Delta e_Y+h_\xi^k\Delta\xi_{piv}^k+h_\eta^k\Delta\eta_{piv}^k+h_\delta^k\Delta\delta_p^k+\Delta u_p^k\} \tag{11b}$$

with $h_X^k=\cos\theta$, $h_Y^k=\sin\theta$, $h_\xi^k=\cos(\theta-\theta_p^k)$, $h_\eta^k=\sin(\theta-\theta_p^k)$, $h_\delta^k=-R_d h_\eta^k$ [18]. The fluid film pressure on a pad is

$$P^k=P_0^k+\Delta P^k e^{i\omega t},\ k=1,\ldots,N_{pad} \tag{12a}$$

where the change in fluid film pressure caused by the perturbations in displacements is

$$\Delta P^k=\{P_X^k\Delta e_X+P_Y^k\Delta e_Y+P_\xi^k\Delta\xi_{piv}^k+P_\eta^k\Delta\eta_{piv}^k+P_\delta^k\Delta\delta_p^k\} \tag{12b}$$

Let $\mathbf{g}(P^k)=\left[\mathbf{K}_\mathbf{p}^k\right]^{\mathbf{-1}}\mathbf{f}(\mathbf{P}^k)$. Hence, the pad deformations caused by the equilibrium pressure field $\left(\mathbf{P}_\mathbf{0}^k\right)$ and the perturbed pressure field ($\Delta\mathbf{P}^k$) are

$$\mathbf{u}_{\mathbf{P_0}}^k,\ \mathbf{\Delta u}_\mathbf{P}^k=\mathbf{g}(P_0^k),\ \mathbf{g}(\Delta P^k)\rightarrow\left[\mathbf{K}_\mathbf{p}^k\right]^{\mathbf{-1}}\mathbf{A}\,\mathbf{P}_\mathbf{0}^k,\ \left[\mathbf{K}_\mathbf{p}^k\right]^{\mathbf{-1}}\mathbf{A}\,\mathbf{\Delta P}^k \tag{13}$$

Substituting Eq. (12b) into Eq. (13) yields the change in pad surface deformation as

$$\Delta u_P^k = u_X^k \Delta e_X + u_Y^k \Delta e_Y + u_\delta^k \Delta \delta_p^k + u_\xi^k \Delta \xi_{piv}^k + u_\eta^k \Delta \eta_{piv}^k \tag{14}$$

Thus,

$$\begin{aligned}\Delta h^k &= (h_X^k + u_X^k)\Delta e_X + (h_Y^k + u_Y^k)\Delta e_Y + (h_\xi^k + u_\xi^k)\Delta \xi_{piv}^k \\ &\quad + (h_\eta^k + u_\eta^k)\Delta \eta_{piv}^k + (h_\delta^k + u_\delta^k)\Delta \delta_p^k\end{aligned} \tag{15}$$

That is, the film thickness changes due to physical displacements of the journal and pad as well as due to the deformation induced by a change or perturbation in pressure.

Define the following linear operators [19],

$$\ell(*) = \frac{\partial}{R\partial\theta}\left[\frac{h_0^3}{12\mu}\frac{\partial(*)}{R\partial\theta}\right] + \frac{\partial}{\partial z}\left[\frac{h_0^3}{12\mu}\frac{\partial(*)}{\partial z}\right] = \vec{\nabla}\left(\frac{h^3}{12\mu_{(T)}}\vec{\nabla}(*)\right) \tag{16}$$

$$\Re(*) = \left[\frac{\Omega}{2}\frac{\partial(*)}{\partial\theta} + i\omega(*) - \frac{\rho h_0^2}{12\mu_{(T)}}\omega^2(*)\right] - \vec{\nabla}\left(\frac{3h_0^2}{12\mu_{(T)}}(*)\vec{\nabla}P_0\right) \tag{17}$$

Substitution of h^k and P^k into the extended Reynolds Eq. (1) gives:

$$\ell(P_0) = \frac{\Omega}{2}\frac{\partial h_0}{\partial\theta} \tag{18}$$

and

$$\ell\left\{P_\sigma^k\right\} = \Re\left\{h_\sigma^k + u_\sigma^k\right\} \quad \alpha,\beta = X, Y, \delta, \xi, \eta \tag{19}$$

Note that the first-order or perturbed pressure fields due to a pad rotation and pivot radial and transverse displacements are a linear combination of P_X and P_Y [18,19], i.e.,

$$\begin{aligned} P_\delta^k &= -R_J P_\eta^k \\ P_\xi^k &= P_X^k \cos\theta_P^k + P_Y^k \sin\theta_P^k \quad, k = 1,\ldots,N_{pad} \\ P_\eta^k &= -P_X^k \sin\theta_P^k + P_Y^k \cos\theta_P^k \end{aligned} \tag{20}$$

Since the pad deformations are a linear function of the applied pressure, i.e., $u_\sigma^k = g(P_\sigma^k)$ with $\alpha,\beta = X, Y, \sigma, \xi, \eta$, then

$$\begin{aligned} u_\delta^k &= -R_J u_\eta^k \\ u_\xi^k &= u_X^k \cos\theta_P^k + u_Y^k \sin\theta_P^k \quad, k = 1,\ldots,N_{pad} \\ u_\eta^k &= -u_X^k \sin\theta_P^k + u_Y^k \cos\theta_P^k \end{aligned} \tag{21}$$

The analysis above reveals that the perturbed pressure fields due to pad rotation or pivot transverse displacements can be readily gathered from the fields determined for changes in the journal eccentricity (Δe_X, Δe_Y). Furthermore, the changes in pad deformation also follow immediately after the perturbed displacements $\left(u_X^k, u_Y^k\right)$ are found. The process is computationally fast and efficient. The only caveat is that Eq. (19) is solved iteratively, as $u_\sigma^k = g(P_\sigma^k)$ $_{\alpha,\beta=X,Y}$.

Integration of the pressure fields, obtained after solving the first order Eqs. (19) on the k^{th} pad, renders 25 fluid film dynamic complex stiffness coefficients ($\tilde{Z}_{\alpha\beta}^k$) [18]

$$\tilde{Z}_{\alpha\beta}^k = \int_{-L/2}^{L/2} \int_{\theta_l^k}^{\theta_t^k} P_\beta^k h_\alpha^k R_J \, d\theta^k dz \quad {}_{\alpha,\beta=X,Y,\sigma,\xi,\eta} \tag{22}$$

Reduced frequency force coefficients for lateral displacements, $Z_{\alpha\beta}=(K_{\alpha\beta}+i\omega C_{\alpha\beta})$ $_{\alpha,\beta=X,Y}$, are extracted from the complete sets of 25 Z's by assuming all pads move with the same frequency ω. For details on the reduction process, see Refs. [18-20].

COMPARISON OF PREDICTIONS AGAINST TEST DATA

Gaines [1] produced test data for three TPJB sets, each having three pads of unequal thickness, to quantify the effect of pad flexibility on the bearings force coefficients, in particular damping, over a range of loads and rotational speed conditions. This section presents exhaustive comparisons of predictions from the current model to the test data in Ref. [1]. Gaines and Childs [17] summarize the comprehensive measurements and data analysis in Ref. [1].

Table 1 lists the geometry of the TPJBs, lubricant properties and operation conditions and Figure 3 depicts the load between pads configuration of a test bearing and a photograph of one pad with a rocker back pivot type. The bearing assembly operates with a flooded lubricant supply condition, all measurements conducted with a flow rate of 31 LPM [1]. The arc length (90^{o}) and inner radius of the pads for the three bearing configurations are identical. A pad is composed of two materials: a main body made of steel and a Babbitt layer, 1.5 mm thick. The elastic moduli for steel and Babbitt are 200 GPa and 50 GPa, respectively [21]. The pad thicknesses (t) quoted includes the Babbitt thickness and is measured at the location noted in the photograph. Presently, in the discussion of results, the pads are referred as thin (t=8.5 mm), medium thickness (t=10 mm), and thick (t=11.5 mm).

Table 1 Geometry, lubrication properties, and operating conditions of three test TPJBs [1].

Number of pads, N_{pad}	3		
Configuration	LBP		
Rotor diameter, D	101.6 mm		
Pad axial length, L	61 mm		
Pad arc angle, Θ_P	90°		
Pivot offset	50%		
Nominal preload, $\overline{r}_p$	0.25		
Pad thickness, t	**8.5mm**	**10 mm**	**11.5mm**

Cold bearing clearance, C_B	69 µm	70 µm	70 µm
Cold pad clearance, C_P	92 µm	93 µm	93 µm
Lubricant type	ISO VG 46		
Supply lubricant temperature	49 °C		
Supply lubricant pressure	2.2 bar		
Lubricant density	854 kg/m^3		
Viscosity at 49 °C,μ_0	0.0269 Pa·s		
Viscosity temperature coefficient, α	0.0319 1/°C		
Specific heat capacity at 70 °C	1830 J/(kg·K)		
Specific load, $W/(LD)$	172 kPa -1724 kPa		
Journal speed,Ω	6,000-12,000 rpm		
Surface speed, ΩR	32-64 m/s		

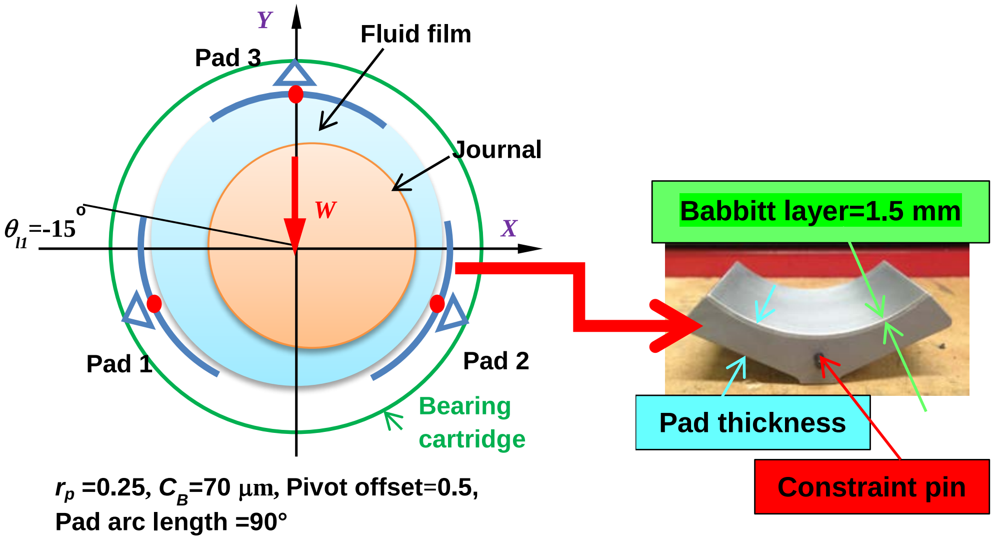
Y
Pad 3
Fluid film
Journal
W
X
θ_{l1}=-15°
Pad 1
Pad 2
Bearing cartridge
r_p =0.25, C_B=70 μm, Pivot offset=0.5,
Pad arc length =90°
Babbitt layer=1.5 mm
Pad thickness
Constraint pin

Figure 3 Load configuration for three pad TPJB and photograph of one pad.

To measure the pivot stiffness of a single pad, Gaines [1] assembled the bearing in a load on pad (LOP) orientation, as shown in Fig. 4. A hydraulic cylinder and spring pull on the bearing cartridge and displace it against the rigid rotor (journal). The applied load on the shaft is trough contact pressure over the whole pad arc extent. Eddy current sensors record the relative displacements between the bearing casing assembly and the journal or shaft.

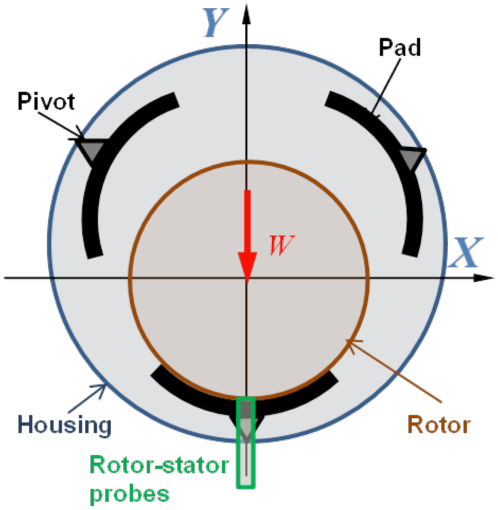

Figure 4 Illustration of three pad bearing and set up for measurement of pivot stiffness.

The load versus pivot deflection measurements conducted on pads (of differing thickness) evidence a nonlinear stiffening effect with mechanical hysteresis. For applied loads 47 kPa < $W/(LD)$ <1,100 kPa, Table 2 lists the average pivot stiffness[2] (K_{piv}) used in the following predictions.

Table 2 Estimated average pivot stiffness for each pad set configuration in Ref. [1]

	Pivot stiffness [MN/m]
Thin pad (t=8.5 mm)	573
Medium thickness pad (t=10 mm)	675
Thick (t=11.5 mm)	775

The current predictive model includes the shaft and pad thermal expansion due to rises in film temperature[3] that determine the *hot* bearing clearance. The predictive model assumes that the lubricant carries away all the heat generated in the bearing, i.e., an adiabatic heat flow process. The inlet heat carry over coefficient (λ) varies for differing rotor speeds[4]; at Ω=6 krpm, λ=0.8; while at Ω=12 krpm, λ=0.98. Predictions with and without pad flexibility are presented.

---

[2] It is not clear why the pads have differing stiffness as they have identical back surface configurations and contact areas at their pivot location.

[3] The shaft and pads, both made of steel, have a thermal expansion coefficient of 1.2×10^{-5}/ °C [22].

Figure 5 shows the predicted and measured journal eccentricity (e/C_P) along the load direction (Y) for operation at 6 krpm and 12 krpm. The predictions include curves for pad flexibility and without it. At both operational speeds (Ω=6 krpm, 12 krpm), the predictions with pad flexibility correlate best with the test data as the applied load increases. Predictions solely considering pivot flexibility deliver a larger static eccentricity. Pad flexibility tends to reduce the predicted journal eccentricity, in particular for operation at the high rotor speed (Ω=12 krpm).

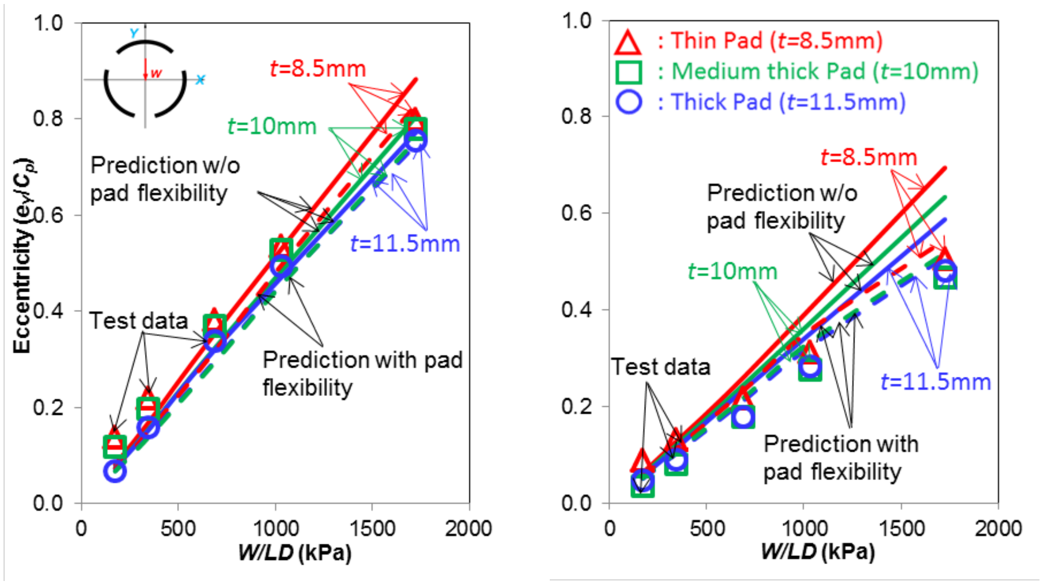

(a) speed 6 krpm

(b) speed 12 krpm

Figure 5 Journal eccentricity (e_Y) along the load direction versus unit load $W/(LD)$. Journal speed Ω=6 krpm and 12 krpm. Predictions (without and with pad flexibility) and test data from Gaines [1]. Results shown for thin, medium and thick pads.

Figure 6 depicts the predicted maximum film temperature rise ($\Delta T_{max}/T_{in}$) versus unit load for two journal speeds. In the tests [1], a pad (~5 mm below) sub-surface temperature is recorded at 75% of the pad arc length. Predictions account for the heat transfer conducted through a pad and the heat convection in the back of a pad. The predictions show the bulk fluid film temperature in pad 2. Generally, the maximum temperatures are underestimated, in particular at the high speed and largest load; Ω=12 krpm, *W/*(*LD*)=1,726 kPa.

---

[4] According to Tao [20], the inlet heat carry over coefficient (λ) varies with journal speed; a larger λ should be used for a high rotor speed (Ω>10 krpm).

The significant differences in temperatures are due to the test bearing being supplied with a fixed flow rate, irrespective of the load and journal speed condition. For test with a shaft speed of 6 krpm, the actual supplied flow rate (31 LPM) is greater than the one predicted (17 LPM) while the recorded peak pad surface temperatures are much higher. Note the oil is pushed through three holes and not routed efficiently into the bearing pads. To support the assertion, note that the recorded lubricant outlet temperature is much lower that the peak temperatures measured [1], and also lower than the predicted lubricant temperature at the bearing exit plane. Hence, excessive churning of the lubricant on the bearing sides contributes to the distinctive differences. Most of the cold supply flow rate does not enter the bearing pads, thus causing the bearing pads to heat excessively.

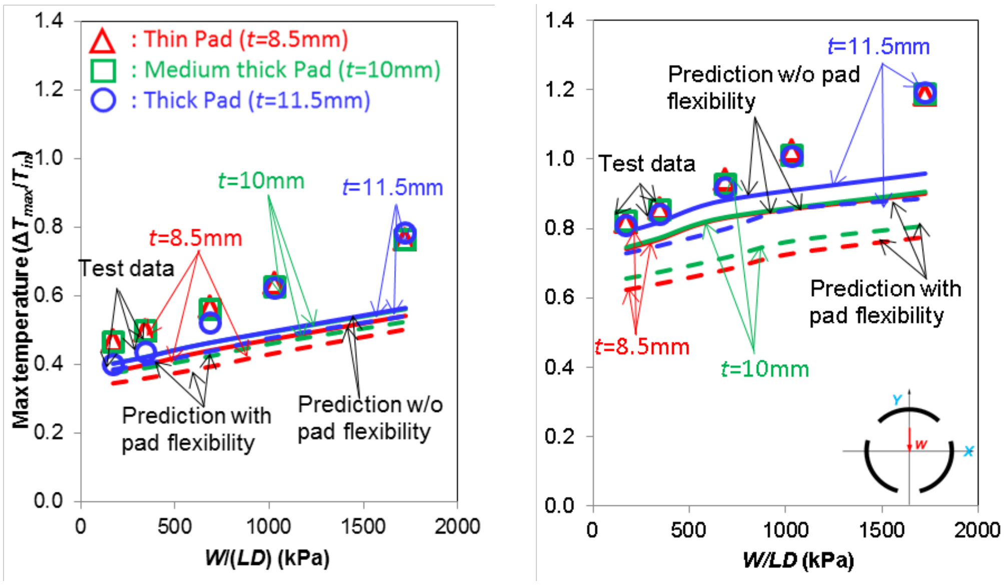

(a) speed 6 krpm (b) speed 12 krpm

Figure 6 Maximum pad-surface temperature versus unit load *W*/(*LD*). Journal speed Ω=6 krpm and 12 krpm. Predictions (without and with pad flexibility) and

test data from Gaines [1]. Inlet oil temperature, T_{in} = 49°C. Results shown for thin, medium and thick pads.

For the largest applied static load, Figs. 7 and 8 show the real part of the bearing direct complex stiffnesses, Re(Z), obtained at two shaft speeds (Ω=6 krpm and 12 krpm) versus excitation frequency ($0<\omega<200$ Hz). Note Re(Z_{YY}), along the load direction, is lesser than Re(Z_{XX}). This peculiar behavior is distinctive for the three pad bearing, each pad having a large (90°) arc extent. In general, the predicted Re(Z_{YY}) correlates best with the test data, whereas Re(Z_{XX}) is overestimated at high frequencies (ω>100 Hz). Note the experimental Re(Z) show little frequency dependency, yet the predictions forward a stiffening Re(Z_{YY}) as frequency increases, and in particular for operation at the low shaft speed (6 krpm). Including pad flexibility reduces the dynamic stiffness, Re(Z); the effect being more pronounced on the thin pad.

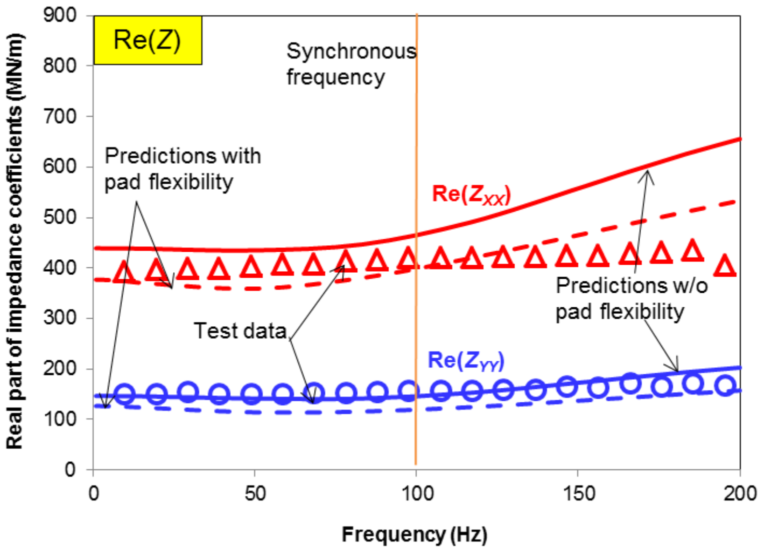

(a) Thin pad, t=8.5 mm

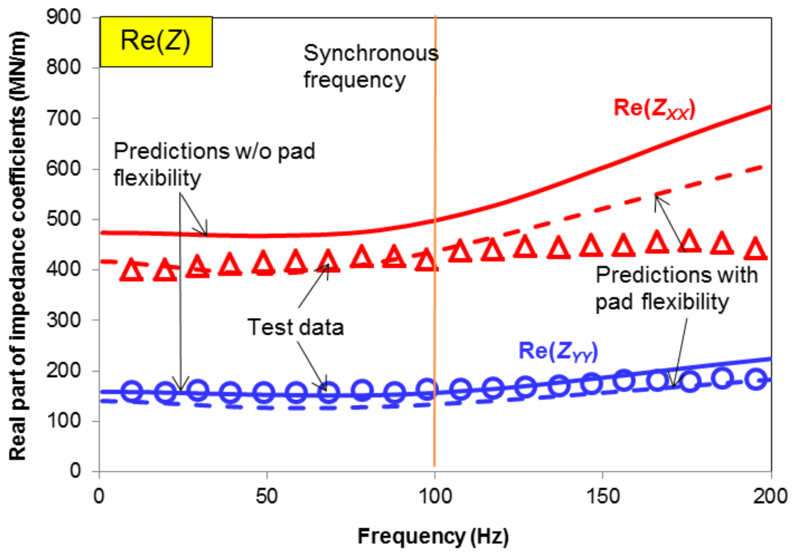

(b) Medium thickness pad, t=10 mm

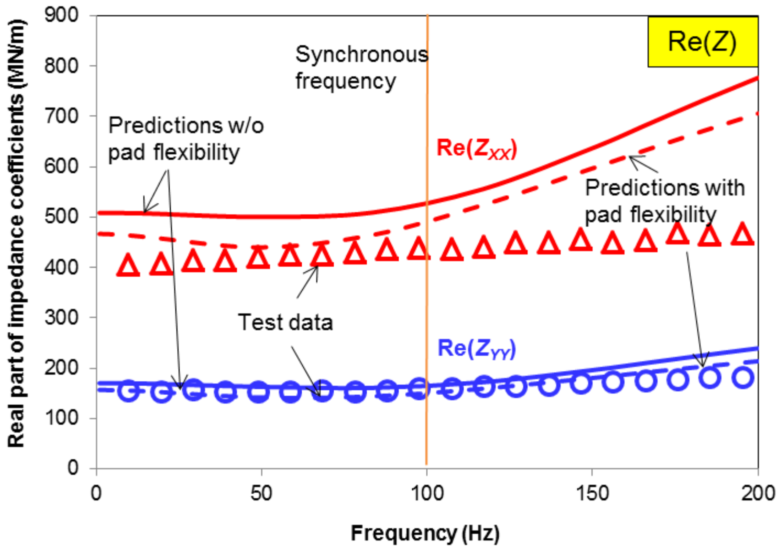

(c) Thick pad, t=11.5 mm

Figure 7 Real part of complex stiffnesses for TPJBs with pads of thickness (a) *t*=8.5 mm (b) *t*=10 mm (c) *t*=11.5 mm. Shaft speed Ω=6 krpm and unit load *W*/(*LD*)=1,726 kPa. Test data from Gaines [1] and predictions (with and without pad flexibility).

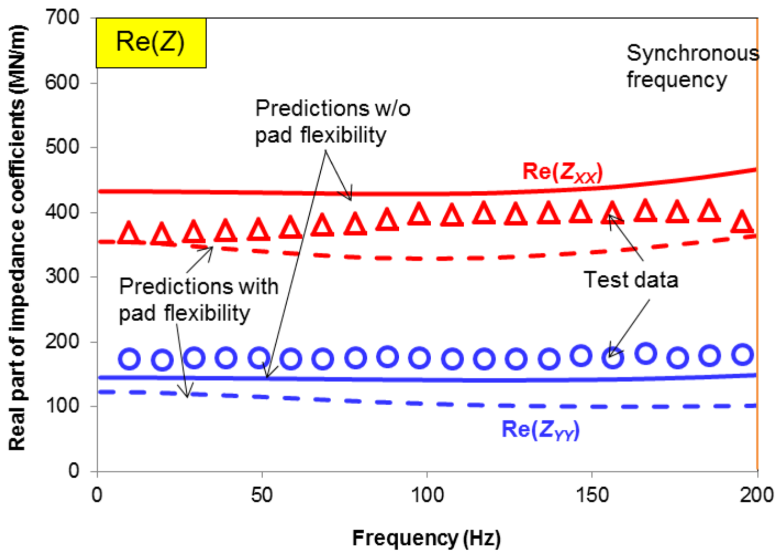

(a) Thin pad, t=8.5 mm

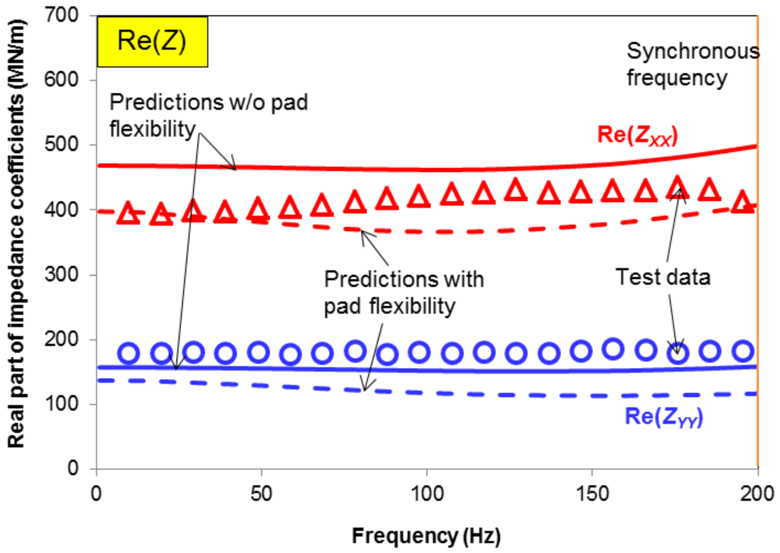

(b) Medium thickness pad, t=10 mm

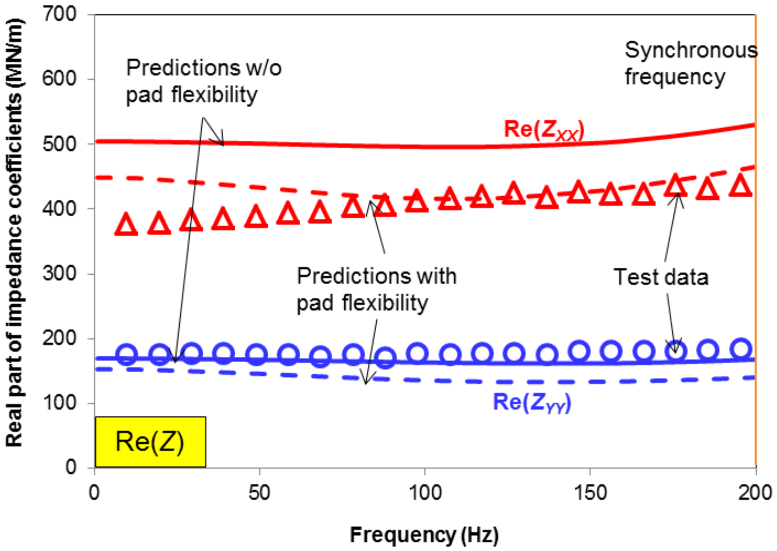

(c) Thick pad, t=11.5 mm

Figure 8 Real part of complex stiffnesses for TPJBs with pads of thickness (a) *t*=8.5 mm (b) *t*=10 mm (c) *t*=11.5 mm. Shaft speed Ω=12 krpm and unit load *W*/(*LD*)=1,726 kPa. Test data from Gaines [1] and predictions (with and without pad flexibility).

For the same static load condition and two journal speeds, Figs. 9 and 10 depict the experimental and predicted imaginary part of the bearing complex stiffnesses, Im(Z). In general, the bearing damping coefficient (C) is the slope of Im(Z)~ ωC. Both Im(Z_{XX}) and Im(Z_{YY}) from the experiments show a linear growth with frequency, i.e., a frequency independent C. Note Im(Z_{XX}) > Im(Z_{YY}). The predictions are in very good agreement with the experimental results for operation with the high shaft speed (12 krpm). On the other hand, for operation at 6 krpm, the predicted Im(Z_{XX}) is larger than the test results and evidences a reduction in growth on the high side of the excitation frequency range (ω>1.5Ω).

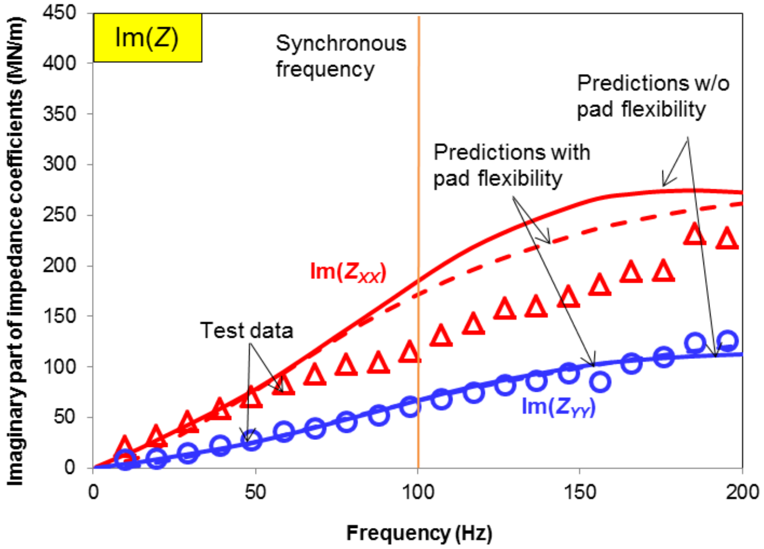

(a) Thin pad, t=8.5 mm

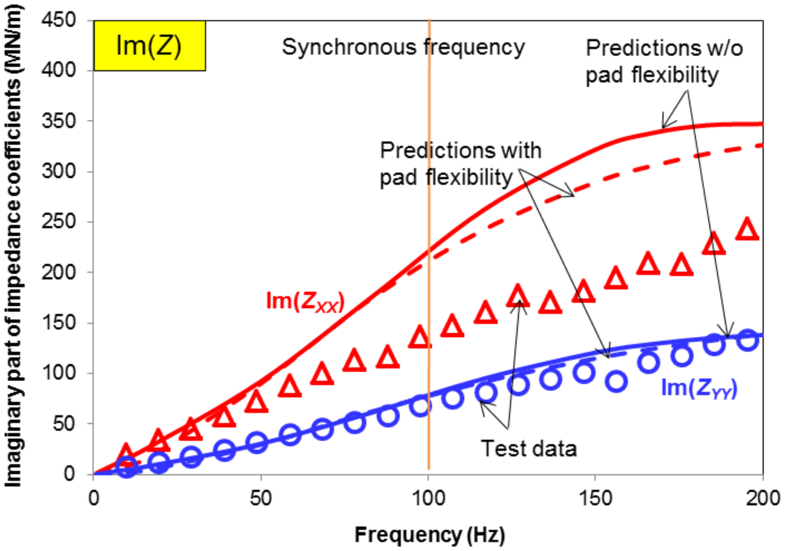

(b) Medium thickness pad, t=10 mm

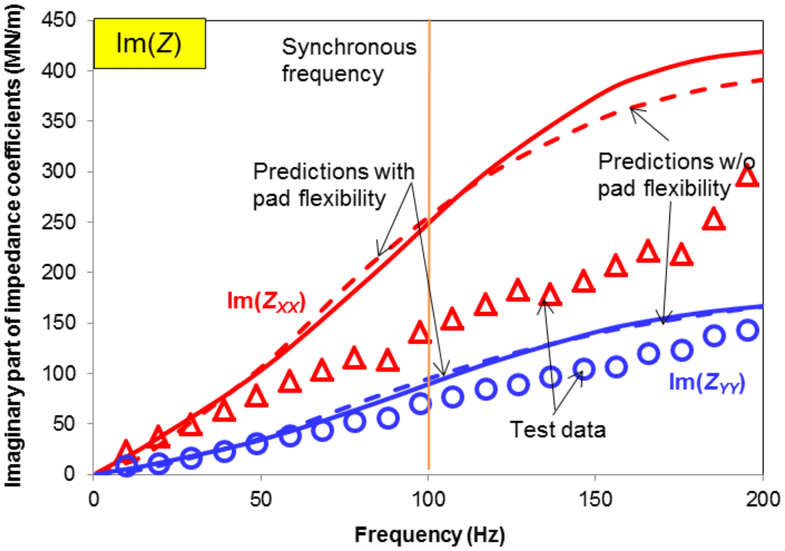

(c) Thick pad, t=11.5 mm

Figure 9 Imaginary part of complex stiffnesses for TPJBs with pads of thickness (a) *t*=8.5 mm (b) *t*=10 mm (c) *t*=11.5 mm. Shaft speed Ω=6 krpm and unit load *W*/(*LD*)=1,726 kPa. Test data from Gaines [1] and predictions (with and without pad flexibility).

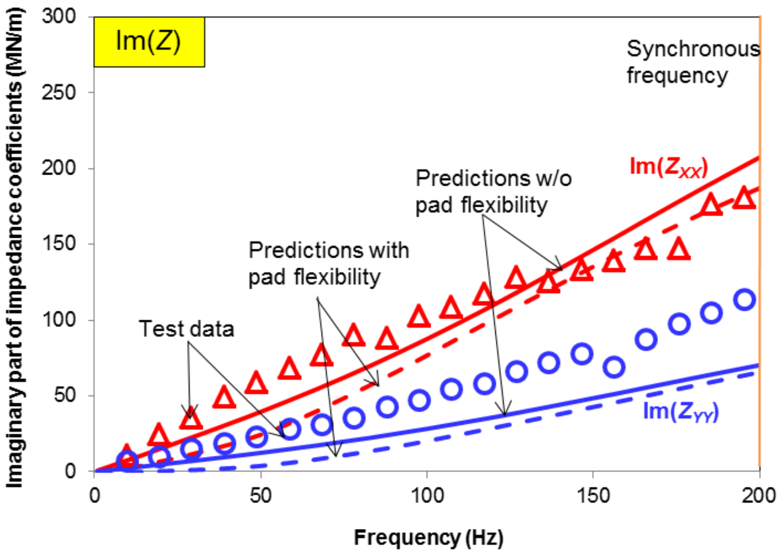

(a) Thin pad, t=8.5 mm

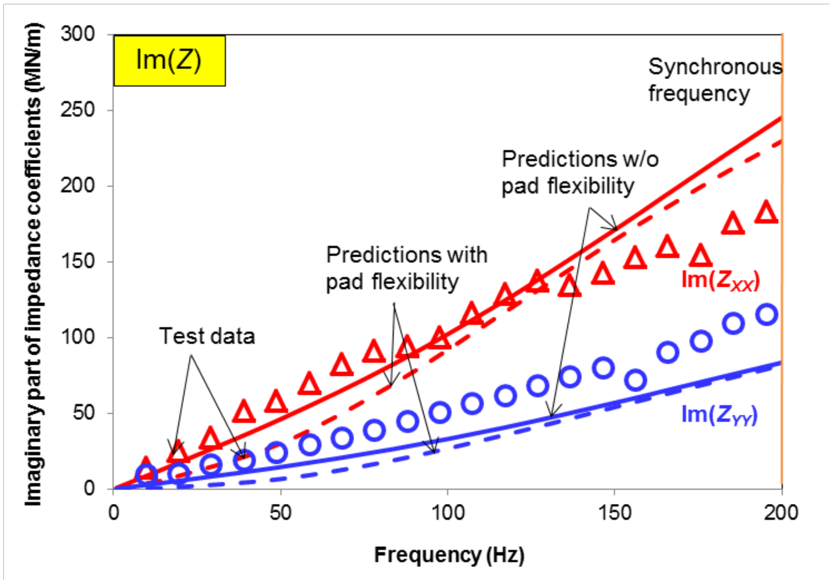

(b) Medium thickness pad, t=10 mm

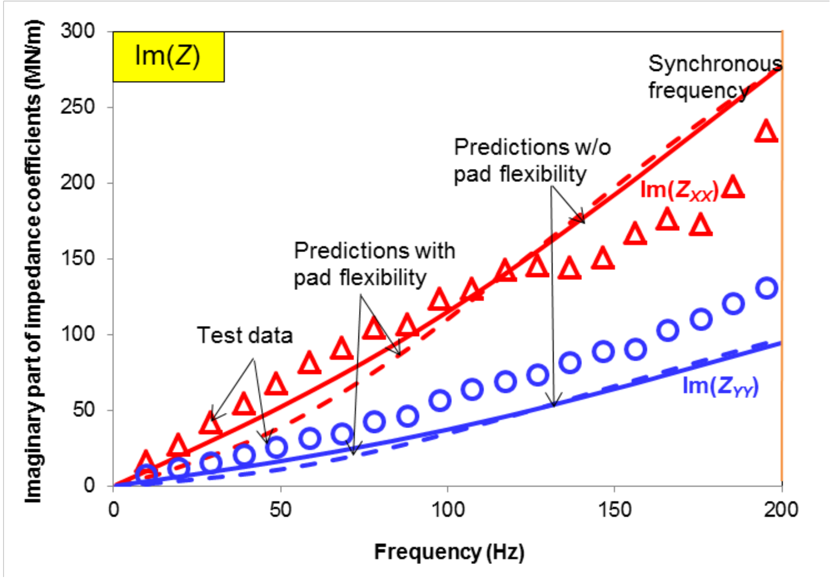

(c) Thick pad, t=11.5 mm

Figure 10 Imaginary part of complex stiffnesses for TPJBs with pads of thickness (a) *t*=8.5 mm (b) *t*=10 mm (c) *t*=11.5 mm. Shaft speed Ω=12 krpm and unit load *W*/(*LD*)=1,726 kPa. Test data from Gaines [1] and predictions (with and without pad flexibility).

Childs [23], supported by a myriad of experimental results from numerous test bearings [1,3-7], stresses that the (issue on) frequency dependency of force coefficients in TPJBs is settled with a simple [K,C,M] model. That is the curve fits Re(Z)←(K-$\omega^2 M$), Im(Z)←(*ωC*) deliver accurate stiffness (*K*), damping (*C*), and virtual mass (*M*) coefficients for confident use in rotor-bearing system stability analysis, i.e., a reliable estimation of the system logarithmic decrement.

Presently, define dimensionless dynamic force coefficients as [24],

$$k_{ij} = \frac{K_{ij} C_p}{W}, c_{ij} = \frac{C_{ij} \Omega C_p}{W}, m_{ij} = \frac{M_{ij} \Omega^2 C_p}{W} \quad _{i,j=X,Y} \tag{23}$$

Above C_p is the cold pad radial clearance, Ω is the rotor speed, and *W* is the static load applied to the bearing.

Figure 11 depicts the TPJB stiffness coefficients ($k_{XX} > k_{YY}$) versus unit load as identified (curve fits) from the measured and predicted complex stiffnesses (*Z*). The predicted stiffnesses correlate well with the test data at low loads, *W*/(*LD*)<1,032 kPa, but are underestimated at the highest load, *W*/(*LD*)=1,724 kPa. Note that pad flexibility increases the predicted k_{XX} and k_{YY} at low loads, *W*/(*LD*)<689 kPa, whereas it reduces the predicted k_{XX} and k_{YY} for high loads, *W*/(*LD*)>689 kPa. Predicted direct stiffnesses accounting for pad flexibility are up to 20% smaller than those assuming a rigid pad. As the pad thickness decreases from 11.5 mm to 8.5 mm, the predicted k_{XX} decreases by 21%.

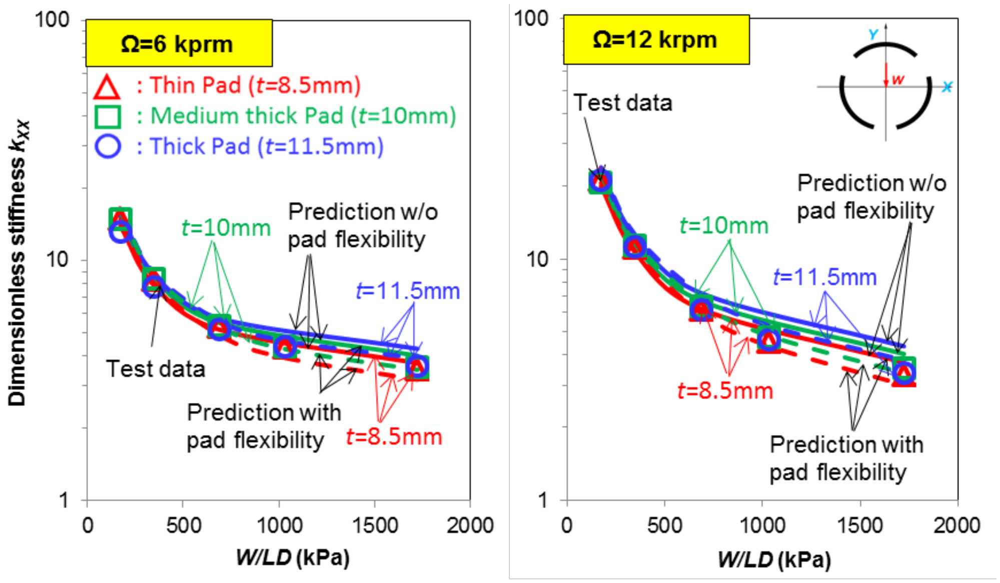

(a) k_{XX}

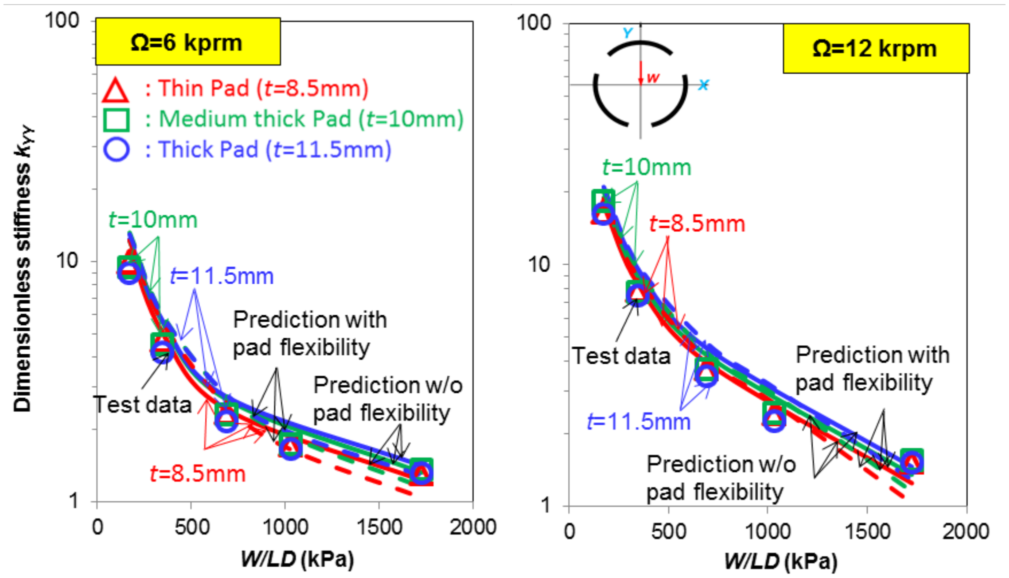

(b) k_{YY}

Figure 11 Direct stiffnesses (k_{XX} and k_{YY}) versus unit load and two shaft speeds. Predictions (without and with pad flexibility) and test data from Gaines [1]. Results shown for thin, medium and thick pads.

Interestingly enough, the direct stiffness (k_{YY}) along the static load direction (-Y) is significantly lower than the stiffness k_{XX}, in particular as the unit load increases. Fig. 12 depicts the film thickness and hydrodynamic pressure at the bearing mid-plane (z=½ L). Both the minimum film thickness and the maximum pressure are quite close to the X axis (θ=180^o), thus causing a large stiffness along the unloaded direction (X). That is, the stiffening effect is a result of the long arc extent of the bearing pads, 90^o.

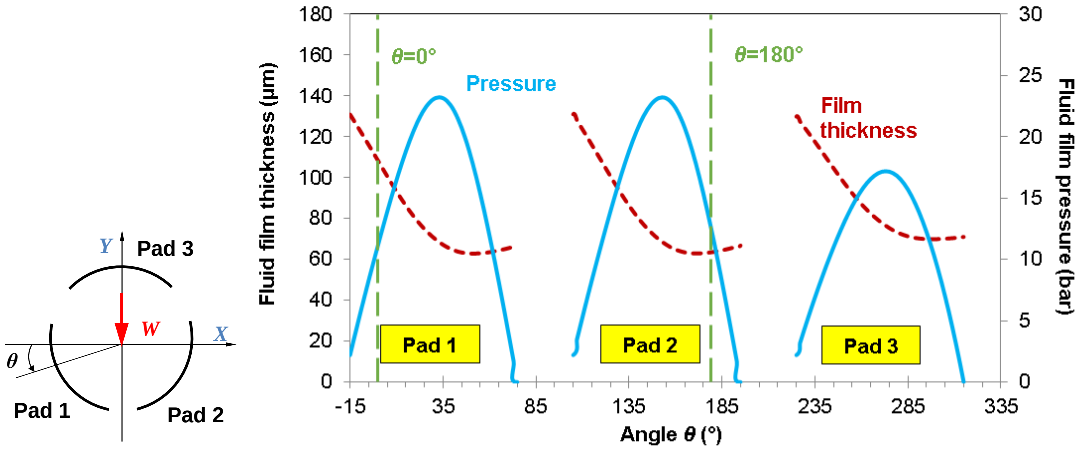

Figure 12 Predicted film pressure and film thickness at bearing mid plane. Operation with unit load *W*/(*LD*)=172 kPa and shaft speed Ω=6 krpm. Location of the maximum film pressure for each pad: θ_1=33° (pad 1), θ_2=153° (pad 2) and θ_3=273° (pad 3). Location of the minimum film thickness for each pad: θ_1=53° (pad 1), θ_2=173° (pad 2) and θ_3=301° (pad 3).

Figure 13 depicts the damping coefficients ($c_{XX} > c_{YY}$) versus unit load and for two shaft speeds. Pad flexibility reduces the predicted damping over the entire load range, 172 kPa< $W/(LD)$< 1,726 kPa. The experimental results show less differences for the three pad thicknesses than the model otherwise predicts. Predictions including pad flexibility deliver damping coefficients up to 46% lower than similar coefficients obtained with a rigid pads model. Reducing the pad thickness from 11.5 mm to 8.5 mm produces also a reduction of up to 50% in predicted direct damping. Note that the test results appear to agree with the predictions including pad flexibility for operation at the low speed of 6 krpm. The opposite argument applies to the test results at the high speed of 12 krpm, as they appear to agree with the predictions without pad flexibility.

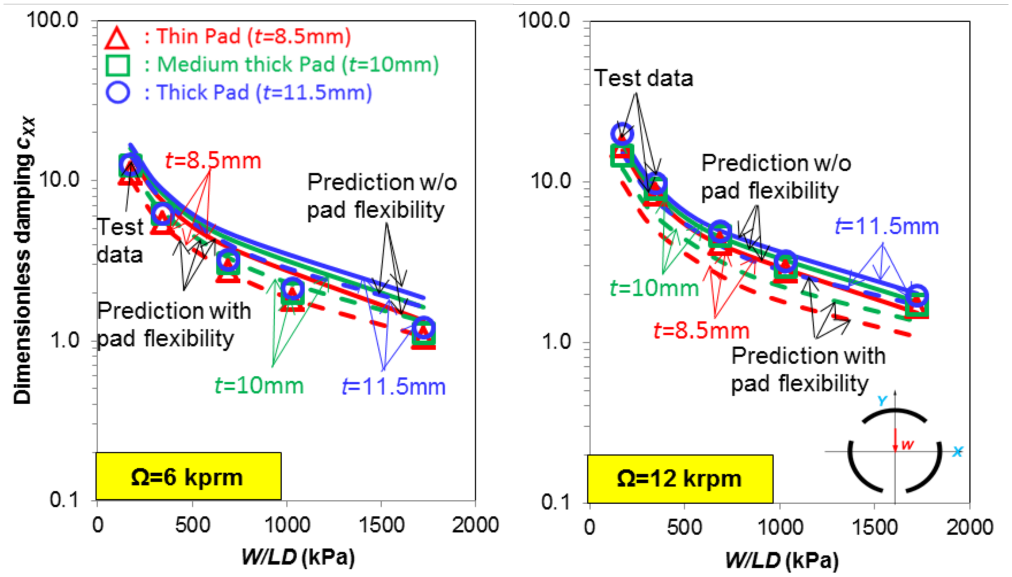

(a) c_{XX}

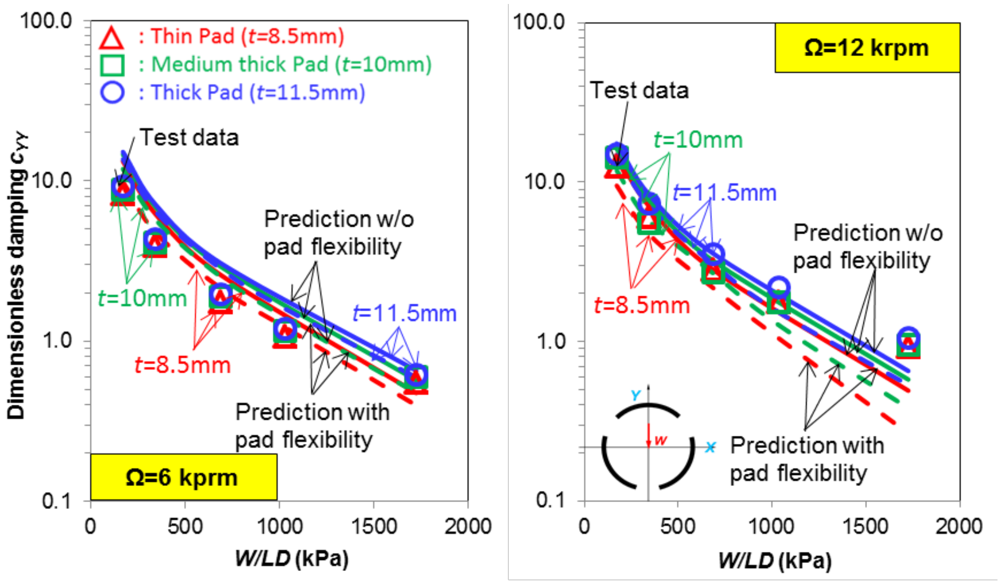

(b) c_{YY}

Figure 13 Direct damping coefficients (c_{XX} and c_{YY}) versus unit load and two shaft speeds. Predictions (without and with pad flexibility) and test data from Gaines [1]. Results shown for thin, medium and thick pads.

For completeness, Fig. 14 displays the virtual mass coefficients (m_{XX}, m_{YY}) versus unit load and operation at the low shaft speed of 6 krpm. The test results evidence lesser magnitudes for the added masses than the predictions otherwise show. The negative values denote the bearing dynamic stiffness hardens slightly as frequency increases, see Fig. 7. Most importantly, as the unit load increases, note (m_{XX}, m_{YY}) approach null values, thus indicating the real part of the complex stiffness (Z) does not show a frequency dependency. Similar results follow for operation at 12 krpm, hence those predictions are omitted for brevity. Note that in the sub-synchronous frequency range ($\omega<\Omega$), the virtual mass coefficients have a negligible impact on the dynamic stiffnesses (Re(Z)).

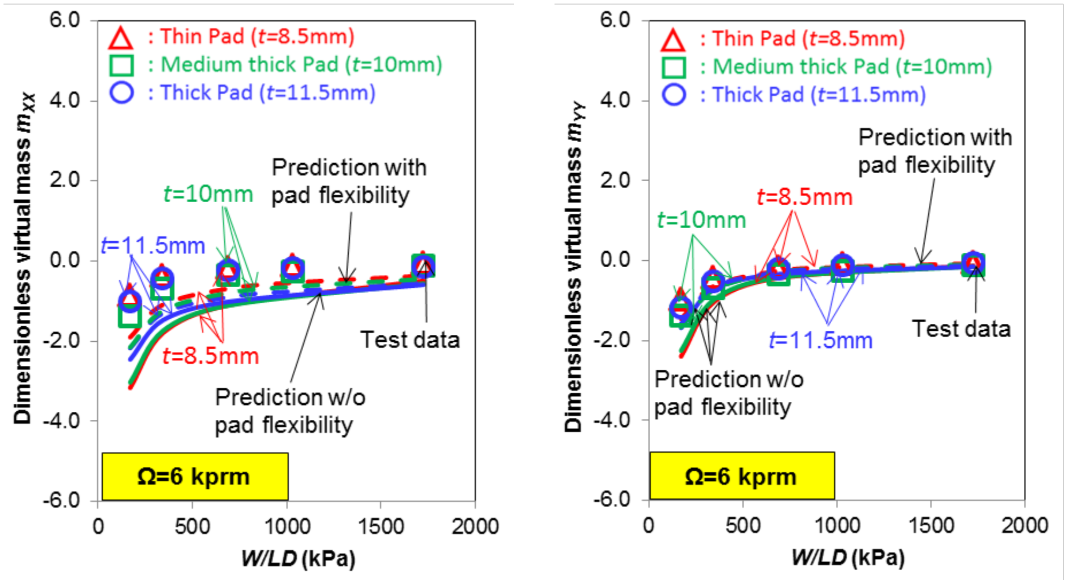

(a) m_{XX} (b)m_{YY}

Figure 14 Direct virtual mass coefficients (m_{XX} and m_{YY}) versus unit load and shaft speed= 6krpm. Predictions (without and with pad flexibility) and test data from Gaines [1]. Results shown for thin, medium and thick pads.

PARAMETRIC STUDY ON THE EFFECT OF PAD FLEXIBILITY ON TPJB PERFORMANCE

Nicholas [2] and Someya [24] produced useful design performance data for TPJBs. However, the original data do not include either pad or pivot flexibility. San Andrés *et al.* [9] complement the design data by accounting for pivot flexibility. This section further supplements TPJB performance characteristics with consideration of both pad and pivot flexibility for a three-pad TPJB operating under both LOP and LBP configurations. The bearing configurations selected reproduces the geometry of the bearings in Ref. [1] and also include variations in pad preload ($\overline{r}_p$). Table 3 presents the operating conditions and geometrical parameters for the TPJB model. The TPJB performance parameters are shown as a function of the Sommerfeld number (S), defined as

$$S = \frac{\mu_s NLD}{W}\left(\frac{R}{C_p}\right)^2 \tag{24}$$

where N=Ω/2π is the rotational speed and μ_s is the lubricant viscosity at the supply or inlet temperature.

Table 3 Cases to assess effect of pad flexibility on the performance of a TPJB.

Static specific load, $W/(LD)$	689 kPa
Journal speed, Ω	500 rpm – 12,000 rpm
Pad preload, $\overline{r}_p$	0, 0.25, 0.5
Pad thickness, t	Rigid pad, 8.5 mm, 11.5 mm
Pivot stiffness, K_{piv}	750 MN/m

Branagan [25] introduces several equations to estimate a pad elastic deformation due to a bending moment (M). He suggests as adequate,

$$u_t = -\frac{M}{AE}(r-1)\frac{4\left[1-r^2\left(1-2\log r\right)\right]}{\left[r^2-1\right]^2-\left(2r\cdot\log r\right)^2} \tag{25}$$

with $r=(R+t)/R$ and A is the cross-sectional area of a pad. Nilsson [10] already notes that a pad with a long arc length is more flexible; alas, Branagan's equation does not account for pad arc length. In addition, Eq. (25) neglects the Babbitt layer that makes a pad more flexible.

Prior to presenting predictions, let's define a suitable pad bending stiffness (K_{pad}). Since a typical bearing pad integrates a thick base material (steel) and a Babbitt layer, define an equivalent elastic modulus as [26]

$$E_{eq} = \frac{E_1\left(\tfrac{1}{2}t_1 - R_n\right)t_1 + E_2\left(\tfrac{1}{2}t_2 - R_n\right)t_2}{\left(\tfrac{1}{2}t \;- R_{eq}\right)t} \tag{26}$$

where E_1 and E_2 are the elastic moduli of materials 1 and 2, t_1 and t_2 are thicknesses, and $t=t_1+t_2$ is the pad thickness. Above, R_n is the neutral axis of a pad (beam) of two materials, whereas R_{eq} is the neutral axis of a pad made of one material,

$$R_n = \frac{E_1 t_1 + E_2 t_2}{E_1 \ln\left(1 + {t_1}/{R}\right) + E_2 \ln\left(1 + {t_2}/{(R+t_1)}\right)}, R_{eq} = \frac{t}{\ln\left(1 + {t}/{R}\right)} \tag{27}$$

A simple elasticity analysis, based on information gathered from Refs. [27-30], takes a pad as a curved beam and apply a uniform pressure ($\bar{p}$) to determine the radial deformation at its edge (u_t),

$$\frac{u_t}{\bar{p}} = \frac{1}{2}\cdot\frac{LR_{eq}^4}{E_{eq}I}\left[\left(\cos\frac{\Theta_P}{2} - 2\right)\cos\frac{\Theta_P}{2} + 1\right] \tag{28}$$

where Θ_P is the pad arc extent and $I=Lt^3/12$ is the area moment of inertia. See Ref. [31] for details on the derivation of the equations above. Define a dimensionless pad stiffness as

$$k_{pad} = \frac{C_p}{W/(LD)}K_{pad} = \frac{C_p}{u_t}\cdot\frac{\bar{p}LD}{W} = \frac{E_{eq}I}{R_{eq}^3}\cdot\frac{D}{R_{eq}}\frac{2}{\left[\left(\cos\frac{\Theta_P}{2} - 2\right)\cos\frac{\Theta_P}{2} + 1\right]}\left(\frac{C_p}{W}\right) \tag{29}$$

Thus, $k_{pad} = \infty$, 3.15 and 7.33, for a rigid pad, a pad with a thickness of 8.5 mm, and another pad with a thickness of 11.5 mm, respectively[5]. Note that the k_{pad} is nearly proportional to the cube of a pad thickness, ~t^3. Incidentally, in the analysis, the dimensionless pivot stiffness (k_{piv}) is, with K_{piv}=750 MN/m,

---

[5] Recall a pad has a 1.5 mm Babbitt layer.

$$k_{piv} = \frac{K_{piv} C_p}{W_{\max}} = 16 \tag{30}$$

For the LBP and LOP configurations and varying pad preload, $\overline{r}_p$ =0, 0.25, 0.5, Fig. 15 depicts the journal eccentricity versus Sommerfeld number (S). At a large S and as the pad flexibility increases (k_{pad} decreases), the journal eccentricity decreases greatly for the LBP bearing with a null pad preload and the LOP bearing with 0.25 preload, in particular.

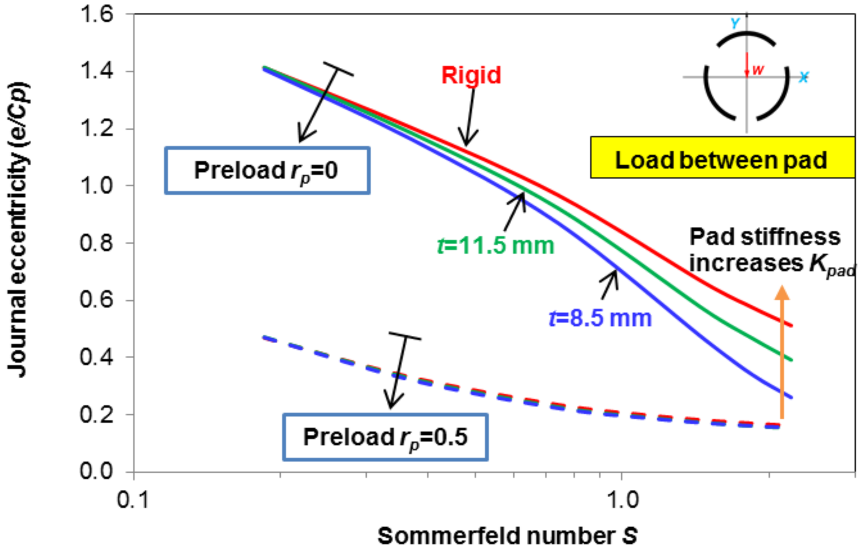

(a) LBP, $\overline{r}_p$ =0 & 0.5

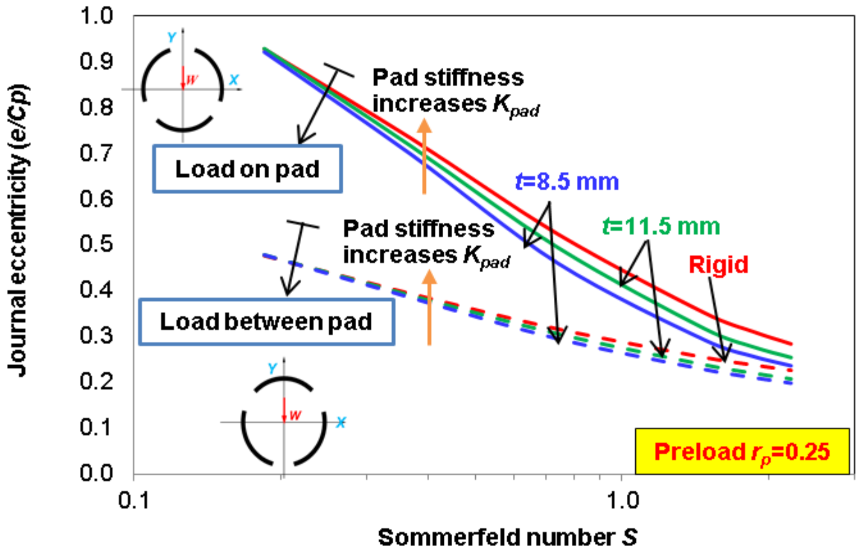

(b) LOP & LBP, $\overline{r}_p$ =0.25

Figure 15 Three-pad TPJB journal eccentricity (e/C_p) vs. Sommerfeld number (S). Pad stiffness k_{pad} = 3.15, 7.33, ∞ (rigid) and k_{piv} = 16. Pad preload varies: LBP and LOP configurations. Specific load $W/(LD)$=689 kPa, rotor speed Ω=500 rpm to 12,000 rpm.

Figure 16 depicts the drag friction coefficient, $f=T_{orque}/(R_J W)$ increasing proportionally with S for both the LBP and LOP configurations, the bearing with the largest preload having more drag. Pad flexibility has no effect on f, hence has no influence on the bearing drag power losses.

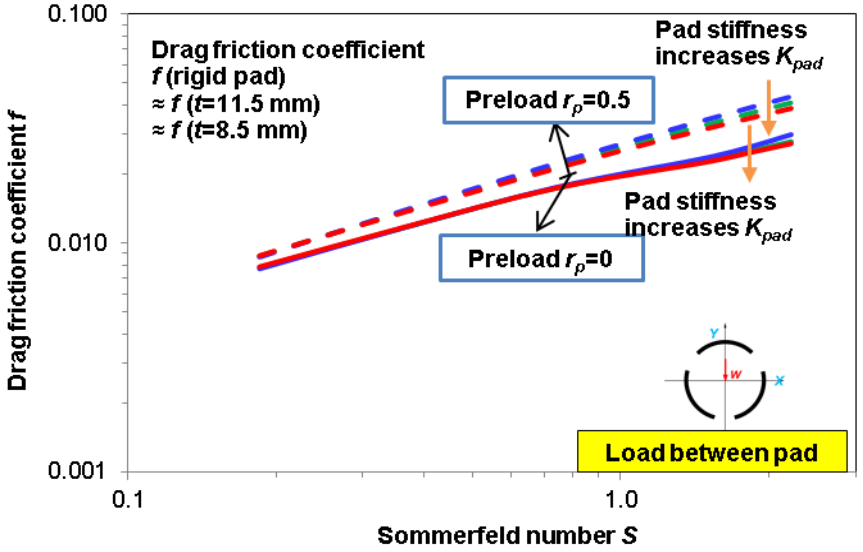

(a) LBP, $\bar{r}_p$ =0 & 0.5

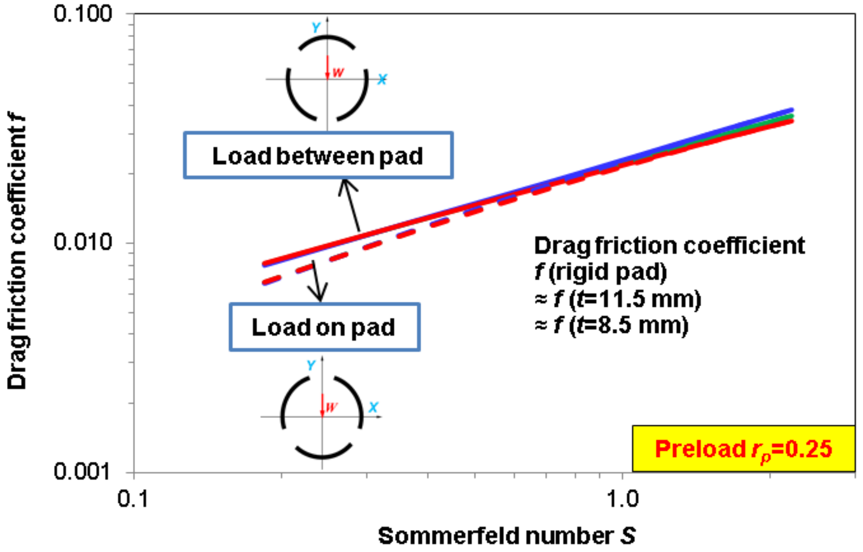

(b) LOP & LBP, $\bar{r}_p$ =0.25

Figure 16 Three-pad TPJB drag friction coefficient (*f*) vs. Sommerfeld number. Pad stiffness k_{pad} = 3.15, 7.33, ∞ (rigid) and k_{piv} = 16. Pad preload varies: LBP and LOP configurations. Specific load *W*/(*LD*)=689 kPa, rotor speed Ω=500 rpm to 12,000 rpm.

Figures 17 and 18 show pad flexibility reduces the stiffness coefficients (k_{XX}, k_{YY}). For the LBP bearing, pad flexibility increases slightly k_{YY} by 3% at S>1. Recall that Fig.

11 depicts an increase in bearing stiffnesses due to pad flexibility at a smaller unit load. For the LOP TPJB, the stiffness along the unloaded direction (k_{XX}) is one order of magnitude lesser than the stiffness along the load direction (k_{YY}) at a Sommerfeld number less than 1 ($S<1$). For both the TPJBs under LBP and LOP configurations, pad flexibility slightly increases k_{YY} at a large Sommerfeld number ($S>0.8$).

For the LBP TPJB with 0.5 preload and the LOP TPJB with 0.25 preload, k_{XX} and k_{YY} increase with S. For the LPB TPJB with null preload, k_{XX} and k_{YY} decrease with an increase in S.

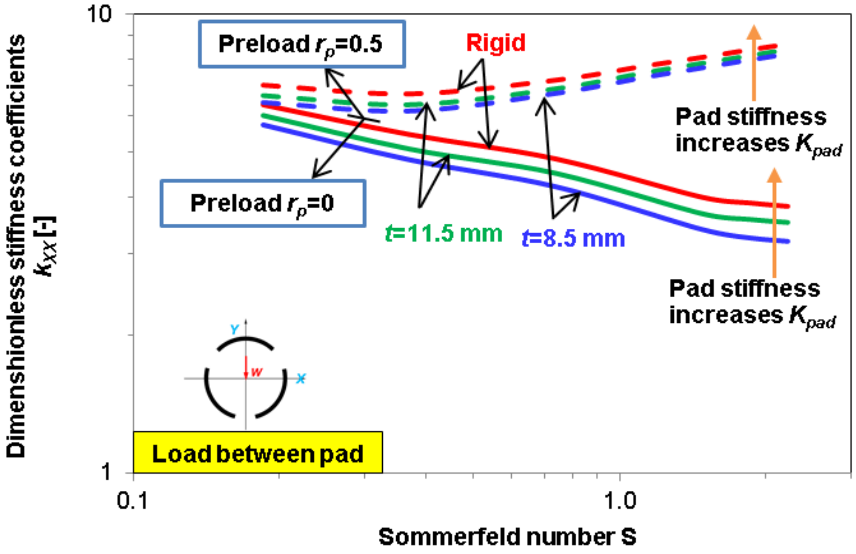

(a) k_{XX}

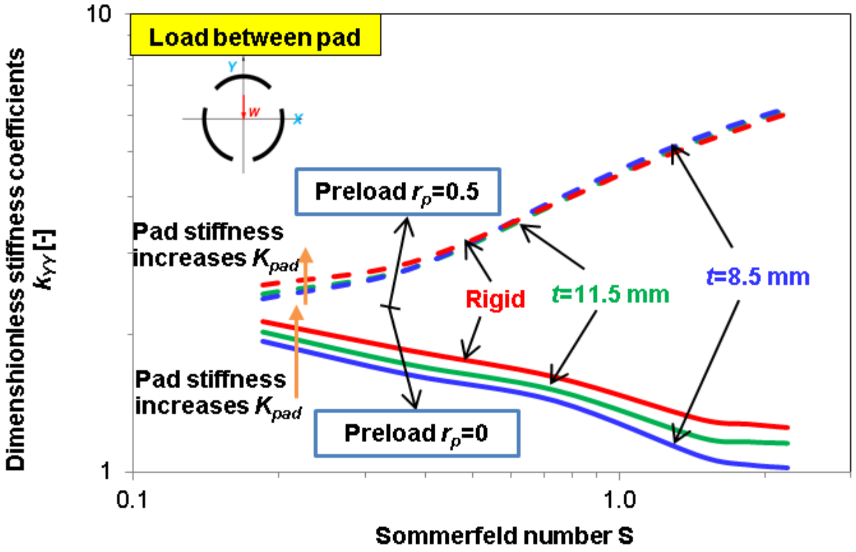

(b) k_{YY}

Figure 17 Three-pad TPJB stiffness coefficients (k_{XX}, k_{YY}) vs. Sommerfeld number (S). Pad stiffness k_{pad} = 3.15, 7.33, ∞ (rigid) and k_{piv} = 16. Pad preload $\overline{r}_p$ =0, 0.5: LBP configuration. Specific load $W/(LD)$=689 kPa, rotor speed Ω=500 rpm to 12,000 rpm.

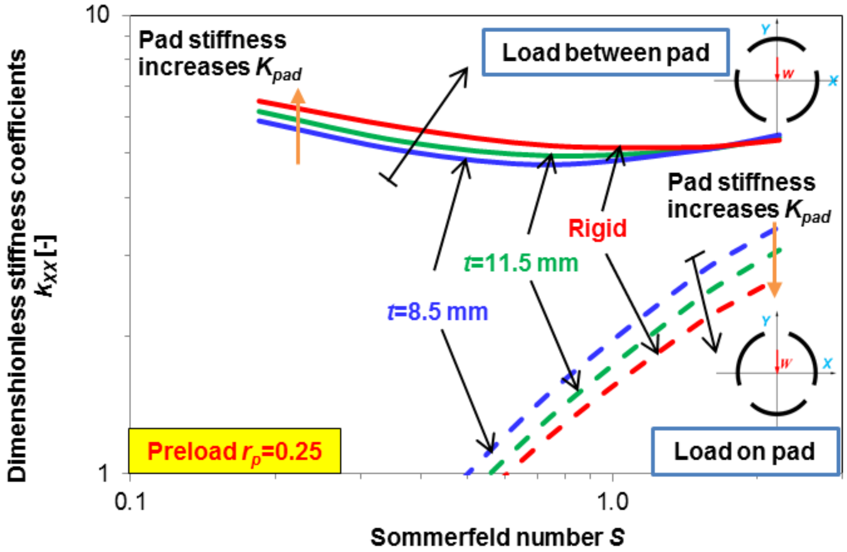

(a) k_{XX}

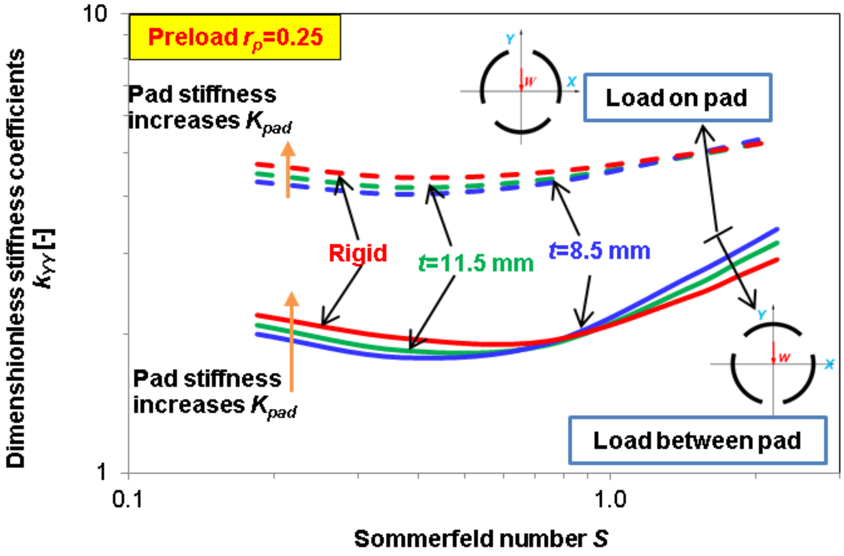

(b) k_{YY}

Figure 18 Three-pad TPJB stiffness coefficients (k_{XX}, k_{YY}) vs. Sommerfeld number (S). Pad stiffness k_{pad} = 3.15, 7.33, ∞ (rigid) and k_{piv} = 16. Pad preload $\overline{r}_p$ =0.25: LOP and LBP configurations. Specific load $W/(LD)$=689 kPa, rotor speed Ω=500 rpm to 12,000 rpm.

Figures 19 and 20 show the damping coefficients (c_{XX}, c_{YY}) versus Sommerfeld number (S) for both LBP and LOP bearings and with pad preload $\overline{r}_p$ = 0, 0.25, 0.5. The dimensionless damping coefficients increase with S; however, for the LBP TPJB with null preload, c_{YY} decreases on $0.74<S<1.08$. As pad flexibility increases, the damping coefficients decrease dramatically by up to 33%, in particular for large Sommerfeld number (S>1.0). Pad flexibility has a more pronounced effect on the damping coefficients of a LBP TPJB with null pad preload ($\overline{r}_p$ =0).

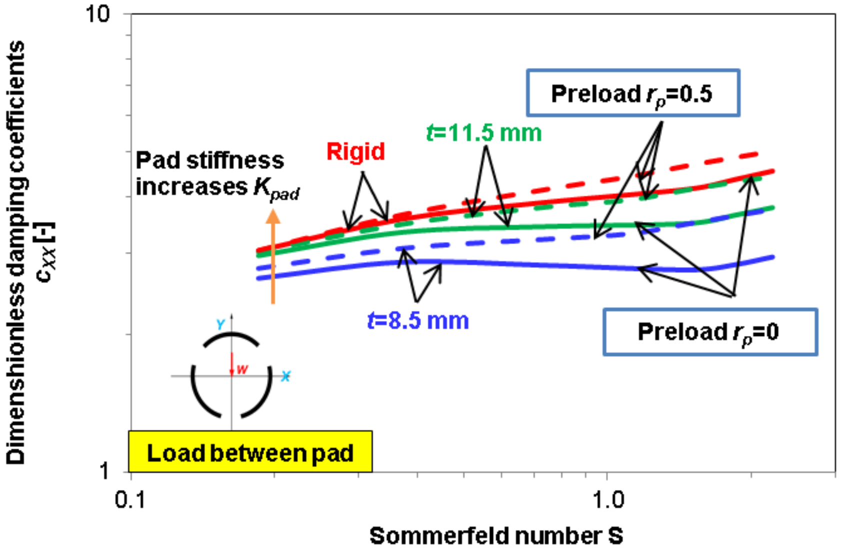

(a) c_{XX}

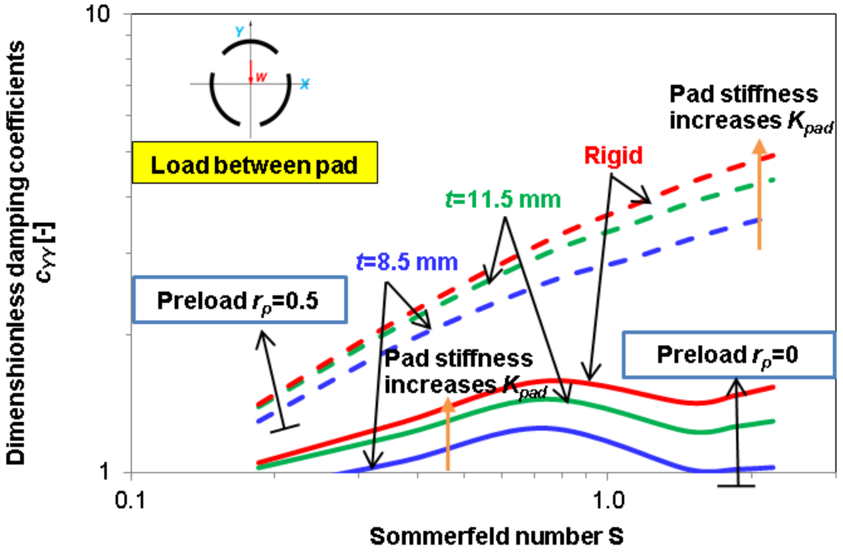

(b) c_{YY}

Figure 19 Three-pad TPJB damping coefficients (c_{XX}, c_{YY}) vs. Sommerfeld number. Pad stiffness k_{pad} = 3.15, 7.33, ∞ (rigid) and k_{piv} = 16. Pad preload $\bar{r}_p$ =0, 0.5: LBP configuration. Specific load $W/(LD)$=689 kPa, rotor speed Ω=500 rpm to 12,000 rpm.

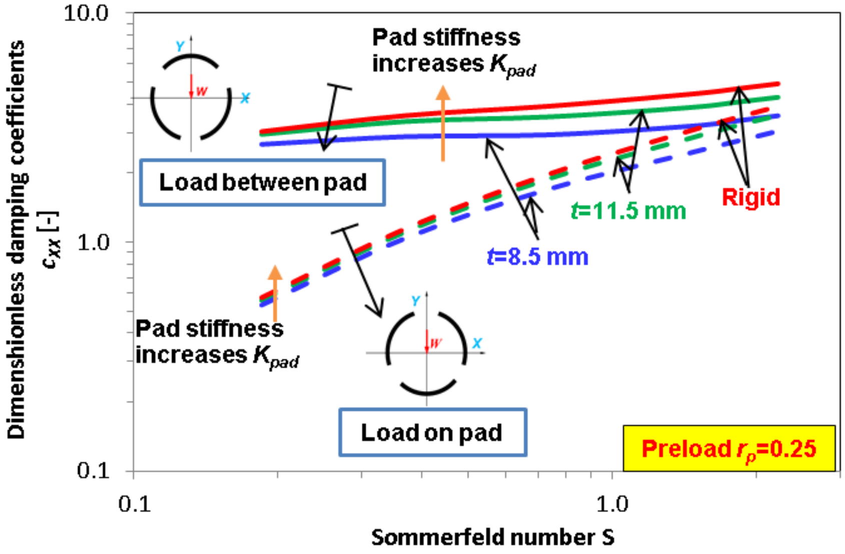

(a) c_{XX}

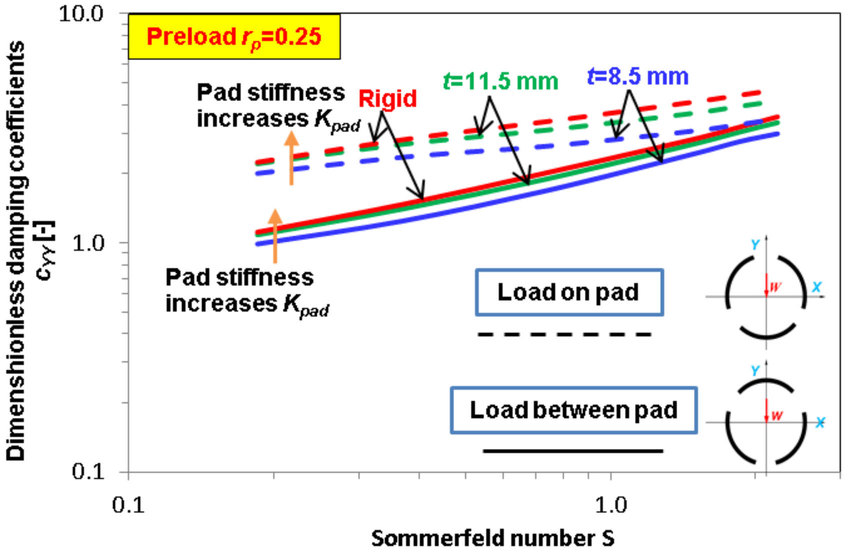

(b) c_{YY}

Figure 20 Three-pad TPJB damping coefficients (c_{XX}, c_{YY}) vs. Sommerfeld number (S). Pad stiffness k_{pad} = 3.15, 7.33, ∞ (rigid) and k_{piv} = 16. Pad preload $\overline{r}_p$ =0.25: LOP and LBP configurations. Specific load $W/(LD)$=689 kPa, rotor speed Ω=500 rpm to 12,000 rpm.

Figures 21 and 22 depict the virtual mass coefficients (m) versus Sommerfeld number (S). In general m<0 denotes the bearing will stiffen as the excitation frequency increases. Pad flexibility has a more pronounced effect on m_{YY}, in particular for the LBP bearing with preload equal to 0 and 0.25. Though the coefficients (*m*) do not approach zero as *S* increases, the virtual mass coefficients (M_{YY}, M_{YY}) approach to zero at a large *S*, thus indicating the dynamic stiffness Re(Z_{YY}) is frequency independent.

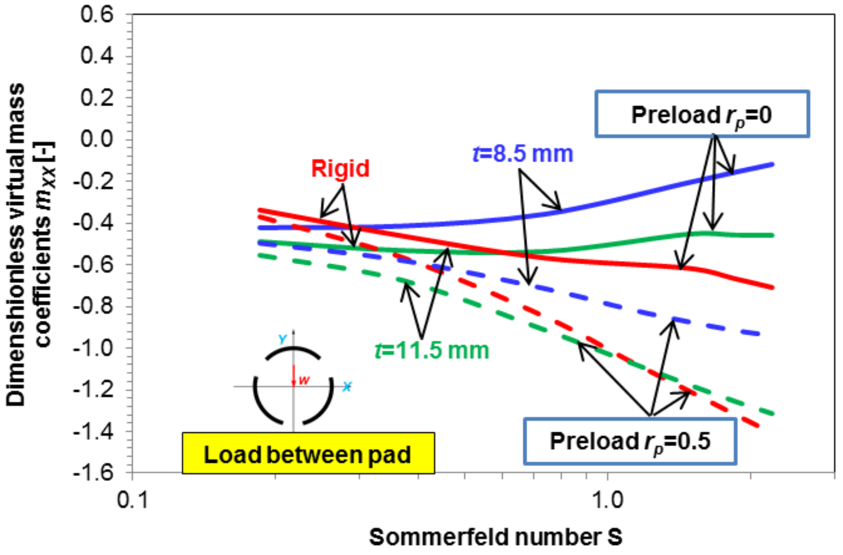

(a) m_{XX}

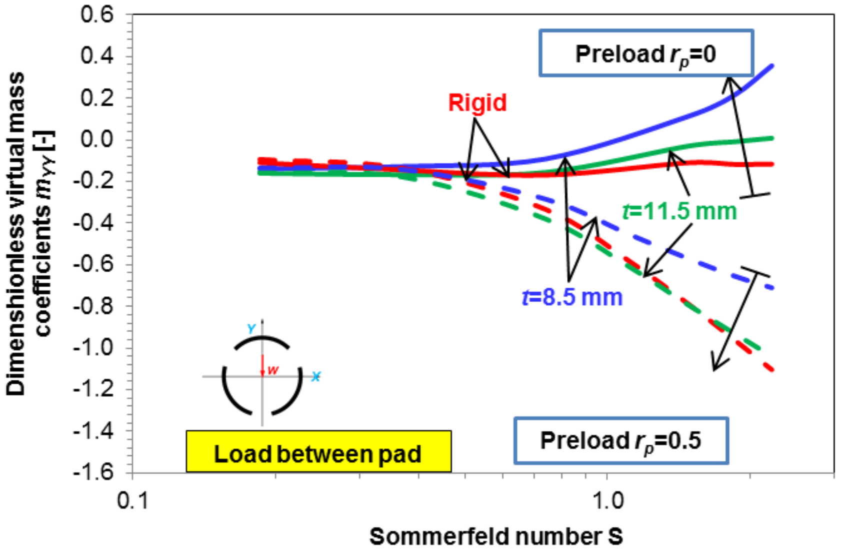

(b) m_{YY}

Figure 21 Three-pad TPJB virtual mass coefficients (m_{XX}**,** m_{YY}**) vs. Sommerfeld number (*S*). Pad stiffness** k_{pad} **= 3.15, 7.33, ∞ (rigid) and** k_{piv} **= 16. Pad preload** $\overline{r}_p$ **=0, 0.5: LBP configuration. Specific load *W*/(*LD*)=689 kPa, rotor speed Ω=500 rpm to 12,000 rpm.**

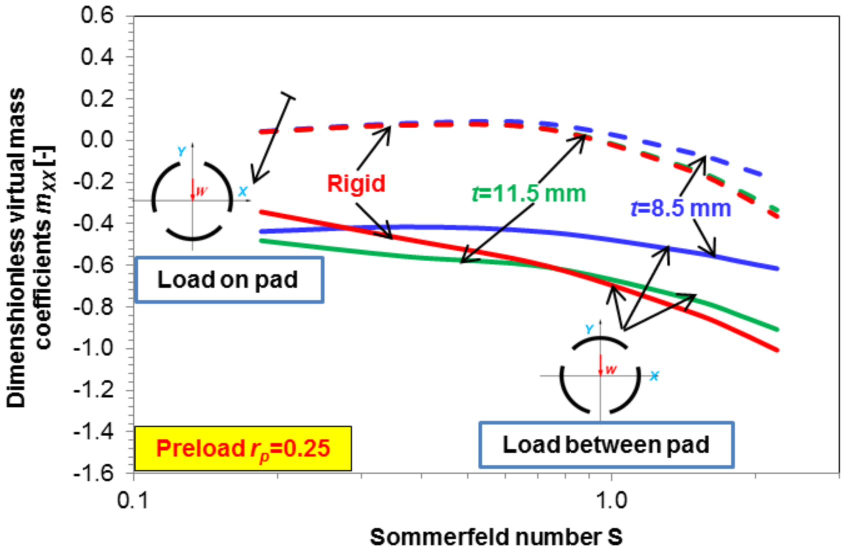

(a) m_{XX}

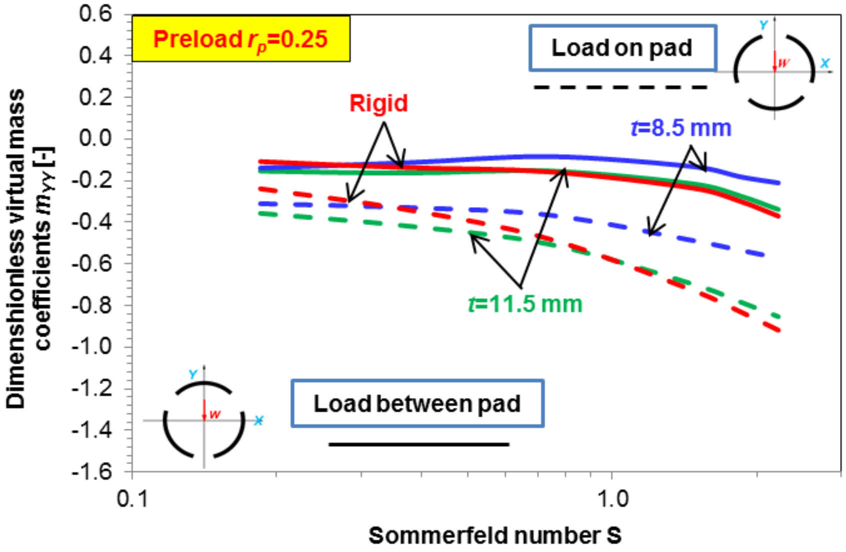

(b) m_{YY}

Figure 22 Three-pad TPJB damping coefficients (m_{XX}, m_{YY}) vs. Sommerfeld number (S). Pad stiffness k_{pad} = 3.15, 7.33, ∞ (rigid) and k_{piv} = 16. Pad preload $\overline{r}_p$ =0.25: LOP and LBP configurations. Specific load $W/(LD)$=689 kPa, rotor speed Ω=500 rpm to 12,000 rpm.

Guide to get a pad structural stiffness matrix in ANSYS

Yingkun Li
Research Assistant
Dr. Luis San Andrés
Mast-Childs Professor

Introduction

Those slides give the detail of each step to get the stiffness matrix from ANSYS©.

The title of each slide shows the name of the dialog box shown in the slide

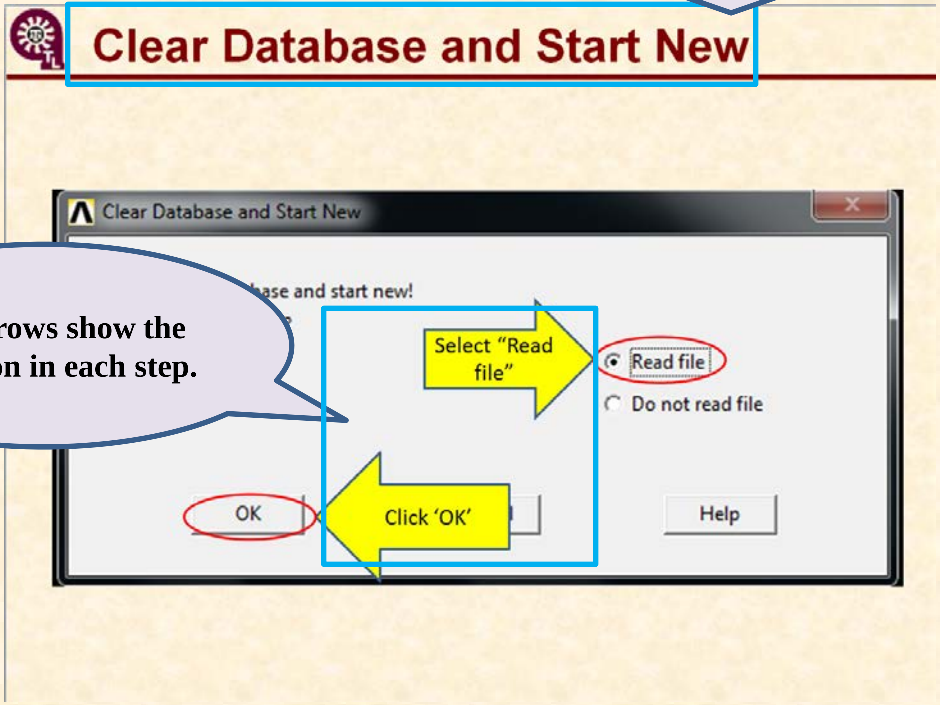

Clear Database and Start New

Clear Database and Start New

...ase and start new!

Select "Read file"

● Read file

○ Do not read file

Click 'OK'

The arrows show the operation in each step.

Introduction

This guide uses a pad model shown on the right to help to illustrate the operations.
The table below lists the geometry and material properties.

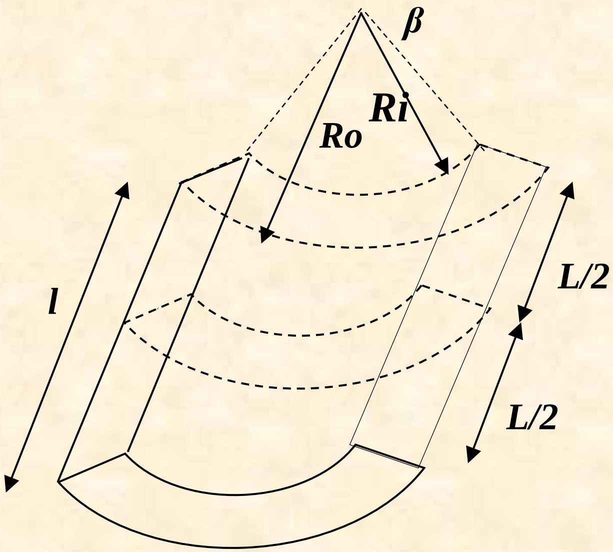

Figure The shape of the pad model

Table Pad geometry and material parameters

Inner radius (R_i)	0.050921m
Outer radius (R_o)	0.076321m
Axial length of the pad (*l*)	0.0559m
Angular amplitude of pad (*β*)	58.9°
Pivot position	0.5
Young’s modulus (*E*)	2.0×10^{11} Pa
Poisson’s ratio	0.3

Main interface

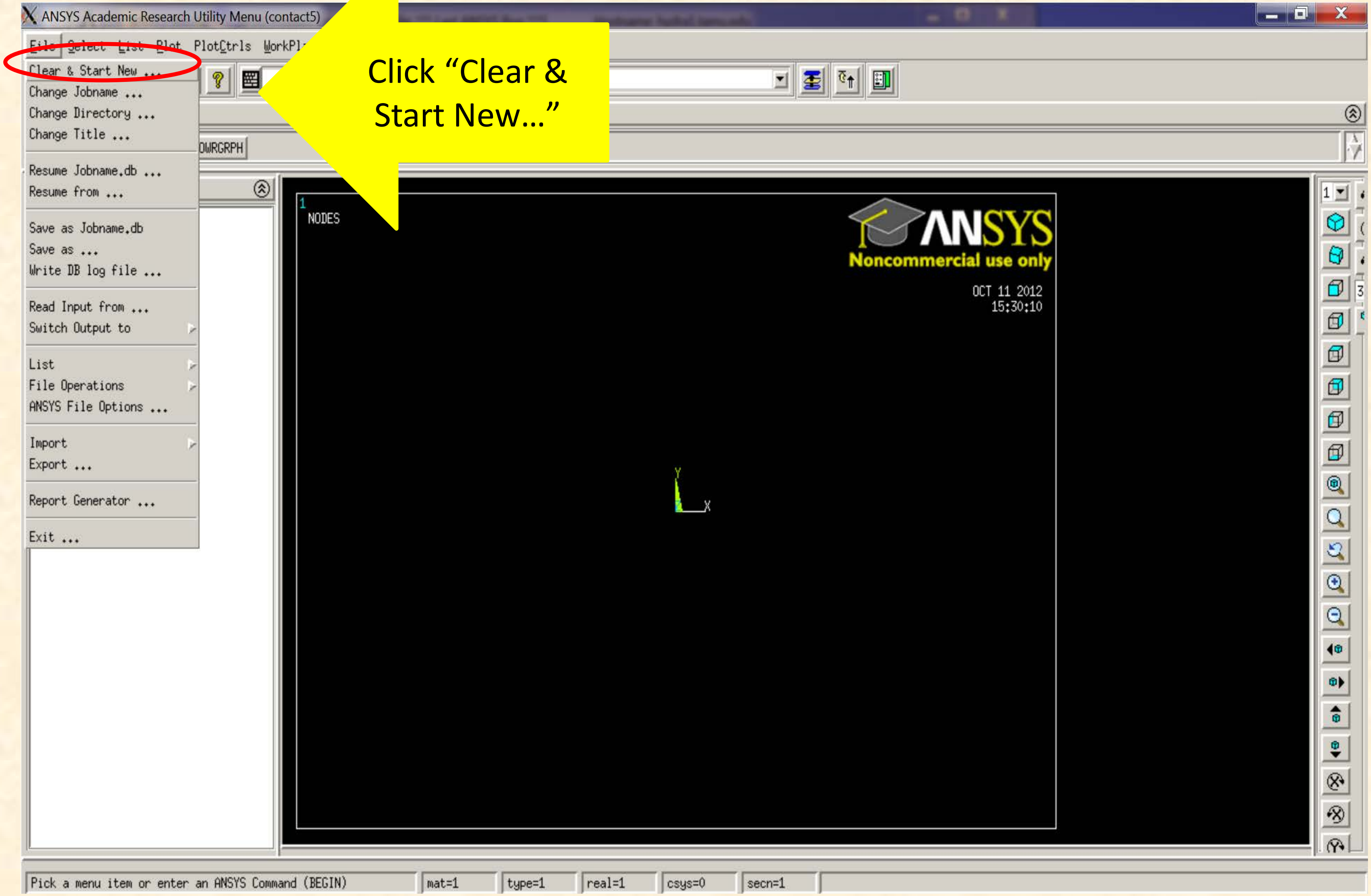
ANSYS Academic Research Utility Menu (contact5)
File
Select
List
Plot
PlotCtrls
WorkPl
Clear & Start New ...
Change Jobname ...
Change Directory ...
Change Title ...
Resume Jobname.db ...
Resume from ...
Save as Jobname.db
Save as ...
Write DB log file ...
Read Input from ...
Switch Output to
List
File Operations
ANSYS File Options ...
Import
Export ...
Report Generator ...
Exit ...
OWRGRPH
1
NODES
ANSYS
Noncommercial use only
OCT 11 2012
15:30:10
Y
X
Pick a menu item or enter an ANSYS Command (BEGIN)
mat=1
type=1
real=1
csys=0
secn=1

Click “Clear & Start New…”

Clear Database and Start New

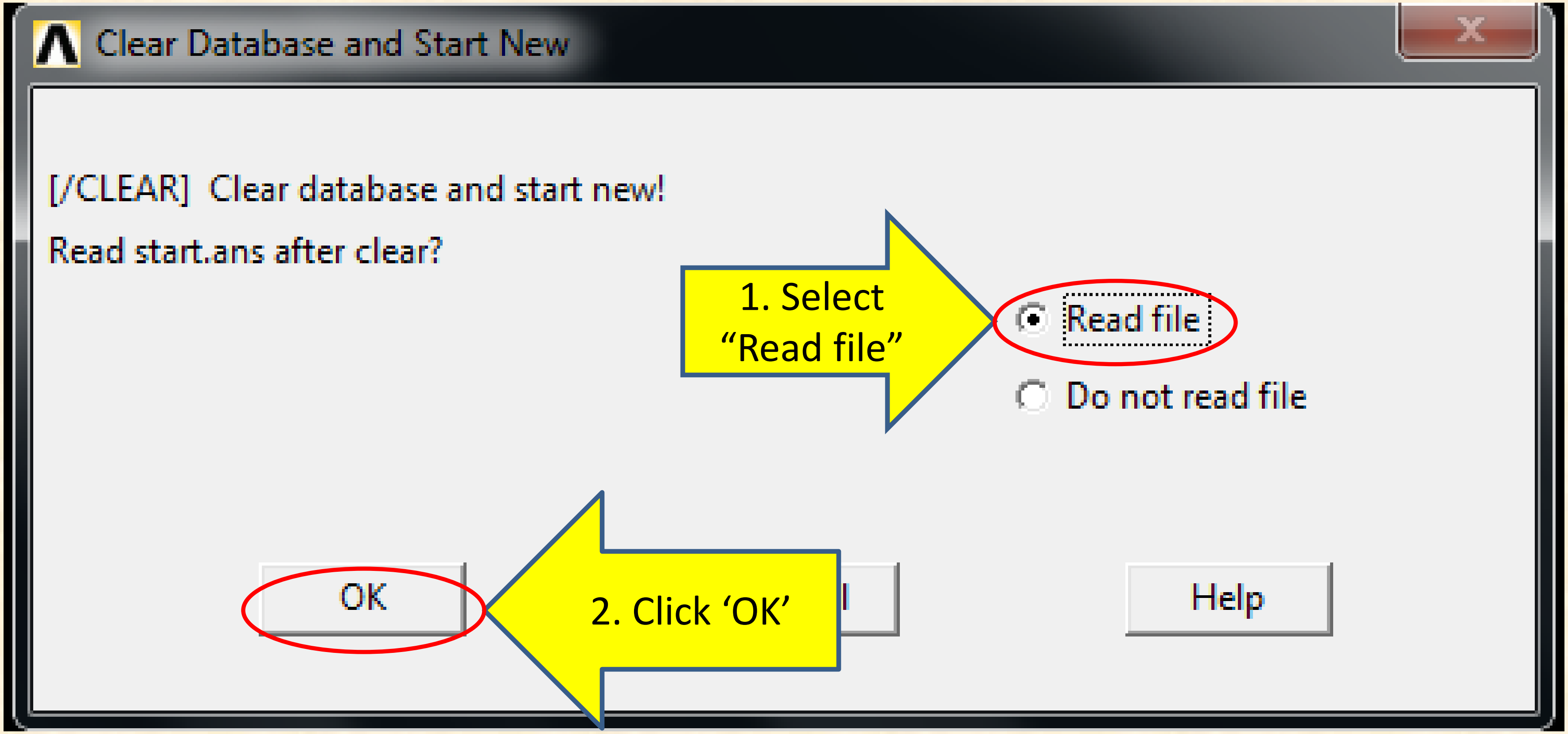

Clear Database and Start New

[/CLEAR] Clear database and start new!

Read start.ans after clear?

● Read file

○ Do not read file

1. Select “Read file”

2. Click ‘OK’

Verify

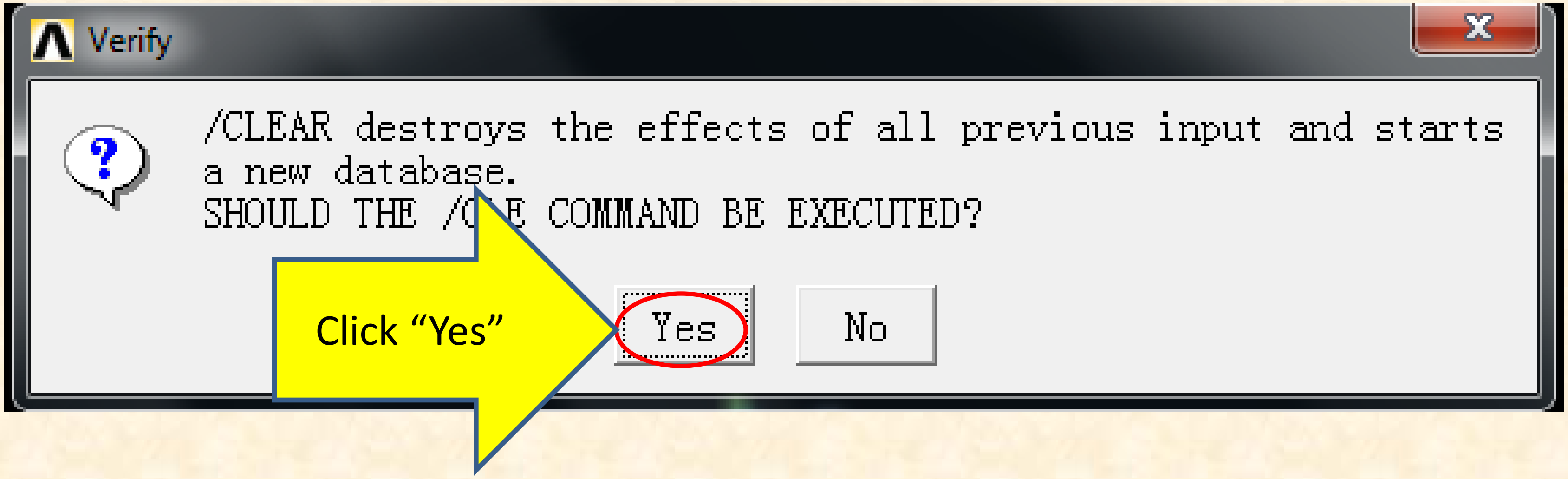

/CLEAR destroys the effects of all previous input and starts a new database.
SHOULD THE /CLE COMMAND BE EXECUTED?

Click “Yes”

Main interface

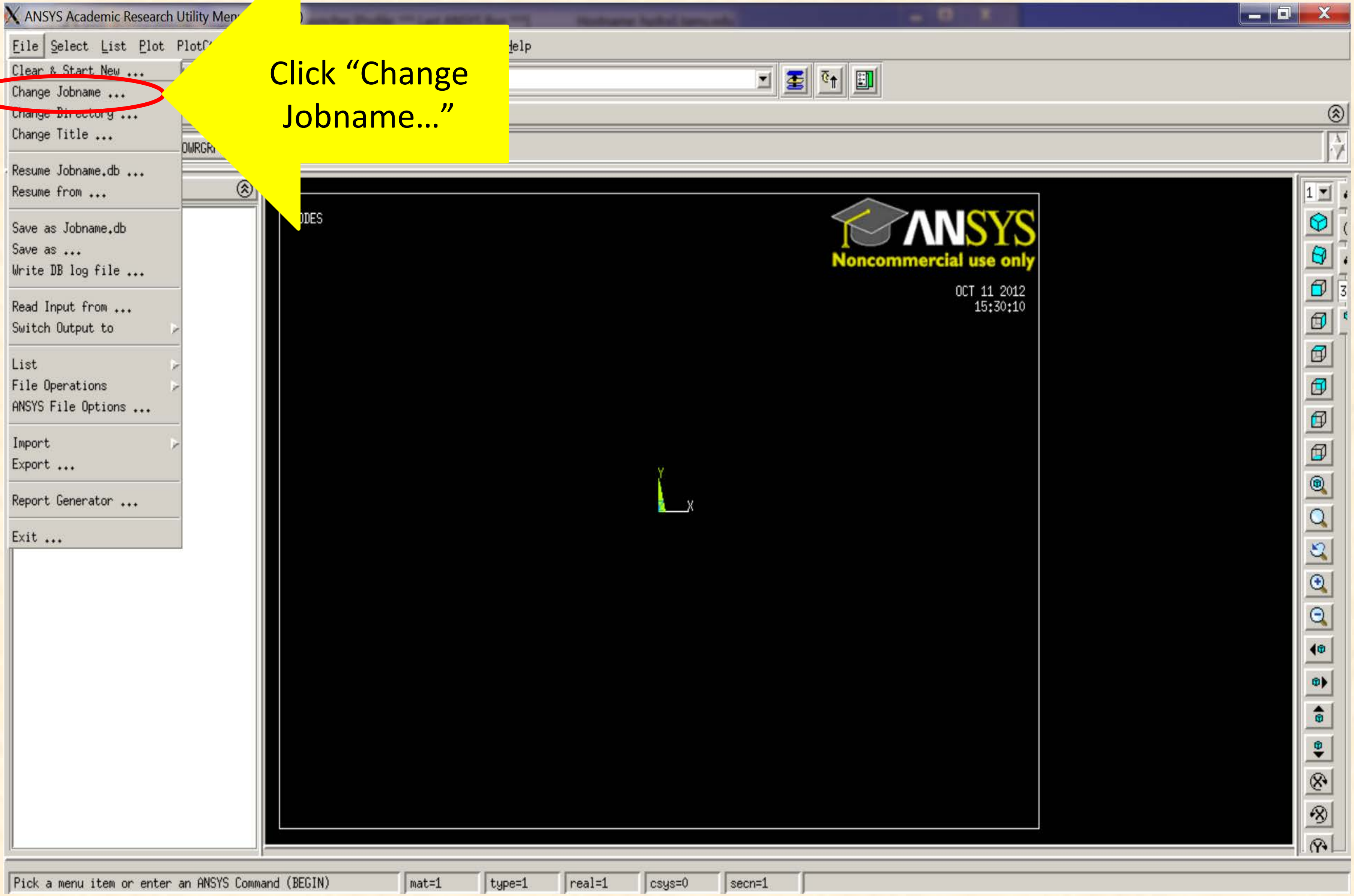
ANSYS Academic Research Utility Menu
File
Select
List
Plot
Help
Clear & Start New ...
Change Jobname ...
Change Directory ...
Change Title ...
Resume Jobname.db ...
Resume from ...
Save as Jobname.db
Save as ...
Write DB log file ...
Read Input from ...
Switch Output to
List
File Operations
ANSYS File Options ...
Import
Export ...
Report Generator ...
Exit ...
ANSYS
Noncommercial use only
OCT 11 2012
15:30:10
Y
X

Click "Change Jobname…"

Pick a menu item or enter an ANSYS Command (BEGIN) | mat=1 | type=1 | real=1 | csys=0 | secn=1

Change jobname

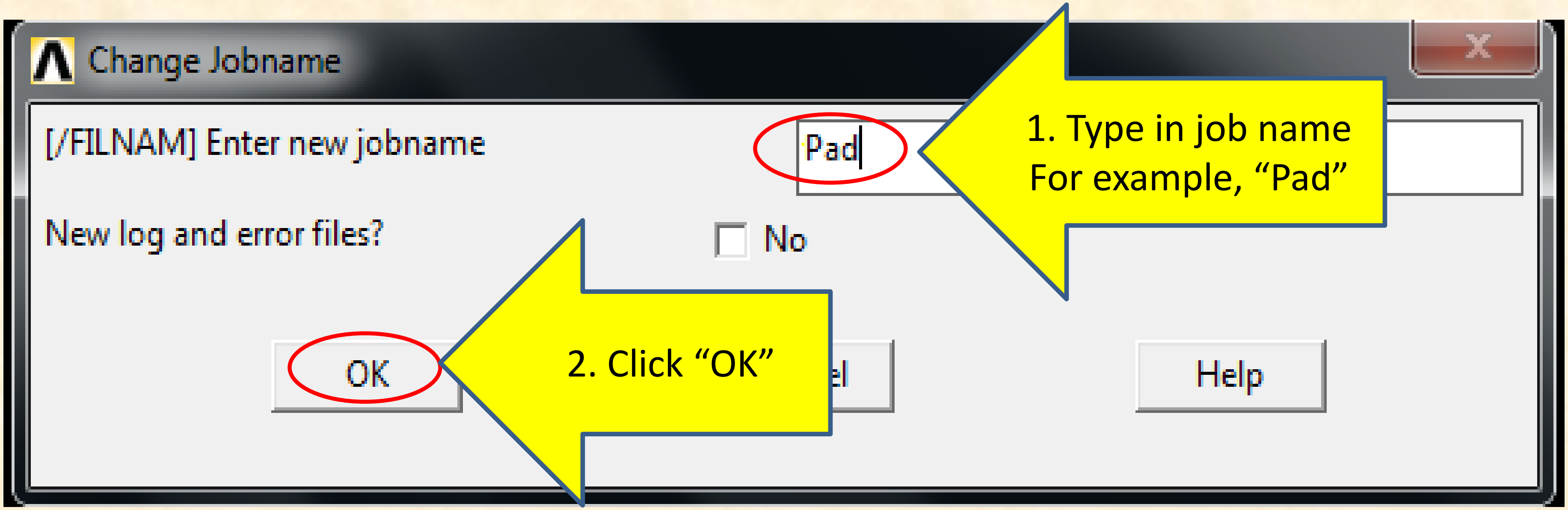

Change Jobname

[/FILNAM] Enter new jobname

Pad

New log and error files?

1. Type in job name For example, “Pad”

2. Click “OK”

Main interface

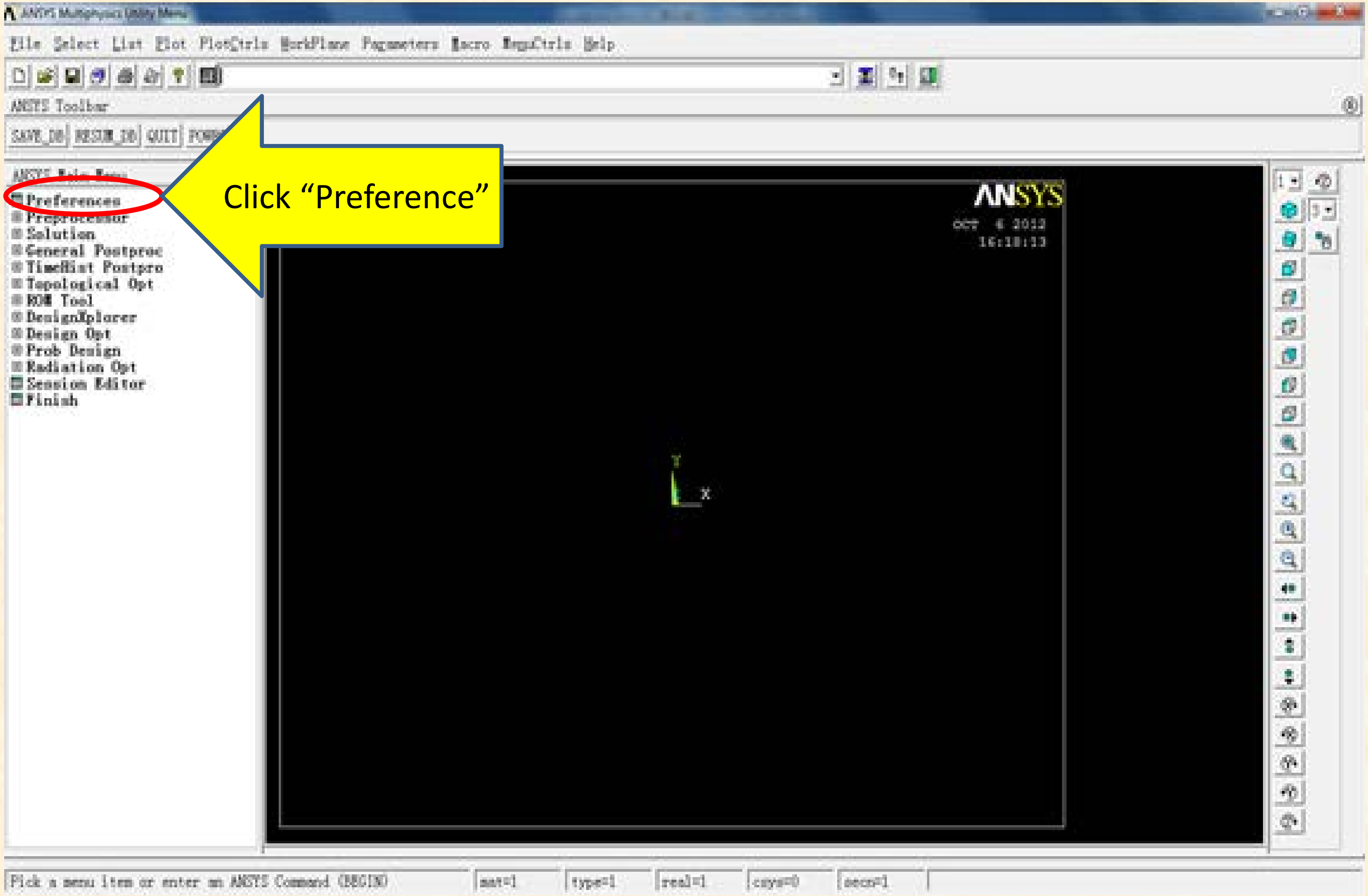
ANSYS Multiphysics Utility Menu
File Select List Plot PlotCtrls WorkPlane Parameters Macro MenuCtrls Help
ANSYS Toolbar
SAVE_DB RESUM_DB QUIT POWR
ANSYS Main Menu
Preferences
Preprocessor
Solution
General Postproc
TimeHist Postpro
Topological Opt
ROM Tool
DesignXplorer
Design Opt
Prob Design
Radiation Opt
Session Editor
Finish
ANSYS
OCT 6 2012
16:18:13
Y
X
Pick a menu item or enter an ANSYS Command (BEGIN)
mat=1
type=1
real=1
csys=0
secn=1

Click “Preference”

Preference for GUI Filtering

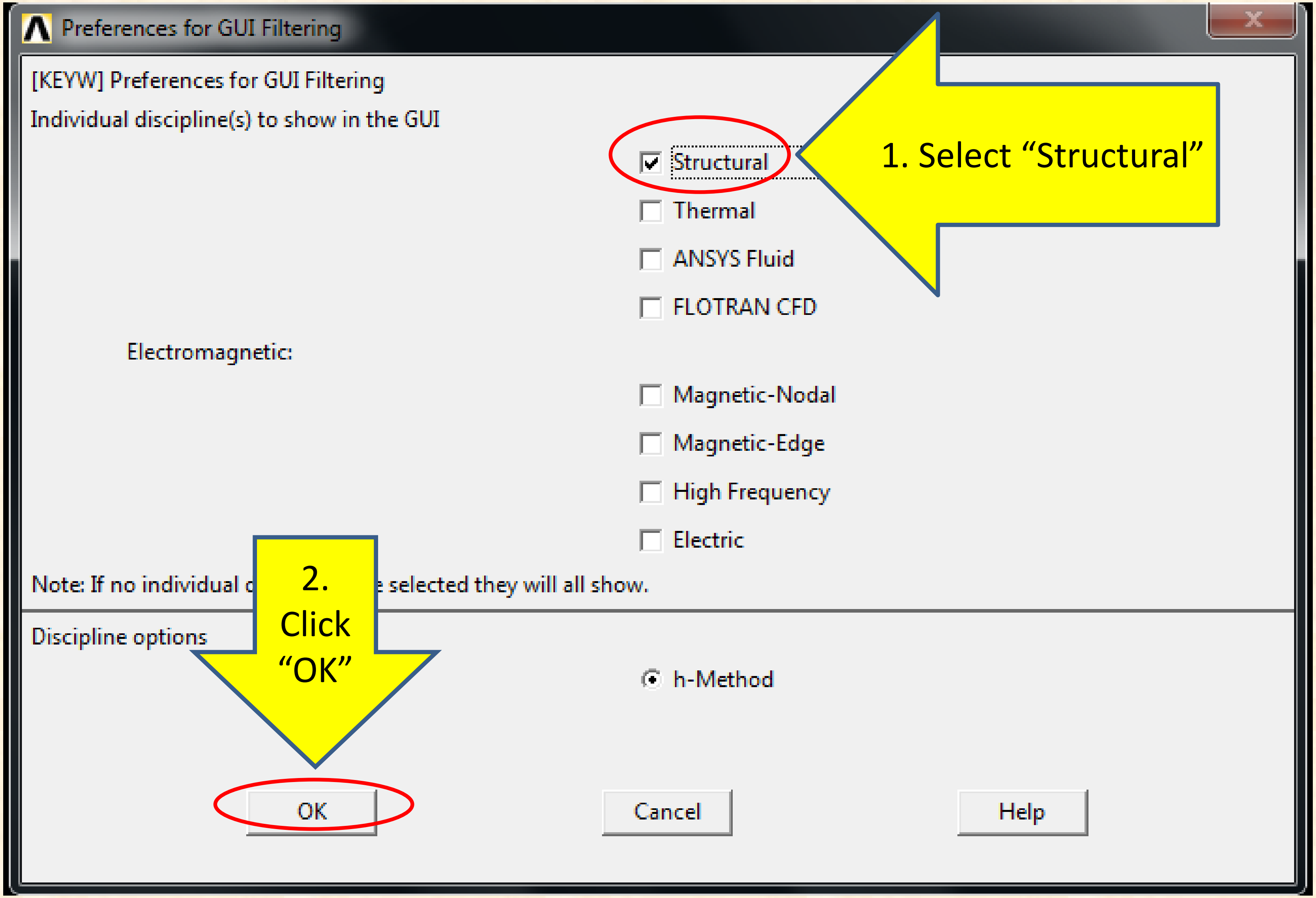

Preferences for GUI Filtering

[KEYW] Preferences for GUI Filtering

Individual discipline(s) to show in the GUI

☑ Structural

☐ Thermal

☐ ANSYS Fluid

☐ FLOTRAN CFD

Electromagnetic:

☐ Magnetic-Nodal

☐ Magnetic-Edge

☐ High Frequency

☐ Electric

Note: If no individual d… …e selected they will all show.

Discipline options

● h-Method

1. Select “Structural”

2. Click “OK”

Main interface

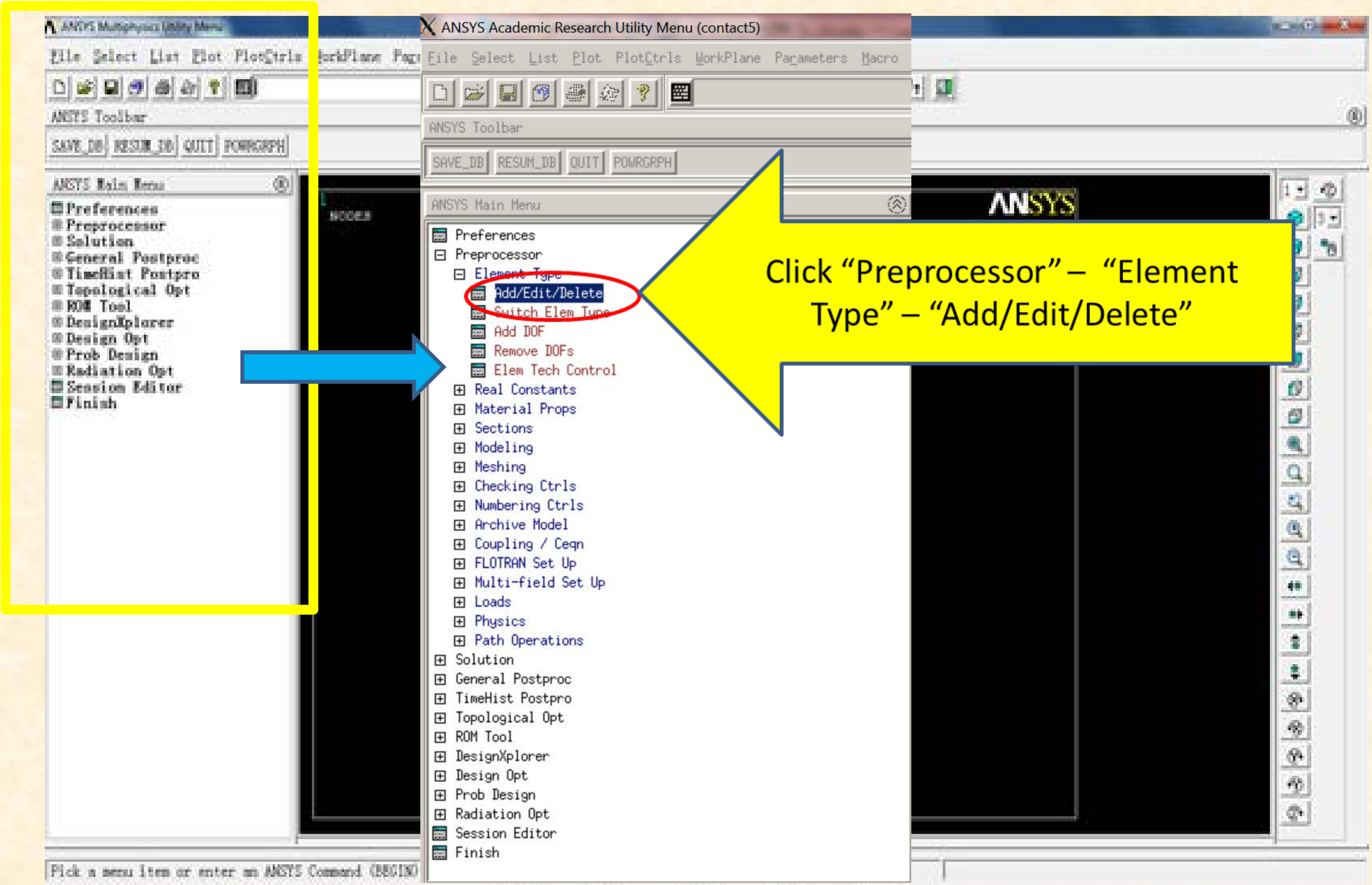
ANSYS Academic Research Utility Menu (contact5)
File Select List Plot PlotCtrls WorkPlane Parameters Macro
ANSYS Toolbar
SAVE_DB RESUM_DB QUIT POWRGRPH
ANSYS Main Menu
Preferences
Preprocessor
Element Type
Add/Edit/Delete
Switch Elem Type
Add DOF
Remove DOFs
Elem Tech Control
Real Constants
Material Props
Sections
Modeling
Meshing
Checking Ctrls
Numbering Ctrls
Archive Model
Coupling / Ceqn
FLOTRAN Set Up
Multi-field Set Up
Loads
Physics
Path Operations
Solution
General Postproc
TimeHist Postpro
Topological Opt
ROM Tool
DesignXplorer
Design Opt
Prob Design
Radiation Opt
Session Editor
Finish
ANSYS
Pick a menu item or enter an ANSYS Command (BEGIN)

Click “Preprocessor” – “Element Type” – “Add/Edit/Delete”

Element Types

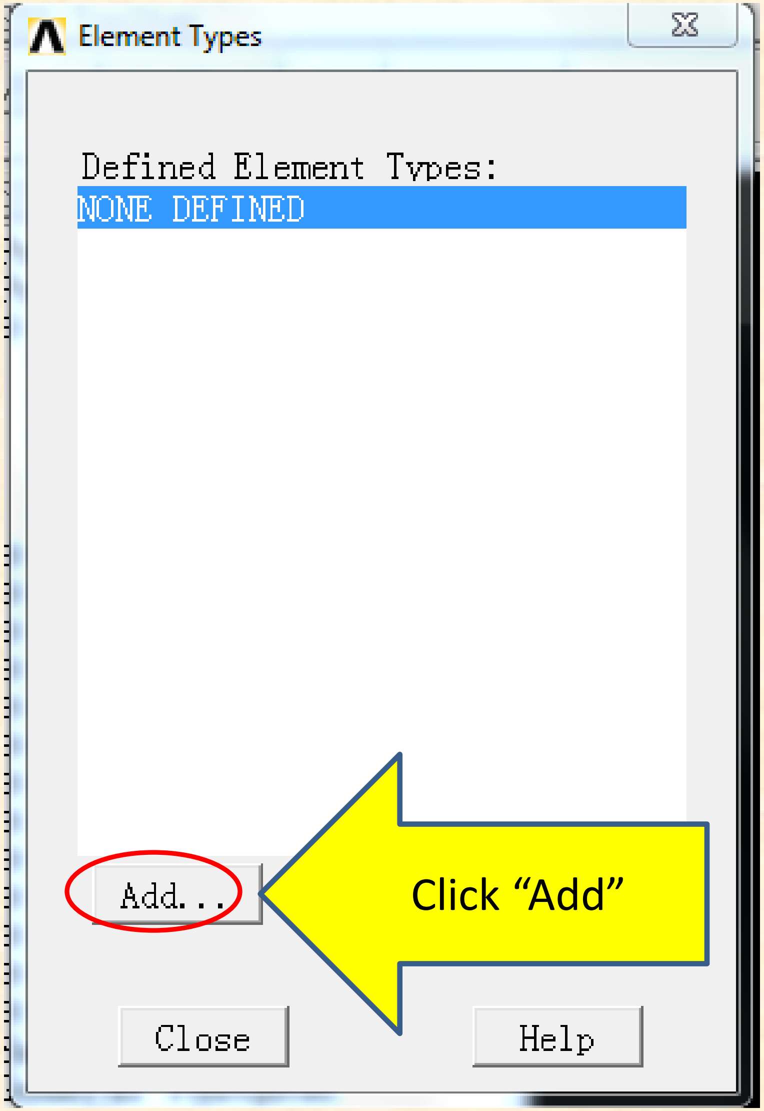
Element Types
Add...
Close
Help

Defined Element Types:
NONE DEFINED

Click “Add”

Element Types

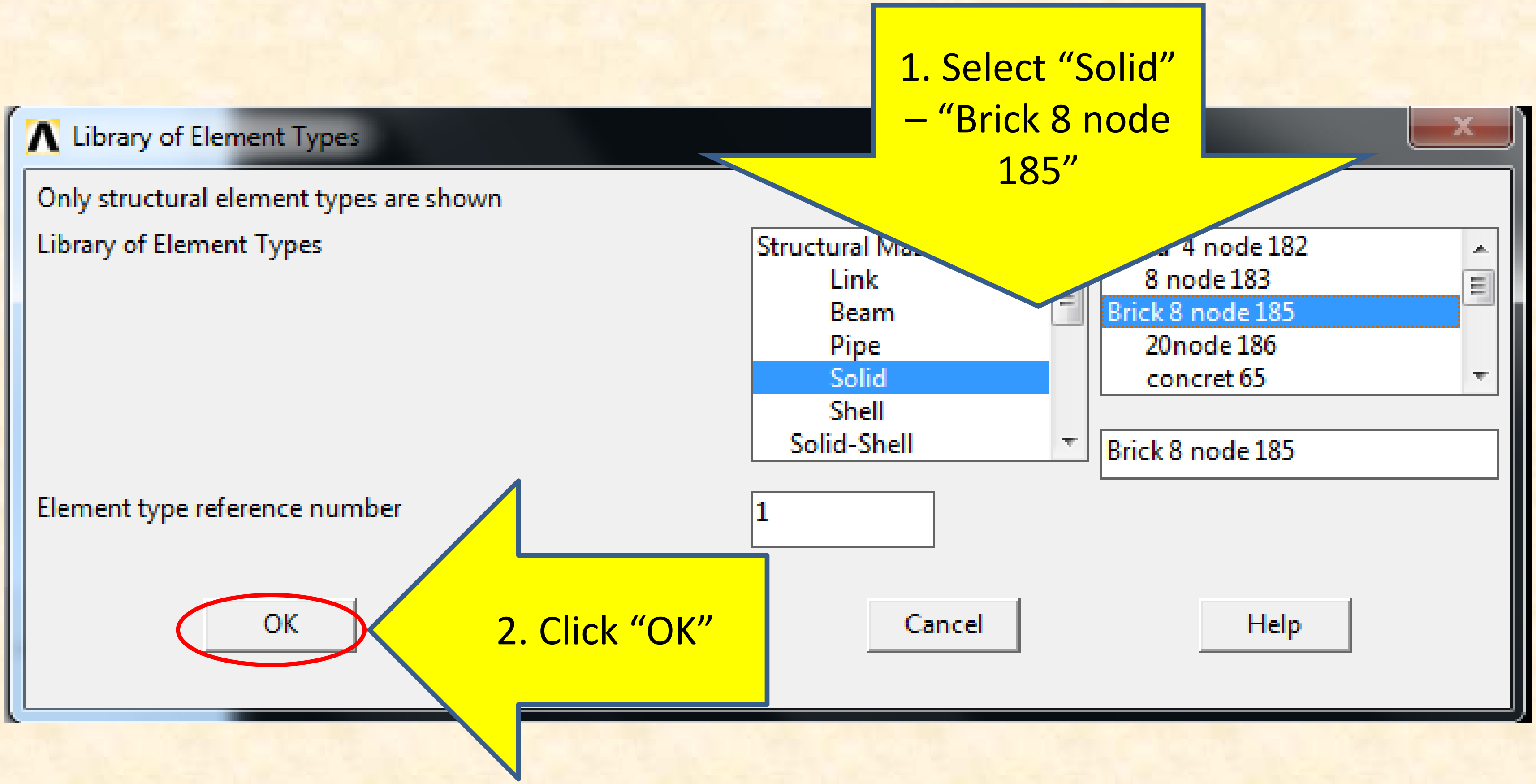

1. Select "Solid" – "Brick 8 node 185"

2. Click "OK"

Library of Element Types

Only structural element types are shown

Library of Element Types

Element type reference number: 1

Selected: Solid – Brick 8 node 185

Structural Ma
Link
Beam
Pipe
Solid
Shell
Solid-Shell
4 node 182
8 node 183
Brick 8 node 185
20node 186
concret 65
OK
Cancel
Help

Main interface

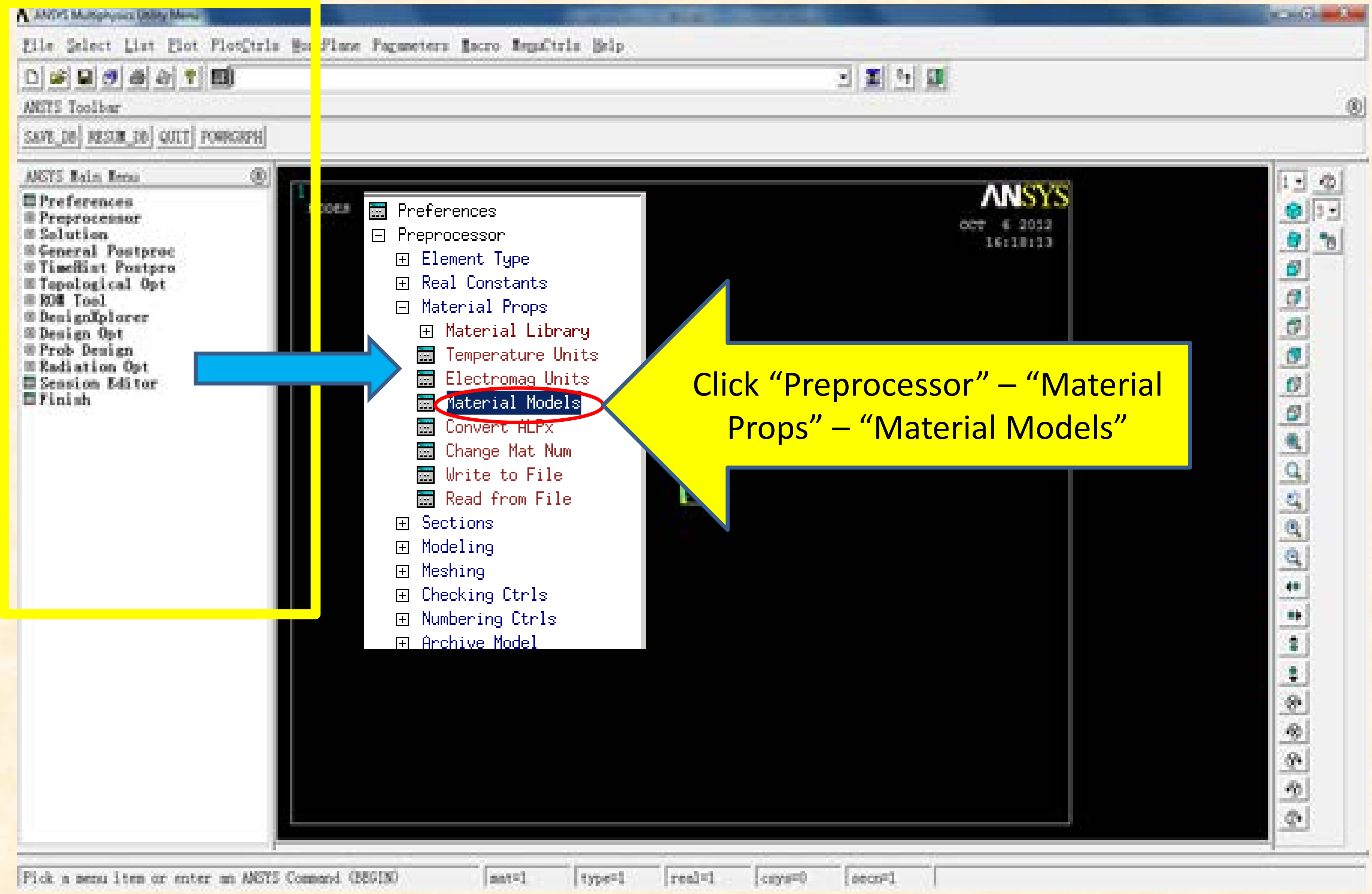
ANSYS Multiphysics Utility Menu
File Select List Plot PlotCtrls WorkPlane Parameters Macro MenuCtrls Help
ANSYS Toolbar
SAVE_DB RESUM_DB QUIT POWRGRPH
ANSYS Main Menu
Preferences
Preprocessor
Solution
General Postproc
TimeHist Postpro
Topological Opt
ROM Tool
DesignXplorer
Design Opt
Prob Design
Radiation Opt
Session Editor
Finish
Preferences
Preprocessor
Element Type
Real Constants
Material Props
Material Library
Temperature Units
Electromag Units
Material Models
Convert ALPx
Change Mat Num
Write to File
Read from File
Sections
Modeling
Meshing
Checking Ctrls
Numbering Ctrls
Archive Model
ANSYS
OCT 6 2012
16:18:13
Pick a menu item or enter an ANSYS Command (BEGIN)
mat=1
type=1
real=1
csys=0
secn=1

Click “Preprocessor” – “Material Props” – “Material Models”

Define Material Model Behavior

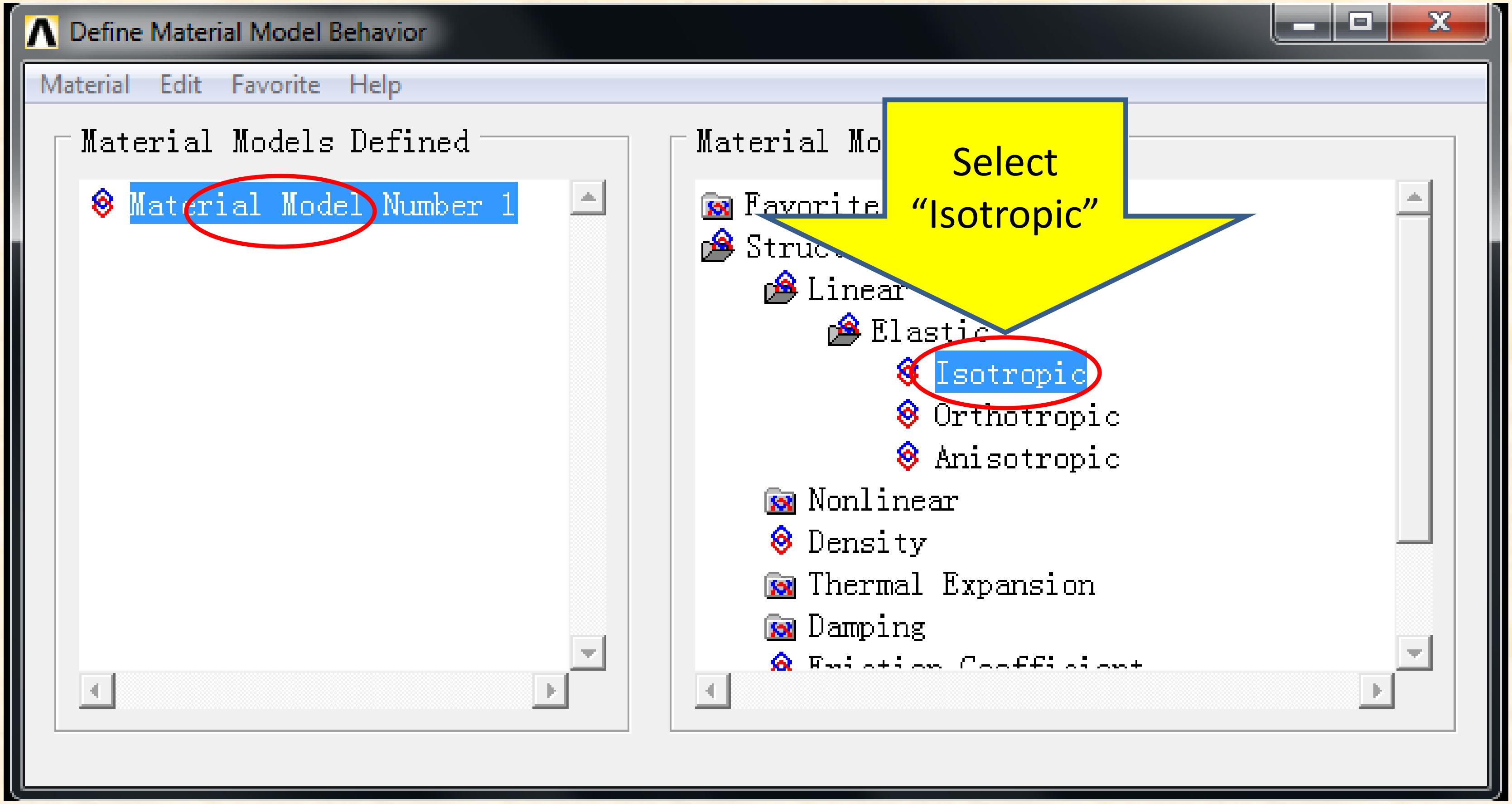
Define Material Model Behavior
Material Edit Favorite Help
Material Models Defined
Material Model Number 1
Material Mo
Favorite
Struc
Linear
Elastic
Isotropic
Orthotropic
Anisotropic
Nonlinear
Density
Thermal Expansion
Damping
Friction Coefficient
Select "Isotropic"

Linear Isotropic Properties

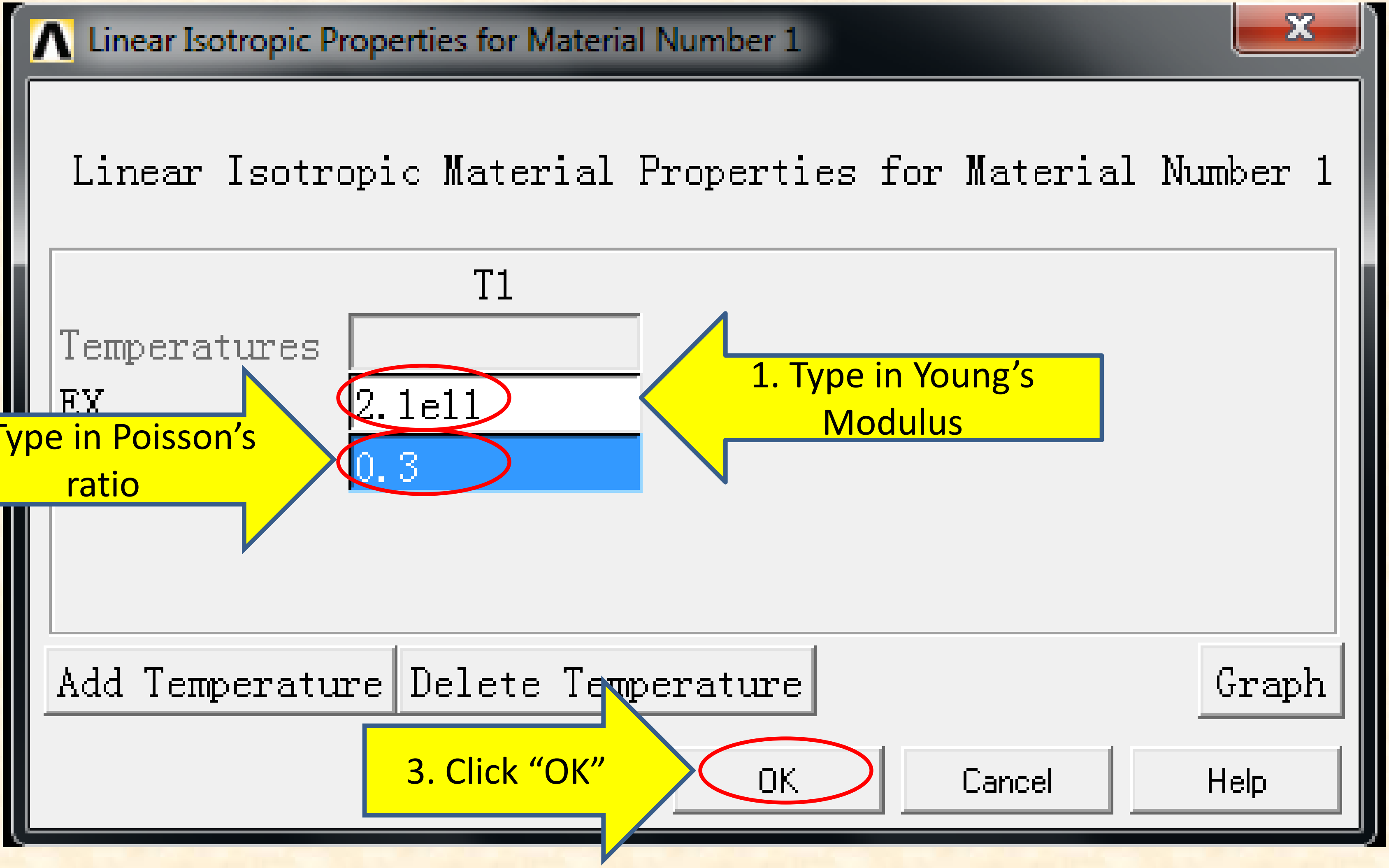

Linear Isotropic Properties for Material Number 1

Linear Isotropic Material Properties for Material Number 1

	T1
Temperatures	
EX	2.1e11
PRXY	0.3

Add Temperature
Delete Temperature
Graph
OK
Cancel
Help

1. Type in Young's Modulus

2. Type in Poisson's ratio

3. Click "OK"

Define Material Model Behavior

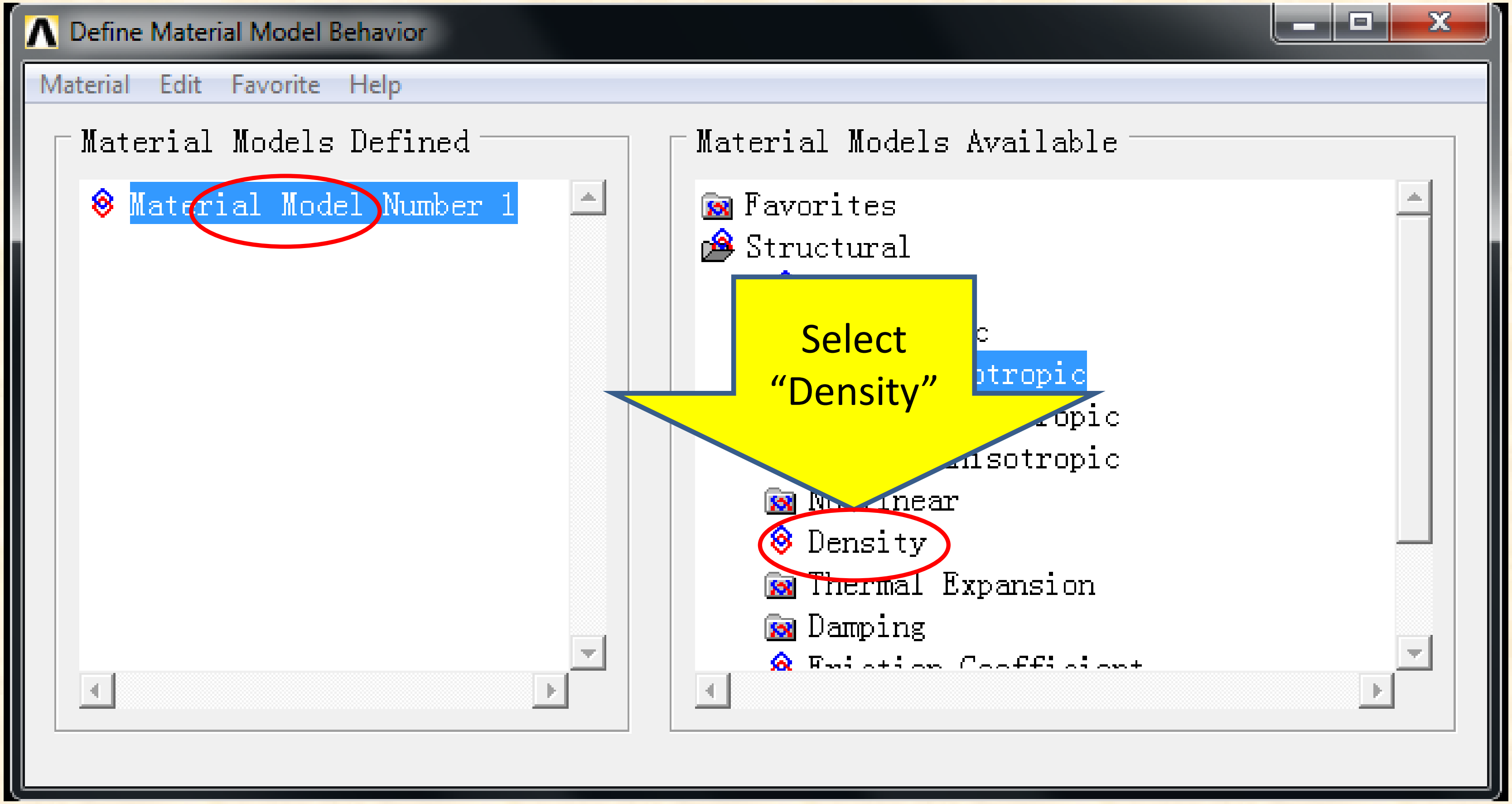
Define Material Model Behavior
Material
Edit
Favorite
Help
Material Models Defined
Material Model Number 1
Material Models Available
Favorites
Structural
Density
Thermal Expansion
Damping

Select "Density"

Density for Material Number 1

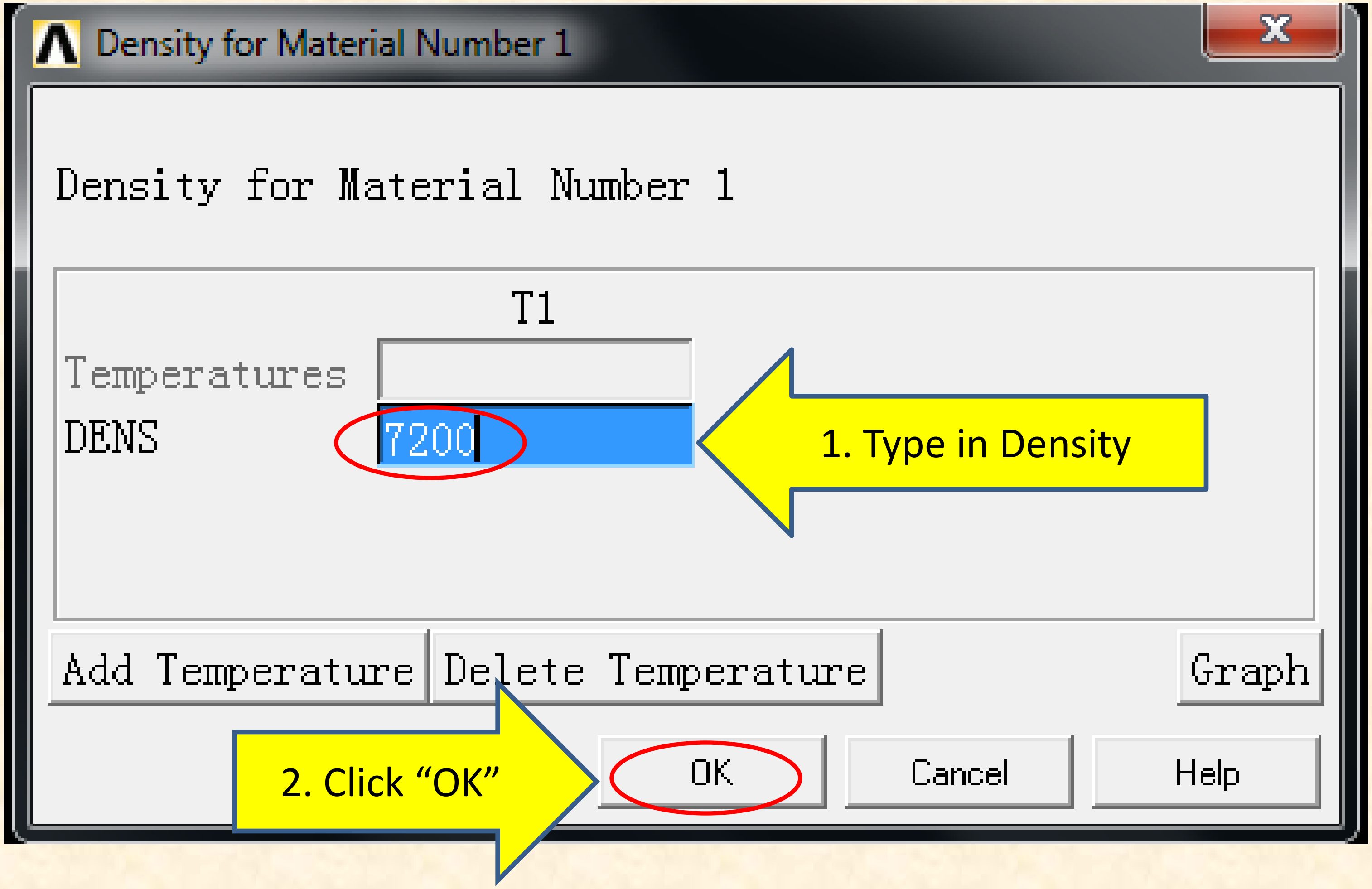

Density for Material Number 1

Density for Material Number 1

	T1
Temperatures	
DENS	7200

Add Temperature
Delete Temperature
Graph
OK
Cancel
Help

1. Type in Density

2. Click “OK”

Density for Material Number 1

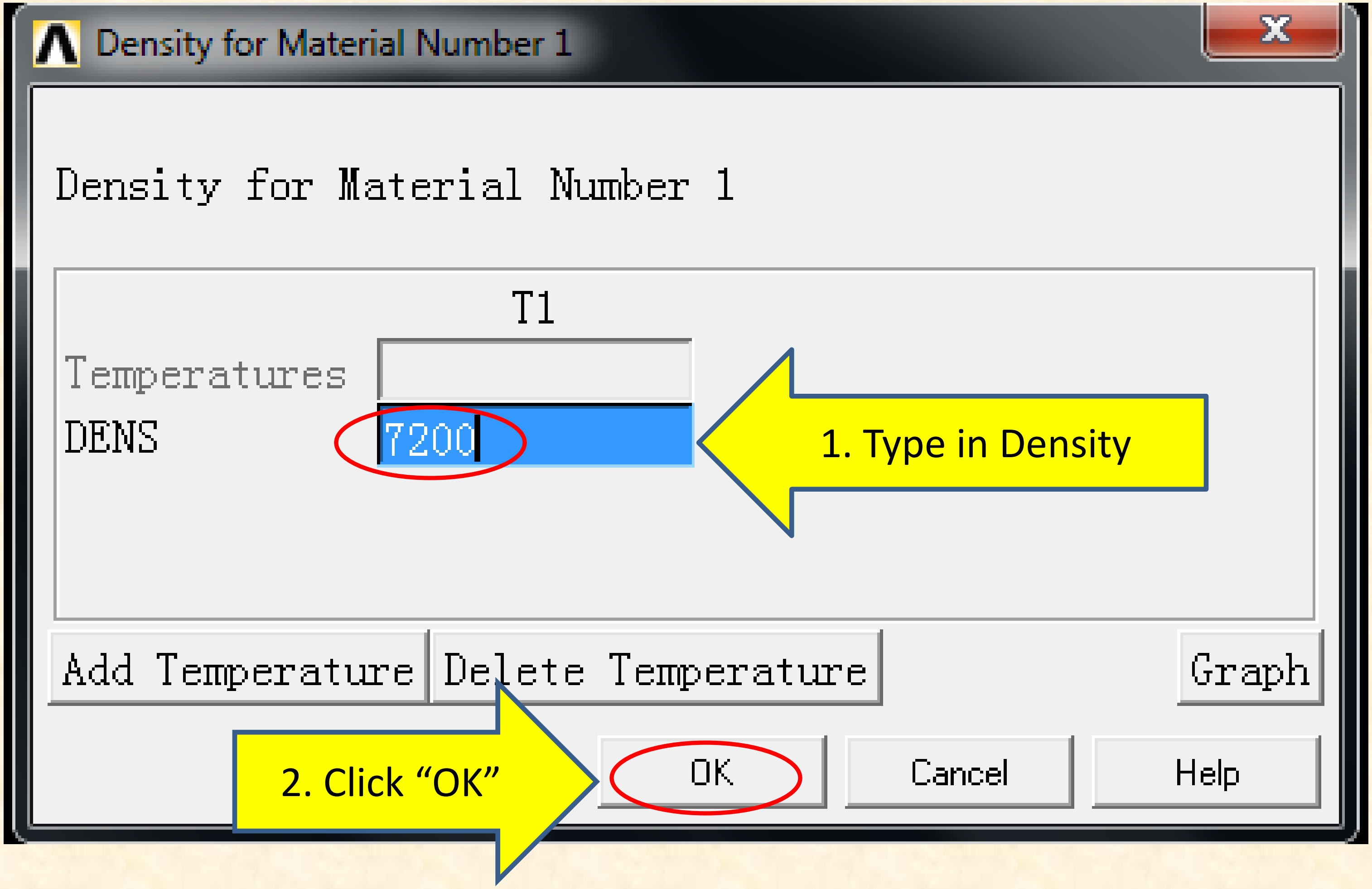

Density for Material Number 1

Density for Material Number 1

T1

Temperatures

DENS 7200

Add Temperature
Delete Temperature
Graph
OK
Cancel
Help

1. Type in Density

2. Click “OK”

Main interface

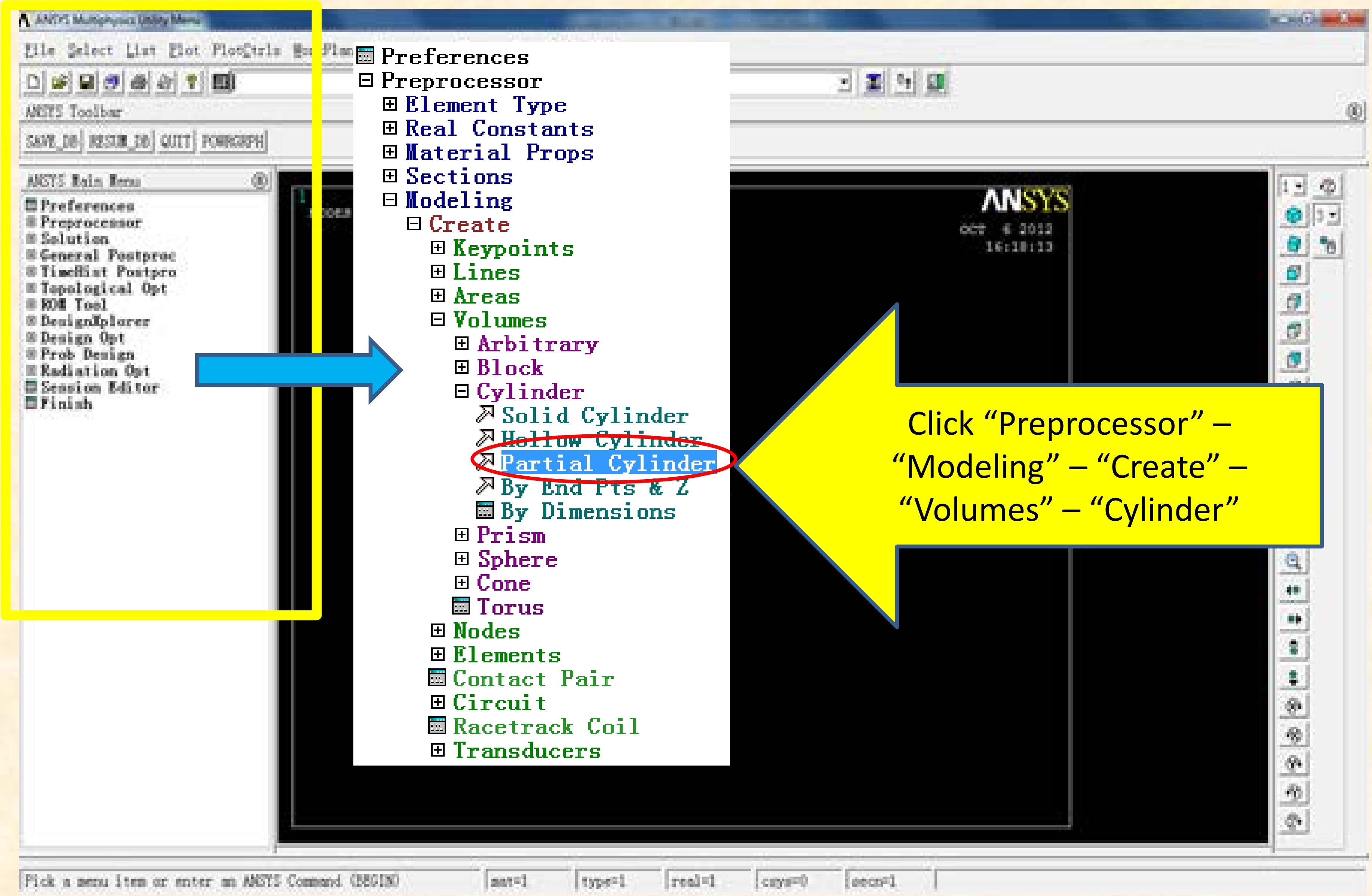
ANSYS Multiphysics Utility Menu
File Select List Plot PlotCtrls WorkPlane
ANSYS Toolbar
SAVE_DB RESUM_DB QUIT POWRGRPH
ANSYS Main Menu
Preferences
Preprocessor
Solution
General Postproc
TimeHist Postpro
Topological Opt
ROM Tool
DesignXplorer
Design Opt
Prob Design
Radiation Opt
Session Editor
Finish
Preferences
Preprocessor
Element Type
Real Constants
Material Props
Sections
Modeling
Create
Keypoints
Lines
Areas
Volumes
Arbitrary
Block
Cylinder
Solid Cylinder
Hollow Cylinder
Partial Cylinder
By End Pts & Z
By Dimensions
Prism
Sphere
Cone
Torus
Nodes
Elements
Contact Pair
Circuit
Racetrack Coil
Transducers
ANSYS
OCT 6 2012
16:18:13
Pick a menu item or enter an ANSYS Command (BEGIN)
mat=1
type=1
real=1
csys=0
secn=1

Click “Preprocessor” – “Modeling” – “Create” – “Volumes” – “Cylinder”

Partial Cylinder

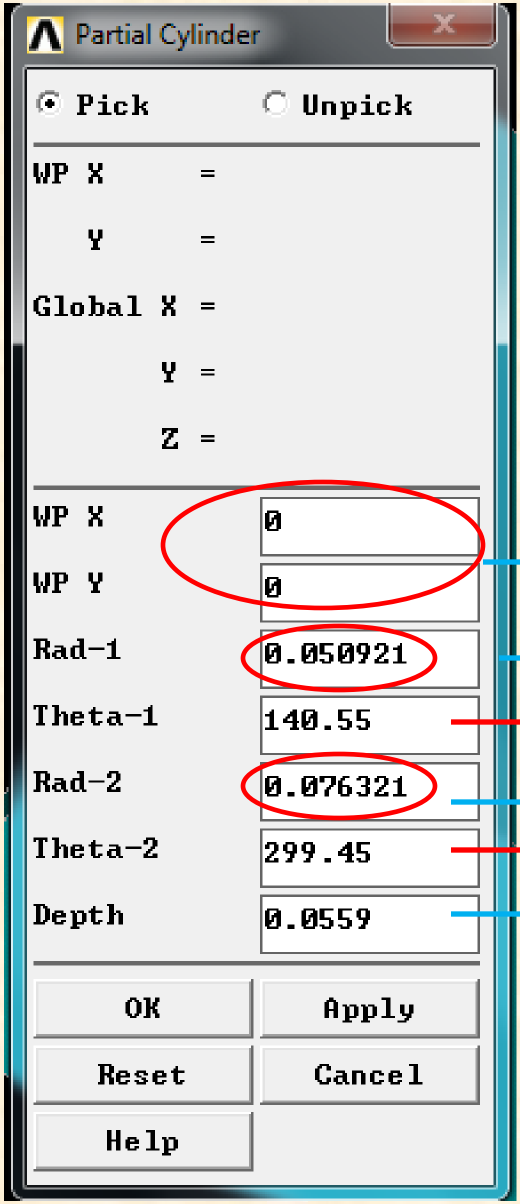
Partial Cylinder
OK
Apply
Reset
Cancel
Help

● Pick ○ Unpick

WP X =
Y =
Global X =
Y =
Z =

WP X: 0
WP Y: 0
Rad-1: 0.050921
Theta-1: 140.55
Rad-2: 0.076321
Theta-2: 299.45
Depth: 0.0559

Type in the center coordinate of the bearing

Type in the leading edge angle and trailing edge angle of the pad

Type in inner and outer radius of the pad

Type in the axial length of the pad

The example pad model

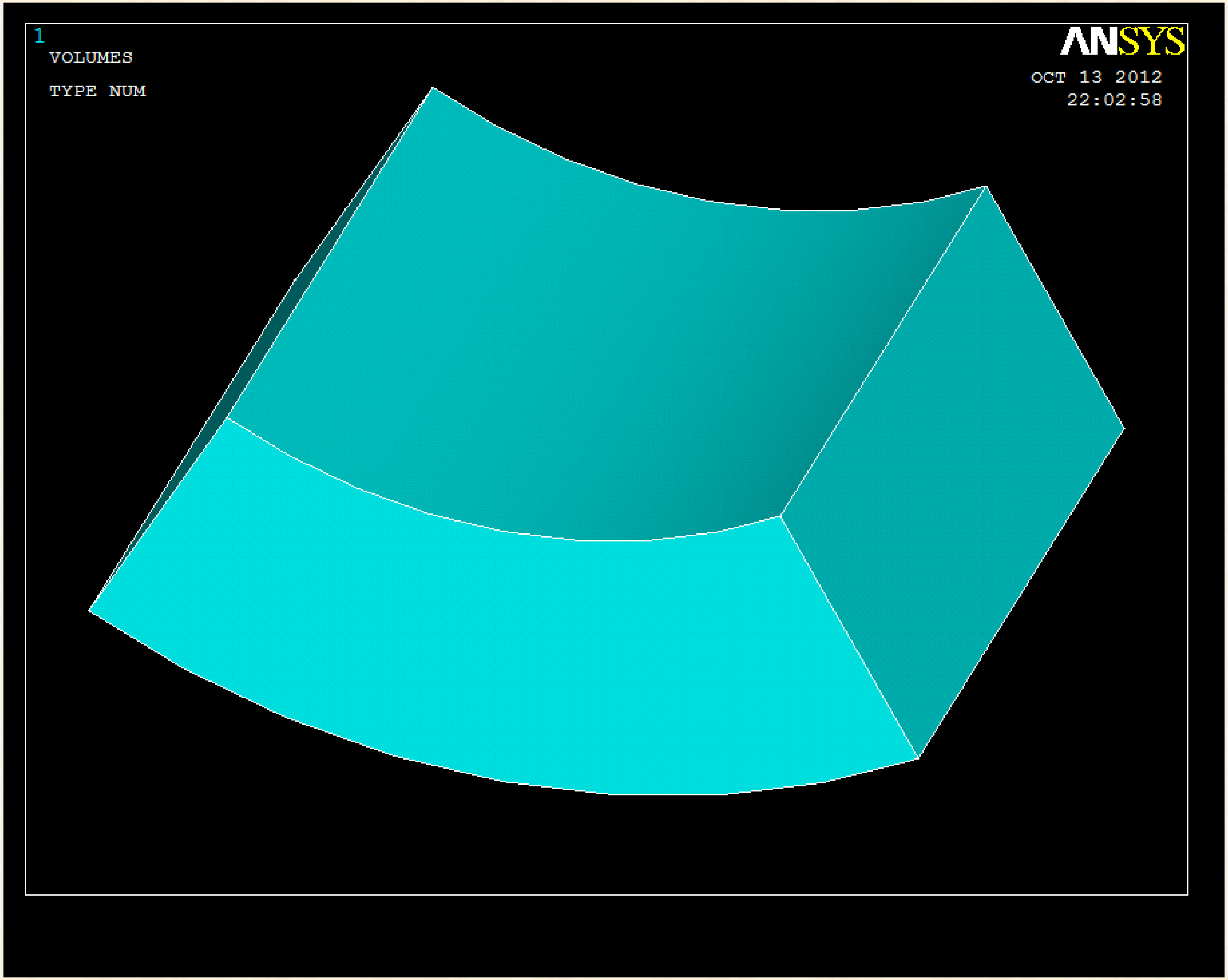
1
VOLUMES
TYPE NUM
ANSYS
OCT 13 2012
22:02:58

Main interface

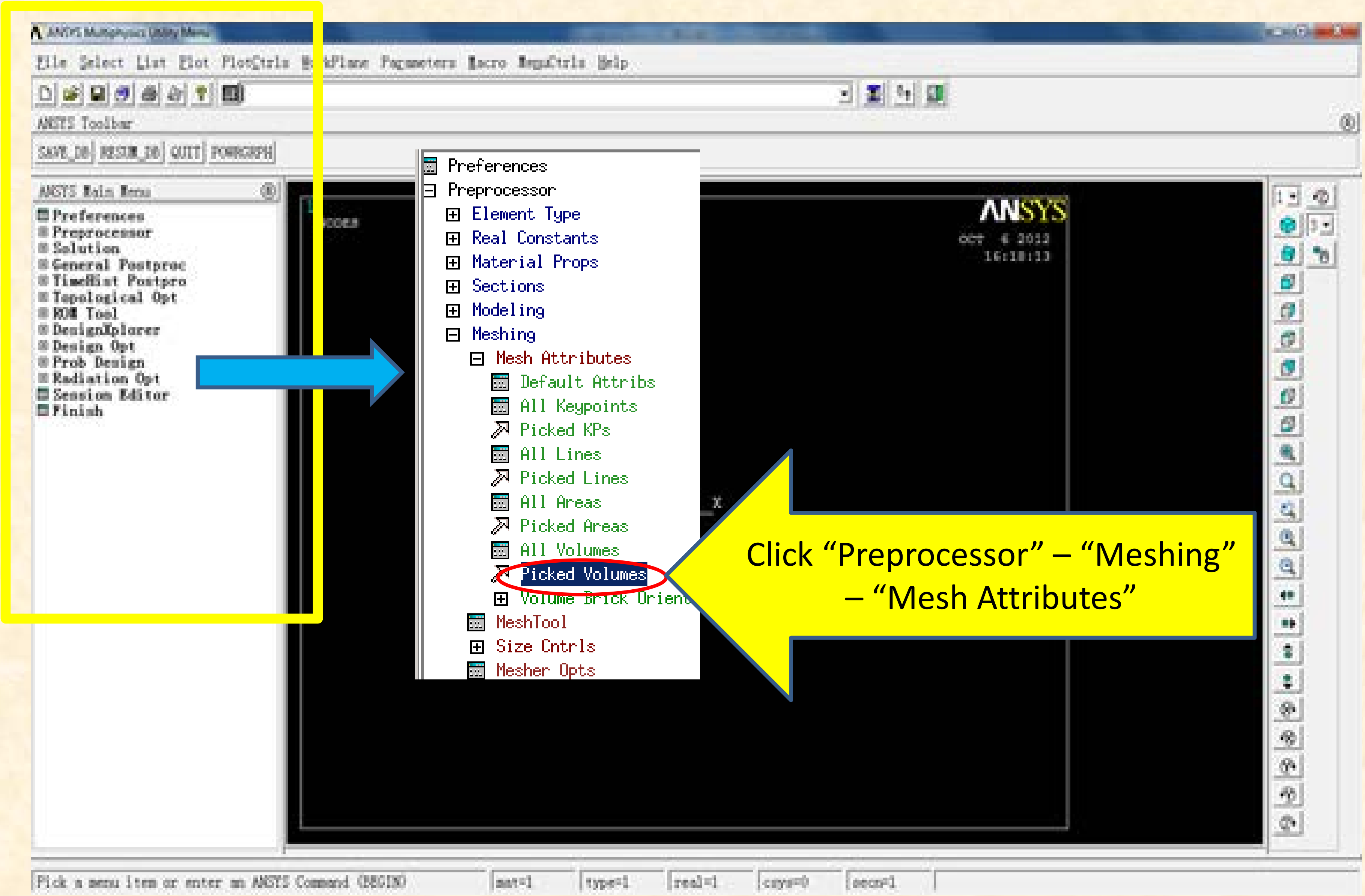
ANSYS Multiphysics Utility Menu
File Select List Plot PlotCtrls WorkPlane Parameters Macro MenuCtrls Help
ANSYS Toolbar
SAVE_DB RESUM_DB QUIT POWRGRPH
ANSYS Main Menu
Preferences
Preprocessor
Solution
General Postproc
TimeHist Postpro
Topological Opt
ROM Tool
DesignXplorer
Design Opt
Prob Design
Radiation Opt
Session Editor
Finish
NODES
ANSYS
OCT 6 2012
16:18:13
Preferences
Preprocessor
Element Type
Real Constants
Material Props
Sections
Modeling
Meshing
Mesh Attributes
Default Attribs
All Keypoints
Picked KPs
All Lines
Picked Lines
All Areas
Picked Areas
All Volumes
Picked Volumes
Volume Brick Orient
MeshTool
Size Cntrls
Mesher Opts
Pick a menu item or enter an ANSYS Command (BEGIN)
mat=1
type=1
real=1
csys=0
secn=1

Click "Preprocessor" – "Meshing" – "Mesh Attributes"

Volume Attributes

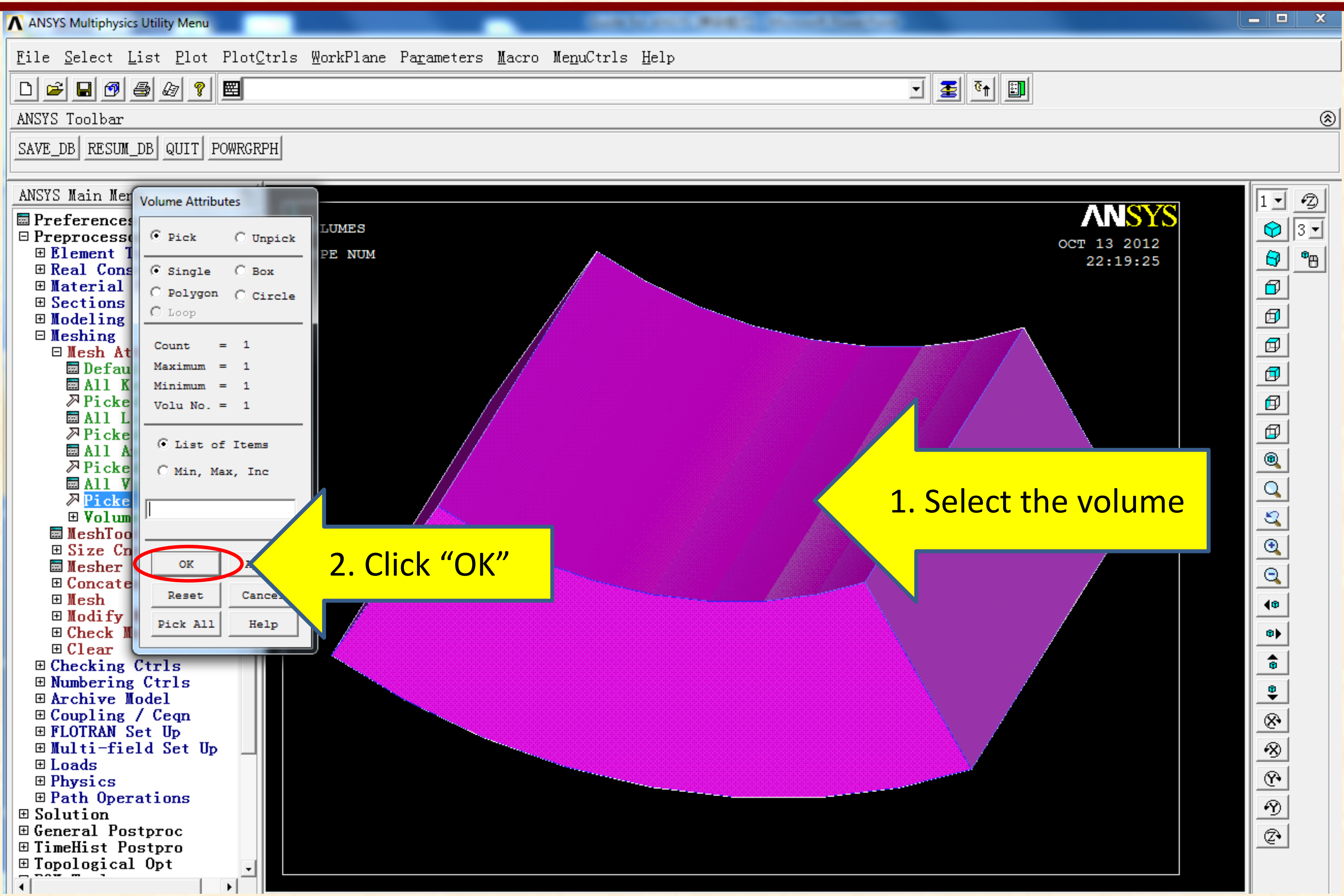
ANSYS Multiphysics Utility Menu
File Select List Plot PlotCtrls WorkPlane Parameters Macro MenuCtrls Help
ANSYS Toolbar
SAVE_DB RESUM_DB QUIT POWRGRPH
ANSYS Main Menu
Preferences
Preprocessor
Element Type
Real Constants
Material Props
Sections
Modeling
Meshing
Mesh Attributes
Default Attribs
All Keypoints
Picked KPs
All Lines
Picked Lines
All Areas
Picked Areas
All Volumes
Picked Volumes
Volume Sweep
MeshTool
Size Cntrls
Mesher Opts
Concatenate
Mesh
Modify Mesh
Check Mesh
Clear
Checking Ctrls
Numbering Ctrls
Archive Model
Coupling / Ceqn
FLOTRAN Set Up
Multi-field Set Up
Loads
Physics
Path Operations
Solution
General Postproc
TimeHist Postpro
Topological Opt
OK
Reset
Cancel
Pick All
Help
LUMES
PE NUM
ANSYS
OCT 13 2012
22:19:25

Volume Attributes

● Pick ○ Unpick

● Single ○ Box

○ Polygon ○ Circle

○ Loop

Count = 1

Maximum = 1

Minimum = 1

Volu No. = 1

● List of Items

○ Min, Max, Inc

1. Select the volume

2. Click “OK”

Volume Attributes

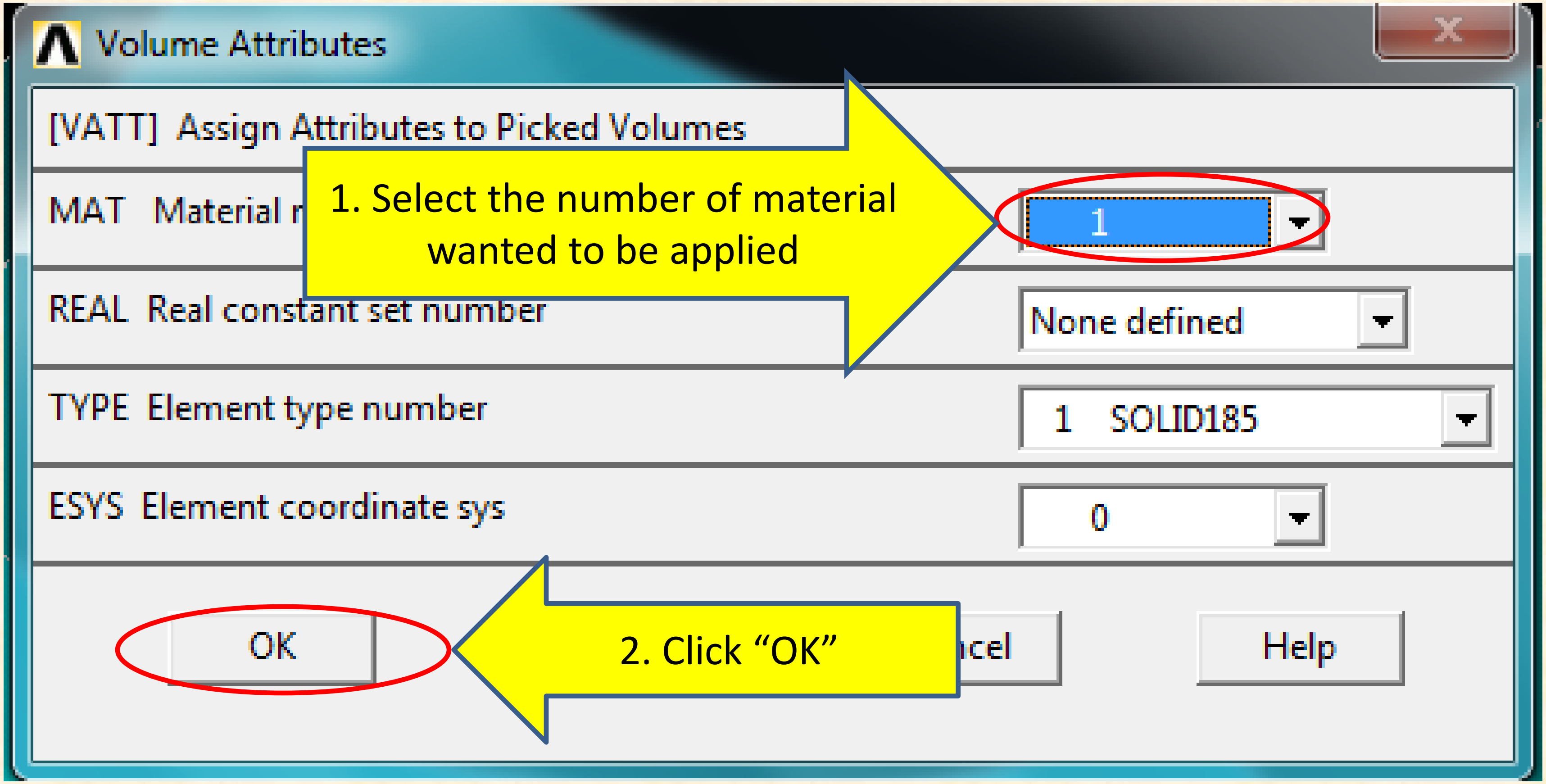

Volume Attributes

[VATT] Assign Attributes to Picked Volumes

MAT Material n 1

REAL Real constant set number None defined

TYPE Element type number 1 SOLID185

ESYS Element coordinate sys 0

1. Select the number of material wanted to be applied

2. Click “OK”

Main interface

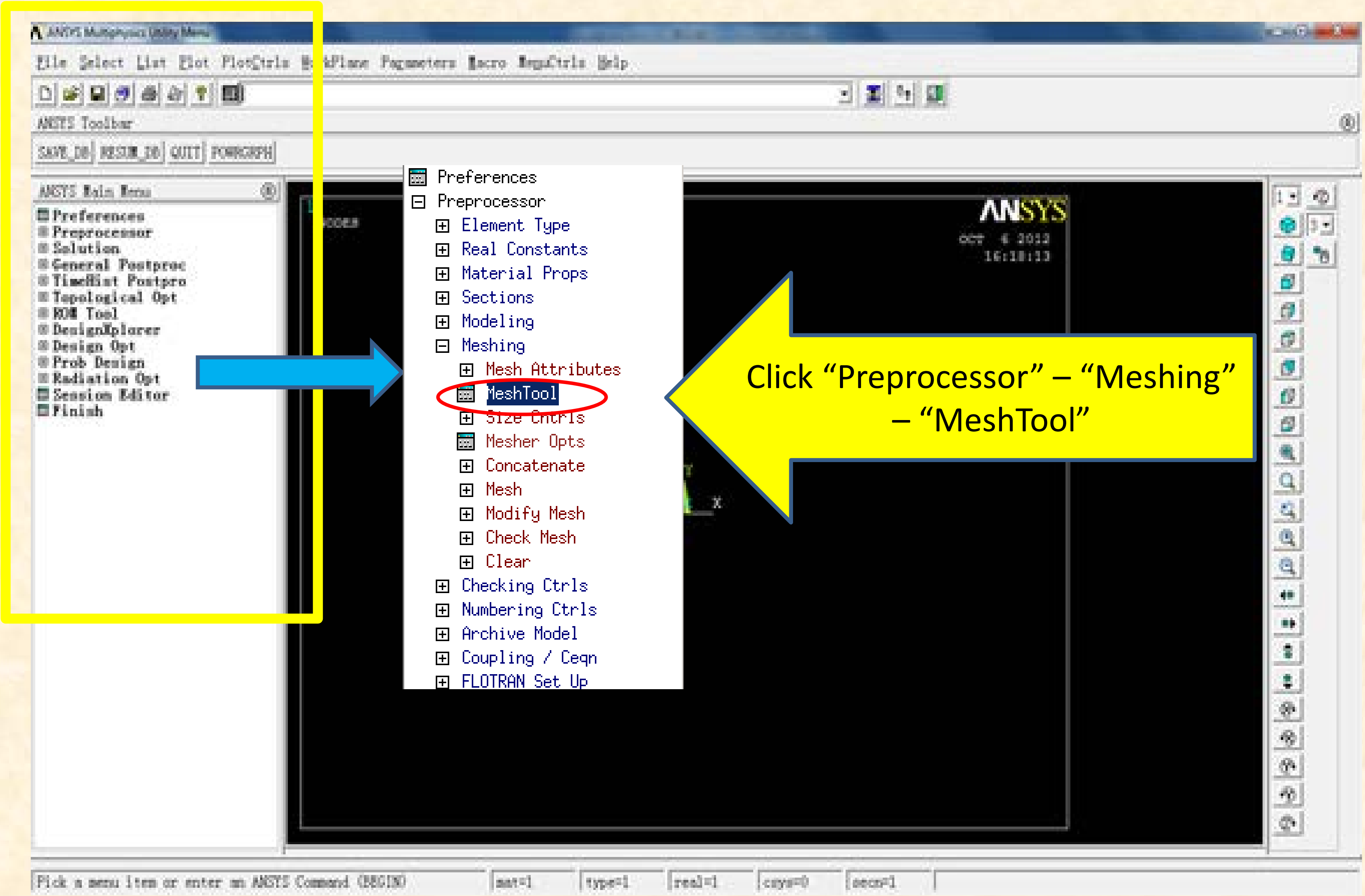
ANSYS Multiphysics Utility Menu
File Select List Plot PlotCtrls WorkPlane Parameters Macro MenuCtrls Help
ANSYS Toolbar
SAVE_DB RESUM_DB QUIT POWRGRPH
ANSYS Main Menu
Preferences
Preprocessor
Solution
General Postproc
TimeHist Postpro
Topological Opt
ROM Tool
DesignXplorer
Design Opt
Prob Design
Radiation Opt
Session Editor
Finish
Preferences
Preprocessor
Element Type
Real Constants
Material Props
Sections
Modeling
Meshing
Mesh Attributes
MeshTool
Size Cntrls
Mesher Opts
Concatenate
Mesh
Modify Mesh
Check Mesh
Clear
Checking Ctrls
Numbering Ctrls
Archive Model
Coupling / Ceqn
FLOTRAN Set Up
NODES
ANSYS
OCT 6 2012
16:18:13
Y
X
Pick a menu item or enter an ANSYS Command (BEGIN)
mat=1
type=1
real=1
csys=0
secn=1

Click “Preprocessor” – “Meshing” – “MeshTool”

MeshTool

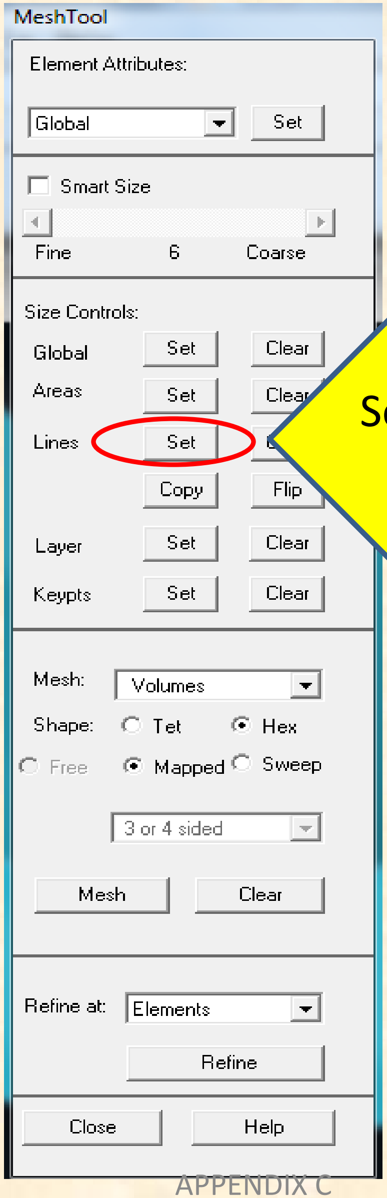
MeshTool

Element Attributes:

Global ▾ Set

☐ Smart Size

Fine 6 Coarse

Size Controls:

Global Set Clear
Areas Set Clear
Lines Set
Copy Flip
Layer Set Clear
Keypts Set Clear

Mesh: Volumes

Shape: ○ Tet ● Hex

○ Free ● Mapped ○ Sweep

3 or 4 sided

Mesh Clear

Refine at: Elements

Refine
Close Help

Set element size on lines

MeshTool

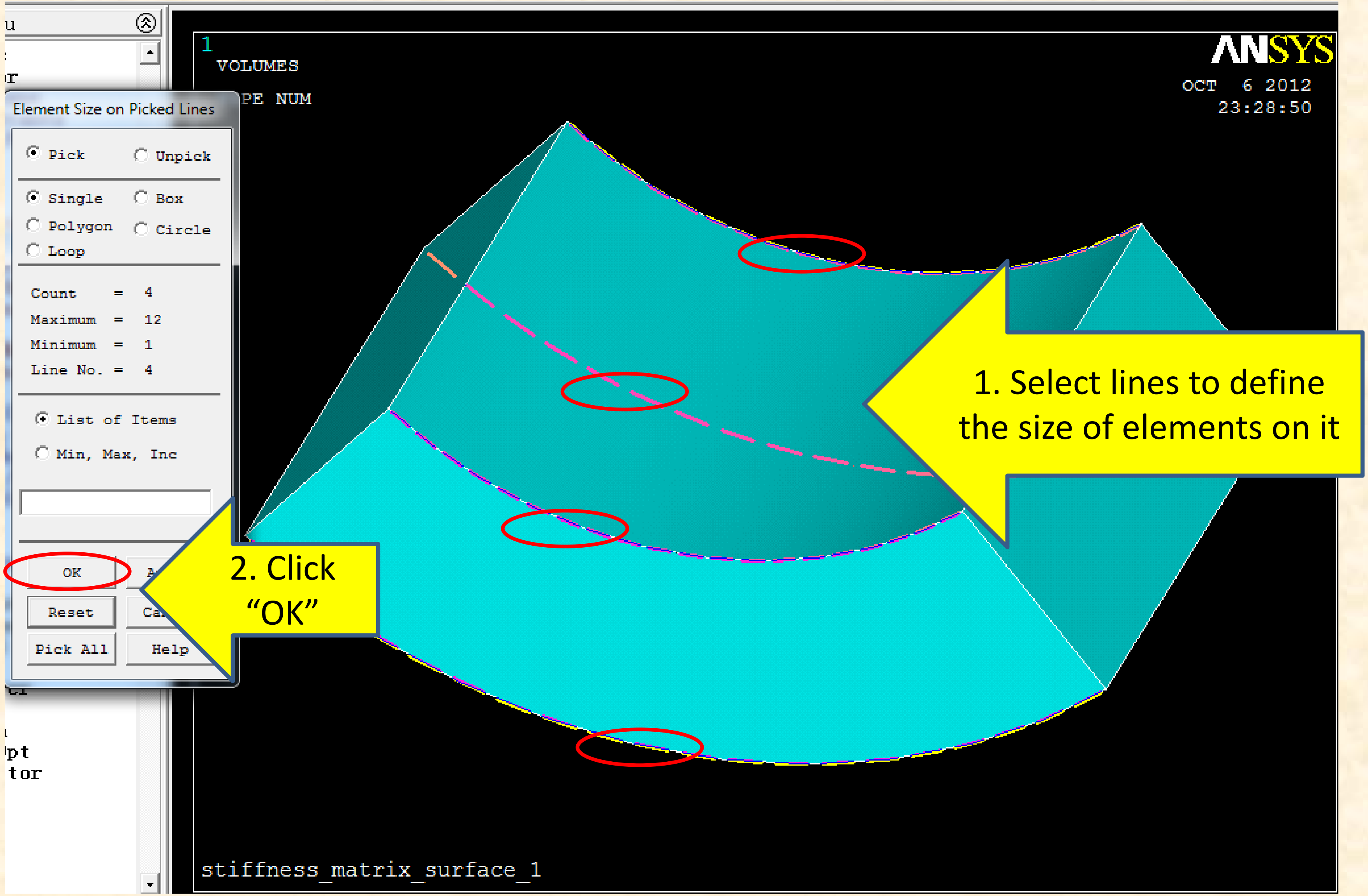

Element Size on Picked Lines

● Pick ○ Unpick

● Single ○ Box
○ Polygon ○ Circle
○ Loop

Count = 4
Maximum = 12
Minimum = 1
Line No. = 4

● List of Items
○ Min, Max, Inc

OK
Reset
Pick All
Help
1
VOLUMES
PE NUM
ANSYS
OCT 6 2012
23:28:50
stiffness_matrix_surface_1

1. Select lines to define the size of elements on it

2. Click "OK"

MeshTool

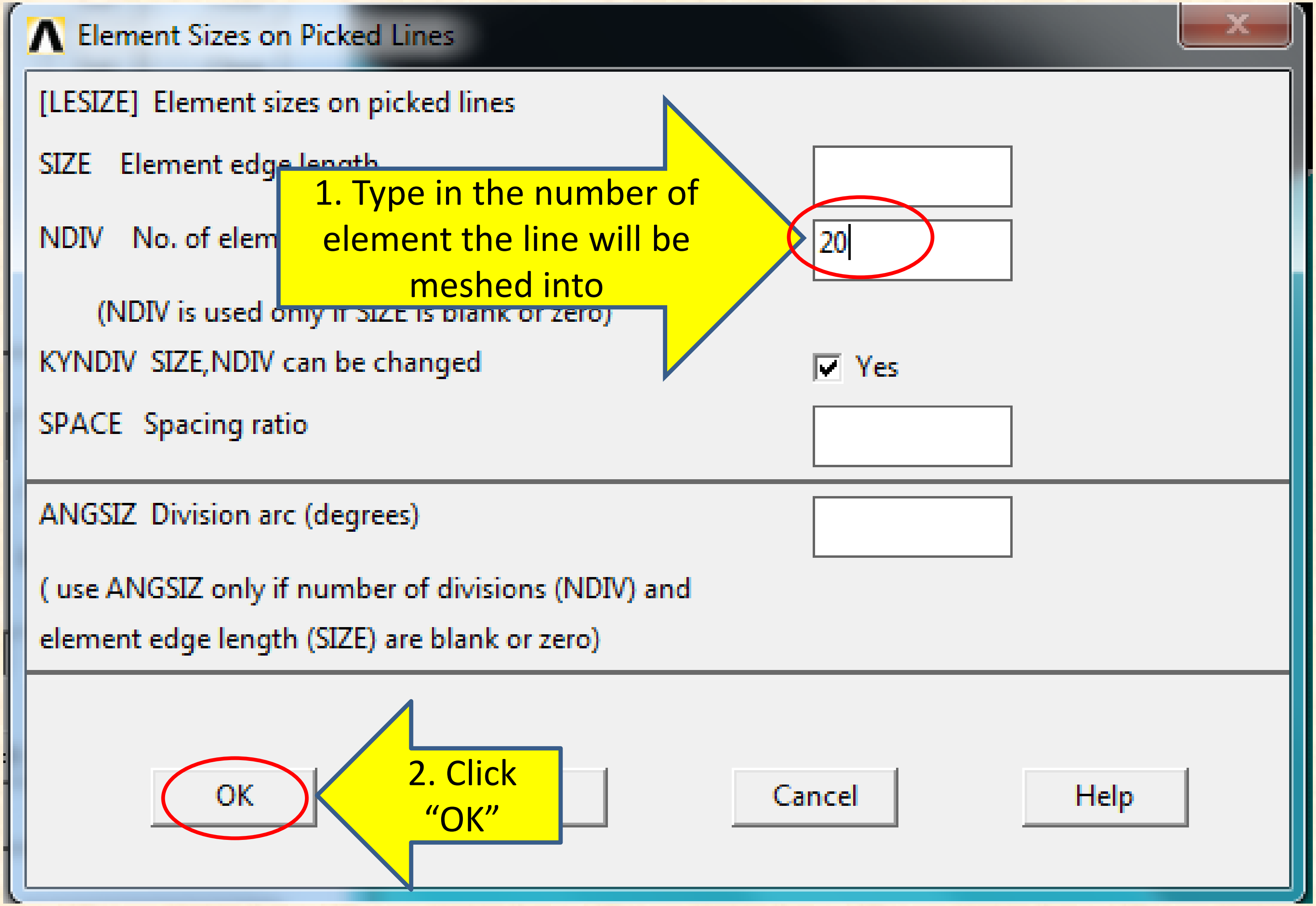

Element Sizes on Picked Lines

[LESIZE] Element sizes on picked lines

SIZE Element edge length

NDIV No. of elem 20

(NDIV is used only if SIZE is blank or zero)

KYNDIV SIZE,NDIV can be changed ☑ Yes

SPACE Spacing ratio

ANGSIZ Division arc (degrees)

(use ANGSIZ only if number of divisions (NDIV) and element edge length (SIZE) are blank or zero)

1. Type in the number of element the line will be meshed into

2. Click "OK"

Meshed model

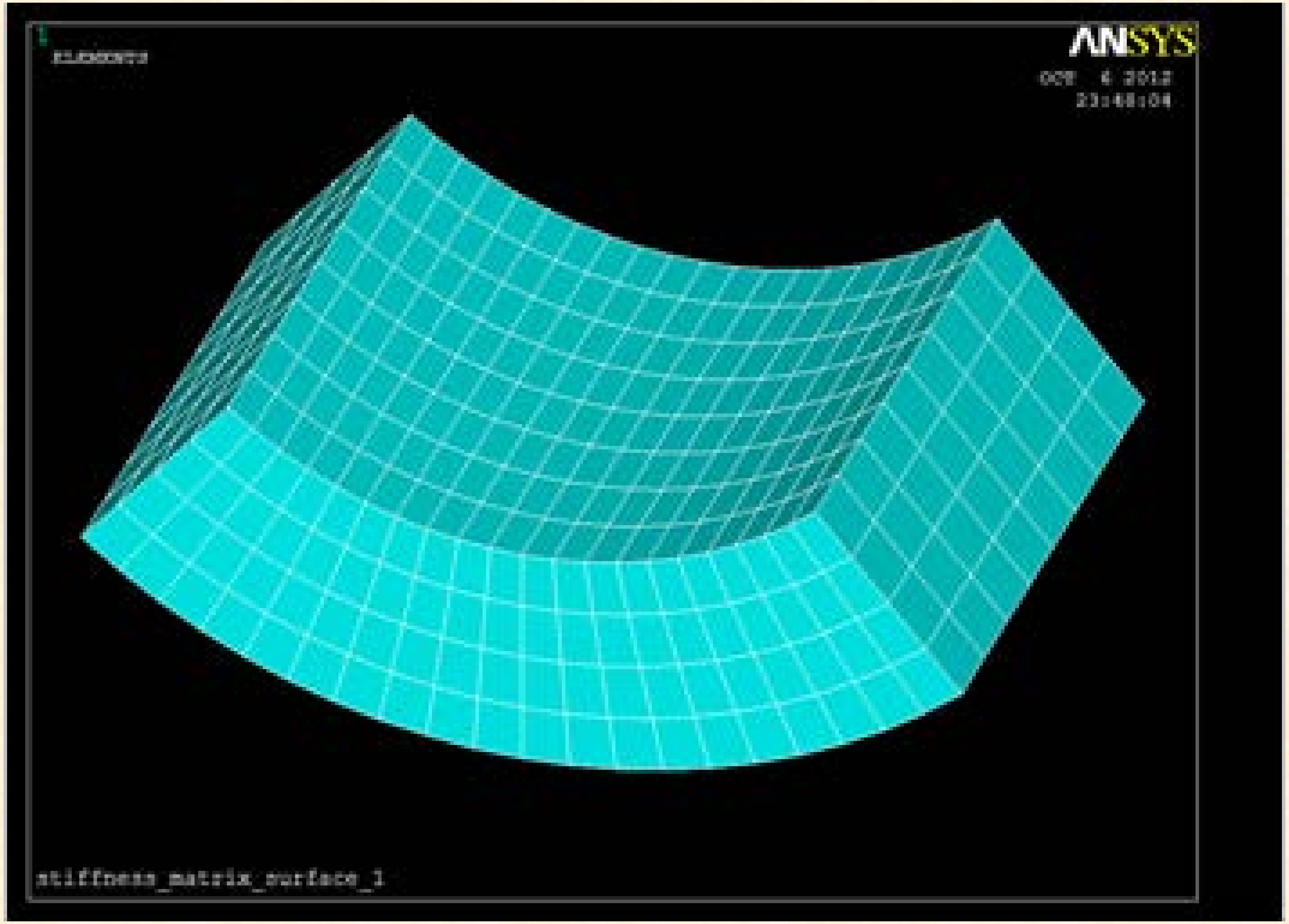
1
ELEMENTS
ANSYS
OCT 6 2012
23:48:04
stiffness_matrix_surface_1

Get stiffness matrix

ANSYS© has a function to reduce the stiffness matrix of a structural model.
As not all the nodal displacements are important to the analysis, ANSYS © offers a way to reduce the stiffness matrix into the size desired.

Main interface

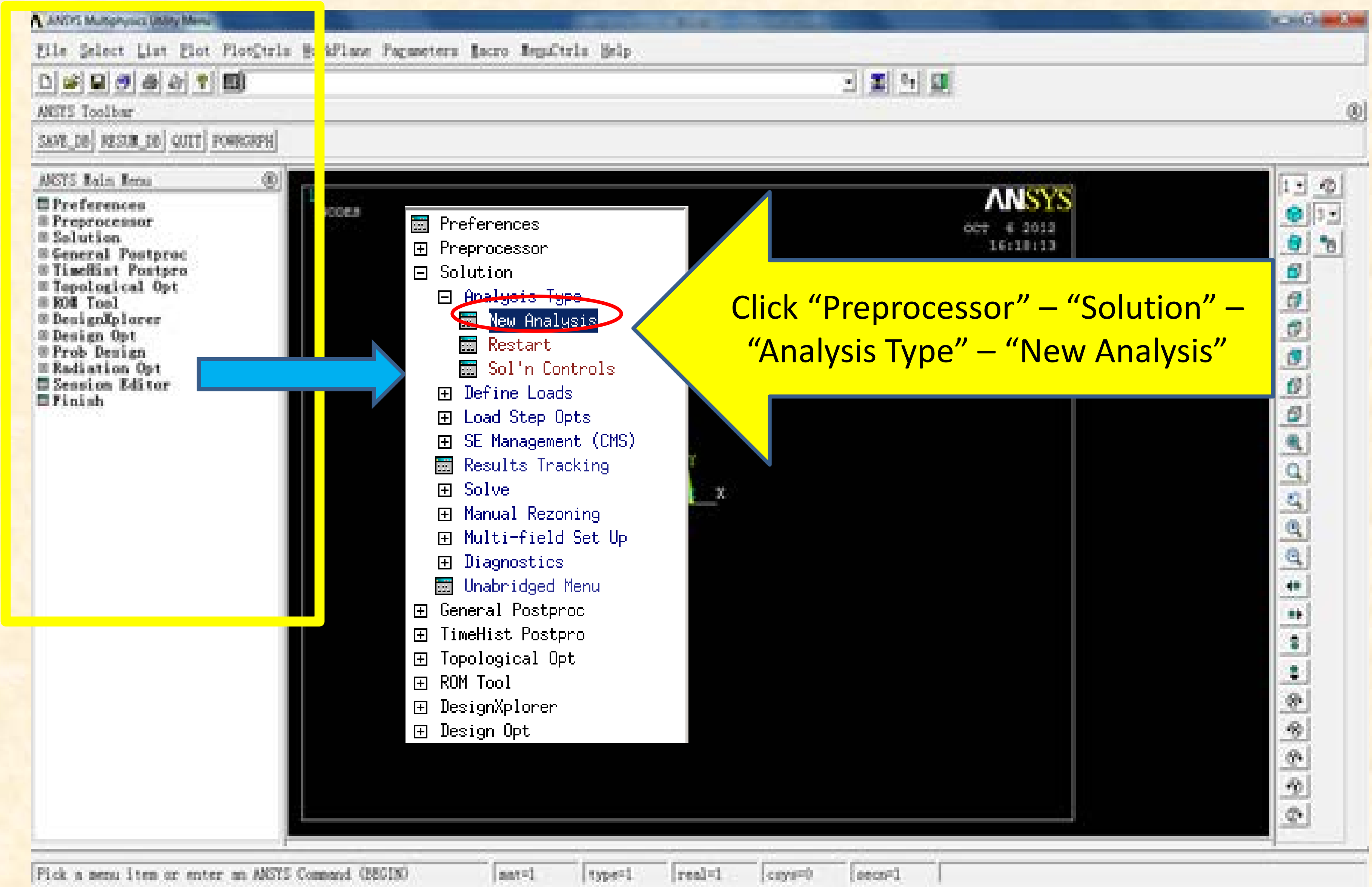
ANSYS Multiphysics Utility Menu
File Select List Plot PlotCtrls WorkPlane Parameters Macro MenuCtrls Help
ANSYS Toolbar
SAVE_DB RESUM_DB QUIT POWRGRPH
ANSYS Main Menu
Preferences
Preprocessor
Solution
General Postproc
TimeHist Postpro
Topological Opt
ROM Tool
DesignXplorer
Design Opt
Prob Design
Radiation Opt
Session Editor
Finish
Preferences
Preprocessor
Solution
Analysis Type
New Analysis
Restart
Sol'n Controls
Define Loads
Load Step Opts
SE Management (CMS)
Results Tracking
Solve
Manual Rezoning
Multi-field Set Up
Diagnostics
Unabridged Menu
General Postproc
TimeHist Postpro
Topological Opt
ROM Tool
DesignXplorer
Design Opt
ANSYS
OCT 6 2012
16:18:13
Pick a menu item or enter an ANSYS Command (BEGIN)
mat=1
type=1
real=1
csys=0
secn=1

Click “Preprocessor” – “Solution” – “Analysis Type” – “New Analysis”

New Analysis

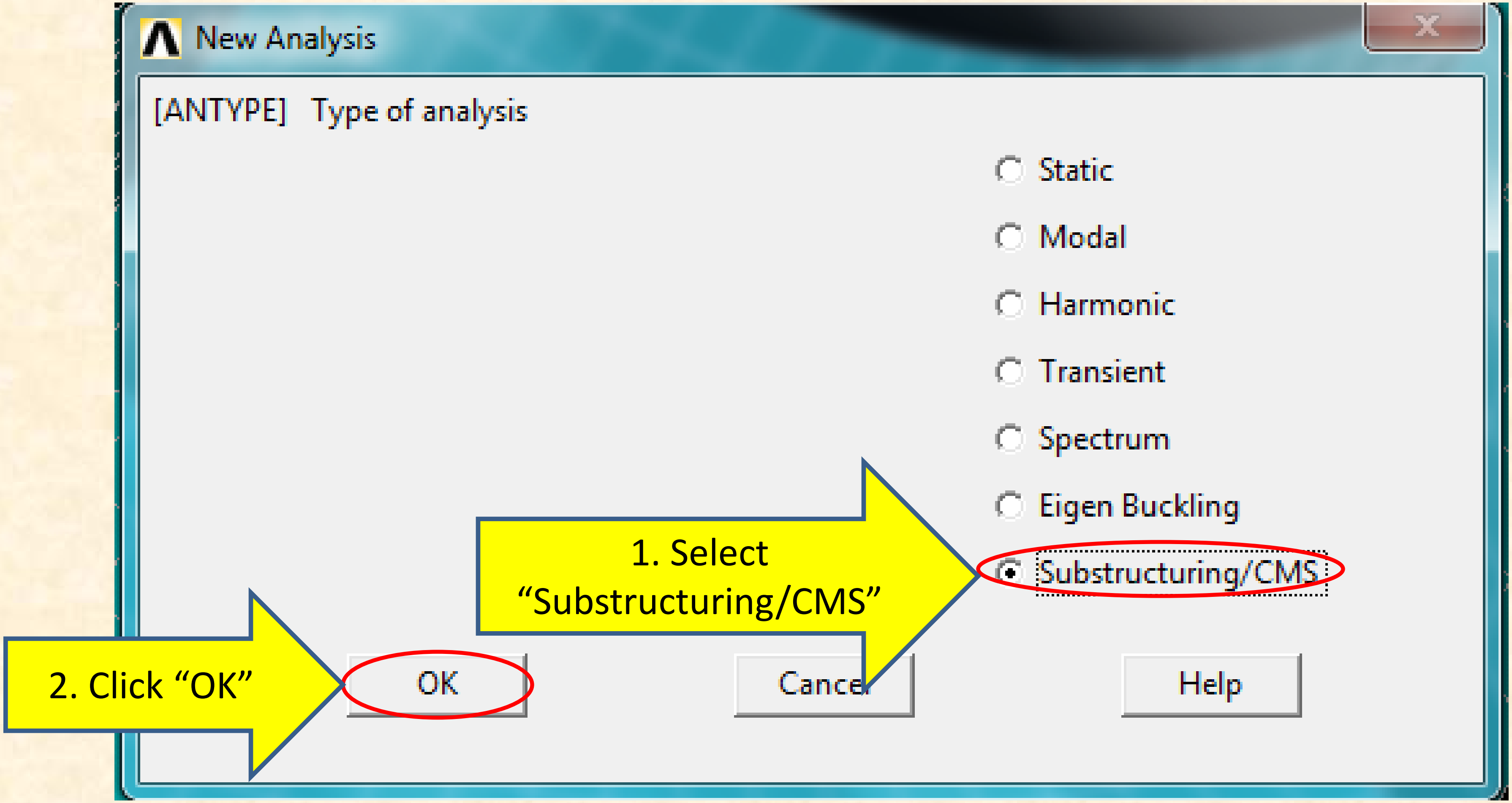

New Analysis

[ANTYPE] Type of analysis

○ Static
○ Modal
○ Harmonic
○ Transient
○ Spectrum
○ Eigen Buckling
● Substructuring/CMS

OK
Cancel
Help

1. Select "Substructuring/CMS"

2. Click "OK"

Main interface

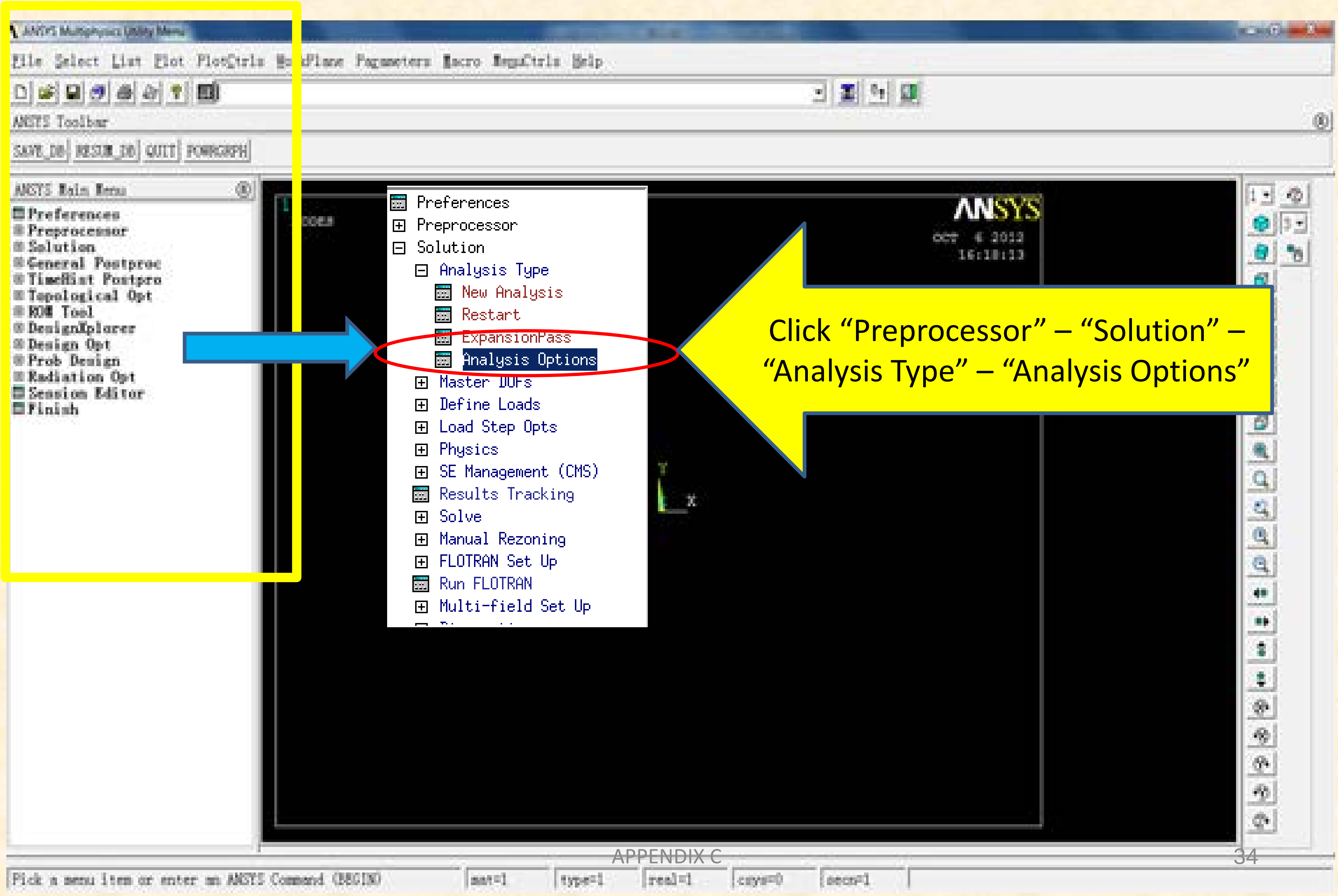
ANSYS Multiphysics Utility Menu
File Select List Plot PlotCtrls WorkPlane Parameters Macro MenuCtrls Help
ANSYS Toolbar
SAVE_DB RESUM_DB QUIT POWRGRPH
ANSYS Main Menu
Preferences
Preprocessor
Solution
General Postproc
TimeHist Postpro
Topological Opt
ROM Tool
DesignXplorer
Design Opt
Prob Design
Radiation Opt
Session Editor
Finish
Preferences
Preprocessor
Solution
Analysis Type
New Analysis
Restart
ExpansionPass
Analysis Options
Master DOFs
Define Loads
Load Step Opts
Physics
SE Management (CMS)
Results Tracking
Solve
Manual Rezoning
FLOTRAN Set Up
Run FLOTRAN
Multi-field Set Up
ANSYS
Y
X
Pick a menu item or enter an ANSYS Command (BEGIN)
mat=1
type=1
real=1
csys=0
secn=1

Click “Preprocessor” – “Solution” – “Analysis Type” – “Analysis Options”

Substructuring/CMS

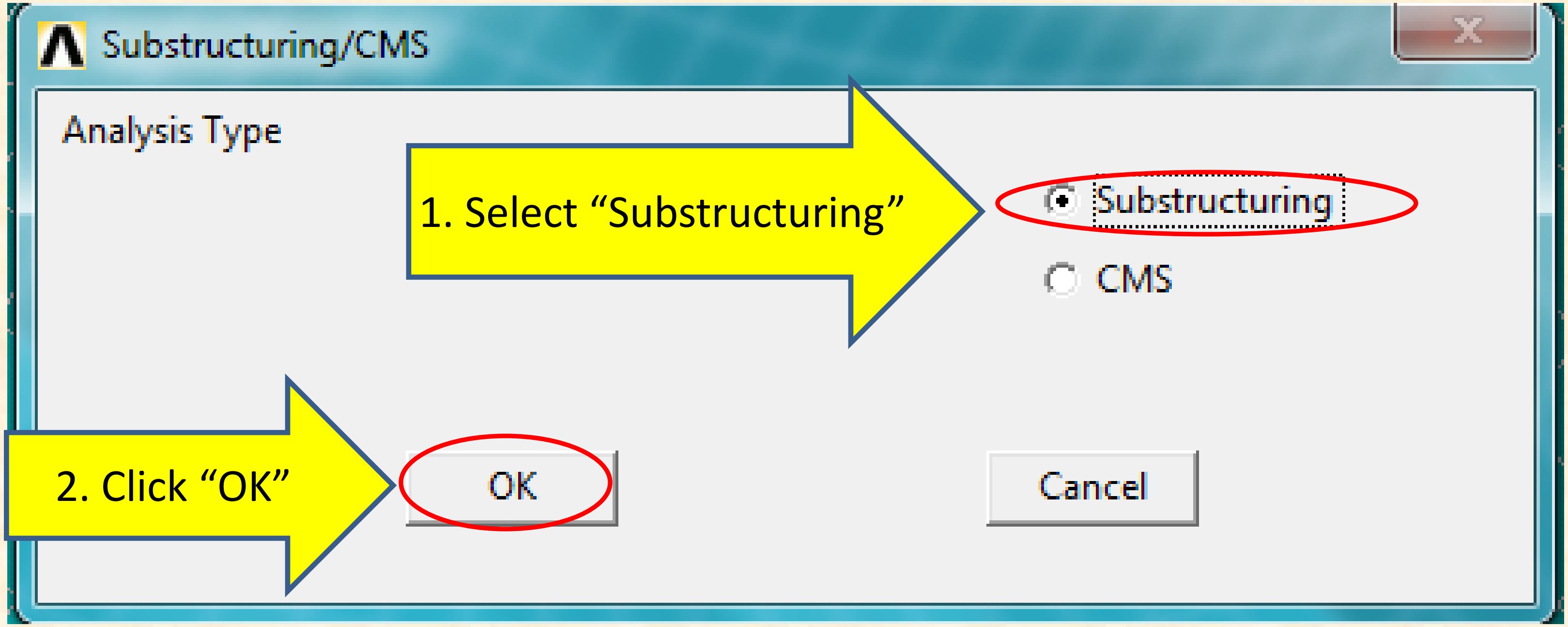

Substructuring/CMS

Analysis Type

● Substructuring

○ CMS

1. Select “Substructuring”

2. Click “OK”

Substructuring Analysis

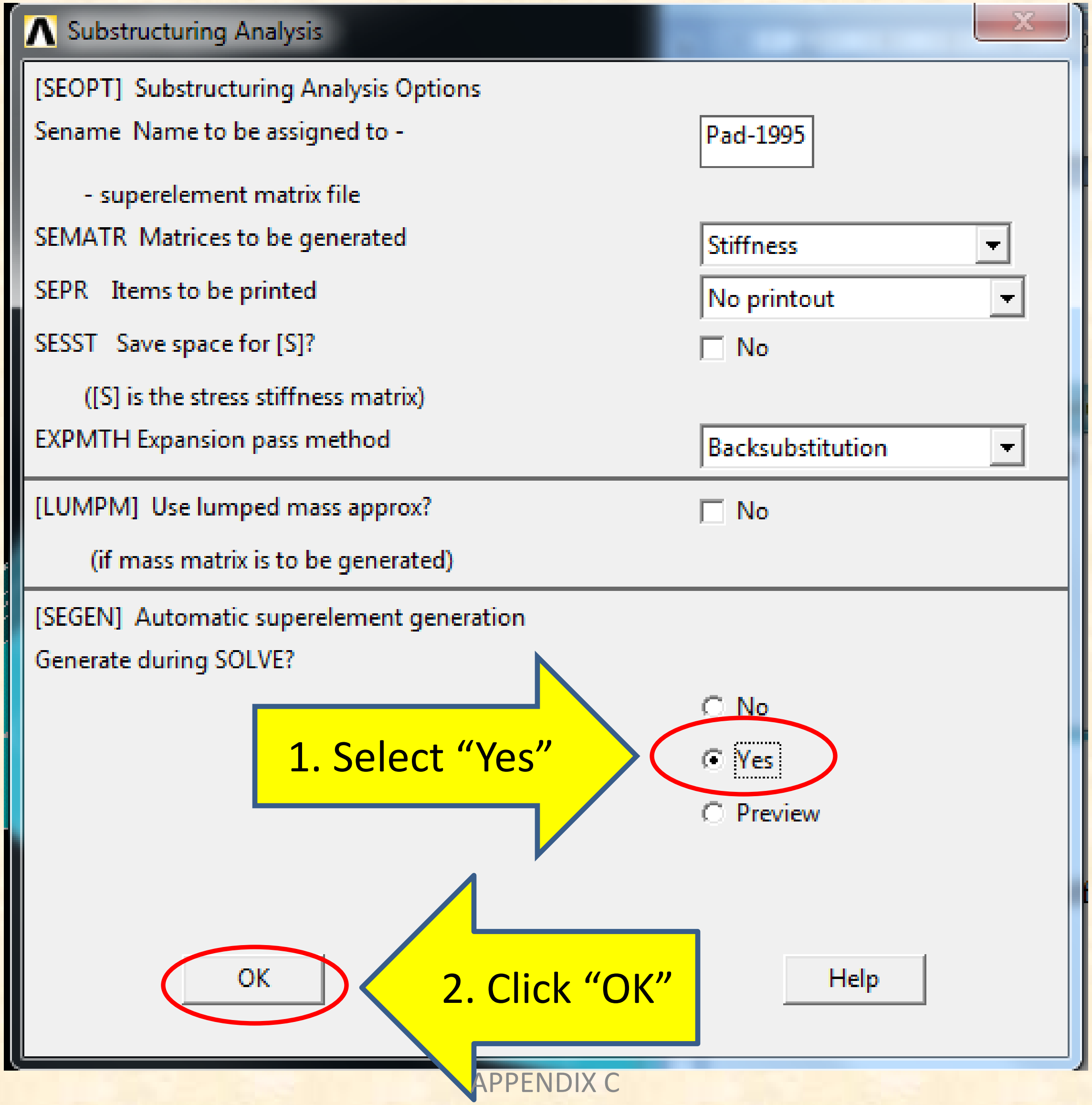

Substructuring Analysis

[SEOPT] Substructuring Analysis Options

Sename Name to be assigned to - - superelement matrix file: Pad-1995

SEMATR Matrices to be generated: Stiffness

SEPR Items to be printed: No printout

SESST Save space for [S]? ([S] is the stress stiffness matrix): ☐ No

EXPMTH Expansion pass method: Backsubstitution

[LUMPM] Use lumped mass approx? (if mass matrix is to be generated): ☐ No

[SEGEN] Automatic superelement generation

Generate during SOLVE?

○ No
● Yes
○ Preview

1. Select "Yes"

2. Click "OK"

Main interface

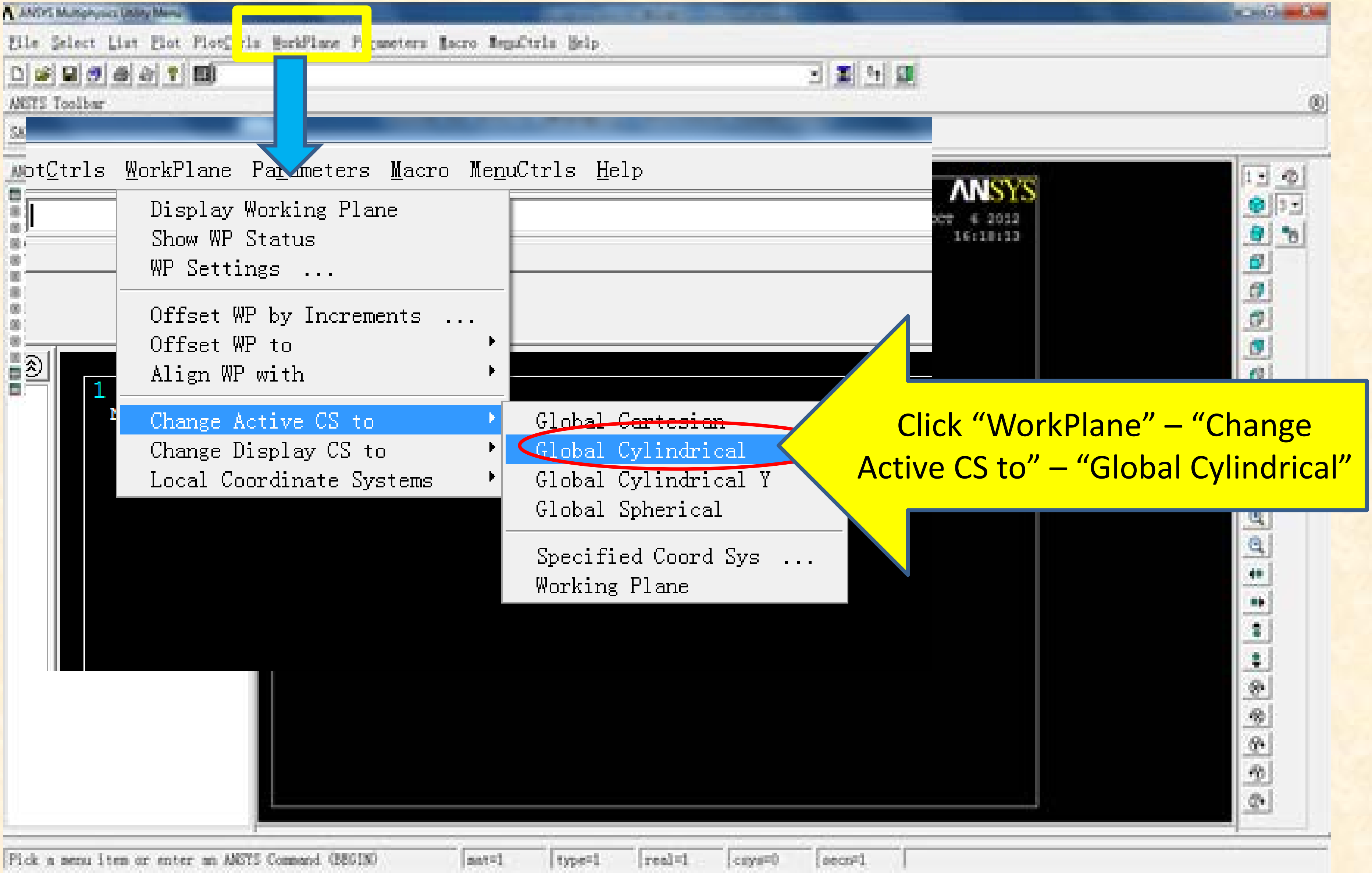
ANSYS Multiphysics Utility Menu
File Select List Plot PlotCtrls WorkPlane Parameters Macro MenuCtrls Help
ANSYS Toolbar
PlotCtrls WorkPlane Parameters Macro MenuCtrls Help
Display Working Plane
Show WP Status
WP Settings ...
Offset WP by Increments ...
Offset WP to
Align WP with
Change Active CS to
Change Display CS to
Local Coordinate Systems
Global Cartesian
Global Cylindrical
Global Cylindrical Y
Global Spherical
Specified Coord Sys ...
Working Plane
ANSYS
Pick a menu item or enter an ANSYS Command (BEGIN)
mat=1
type=1
real=1
csys=0
secn=1

Click “WorkPlane” – “Change Active CS to” – “Global Cylindrical”

Main interface

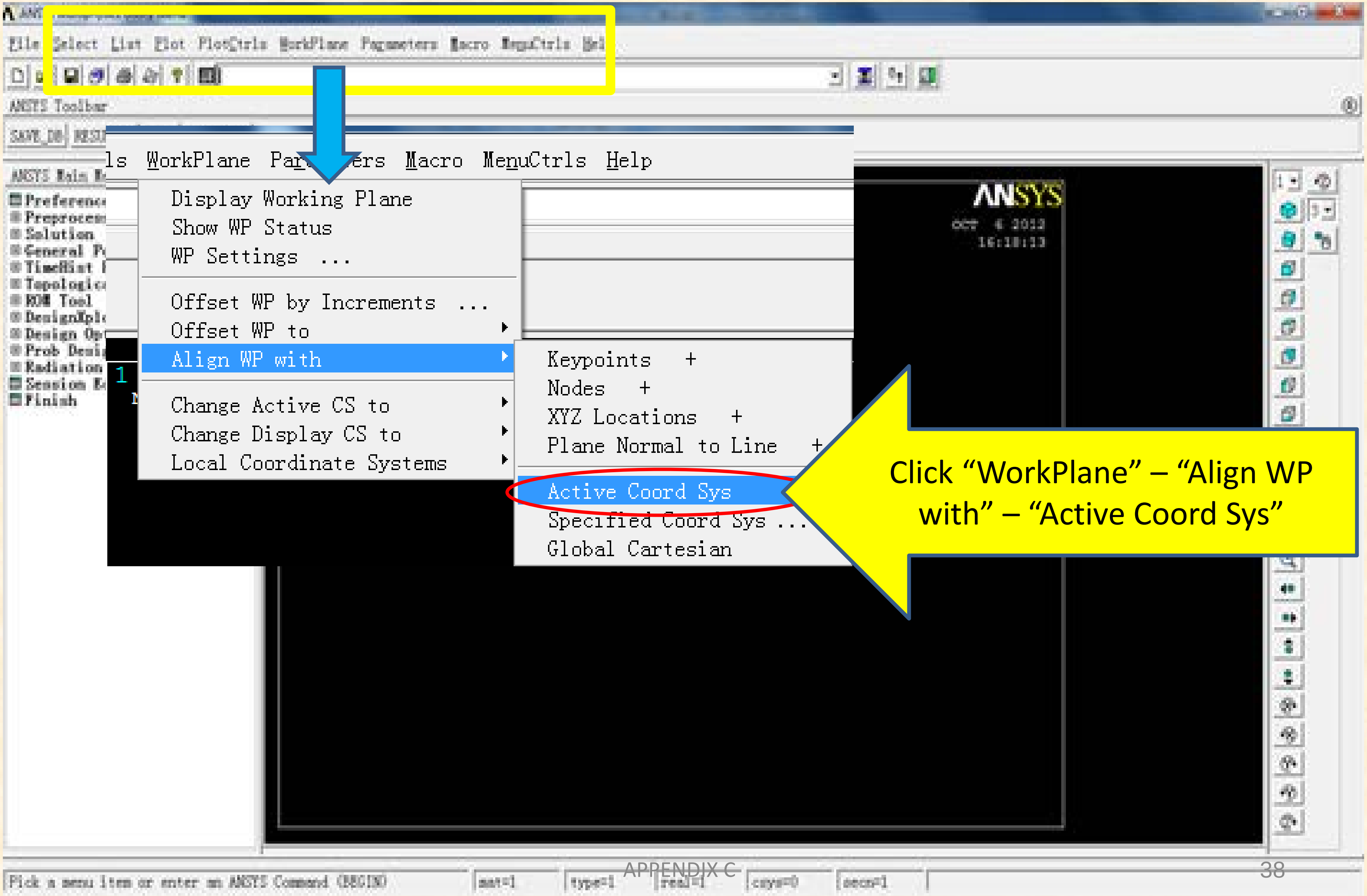
File Select List Plot PlotCtrls WorkPlane Parameters Macro MenuCtrls Help
ANSYS Toolbar
SAVE_DB RESUM
ANSYS Main Menu
Preferences
Preprocessor
Solution
General Postproc
TimeHist Postpro
Topological Opt
ROM Tool
DesignXplorer
Design Opt
Prob Design
Radiation Opt
Session Editor
Finish
ls WorkPlane Parameters Macro MenuCtrls Help
Display Working Plane
Show WP Status
WP Settings ...
Offset WP by Increments ...
Offset WP to
Align WP with
Change Active CS to
Change Display CS to
Local Coordinate Systems
Keypoints +
Nodes +
XYZ Locations +
Plane Normal to Line +
Active Coord Sys
Specified Coord Sys ...
Global Cartesian
ANSYS
OCT 6 2012
16:18:13
Pick a menu item or enter an ANSYS Command (BEGIN)
mat=1
type=1
real=1
csys=0
secn=1

Click “WorkPlane” – “Align WP with” – “Active Coord Sys”

Main interface

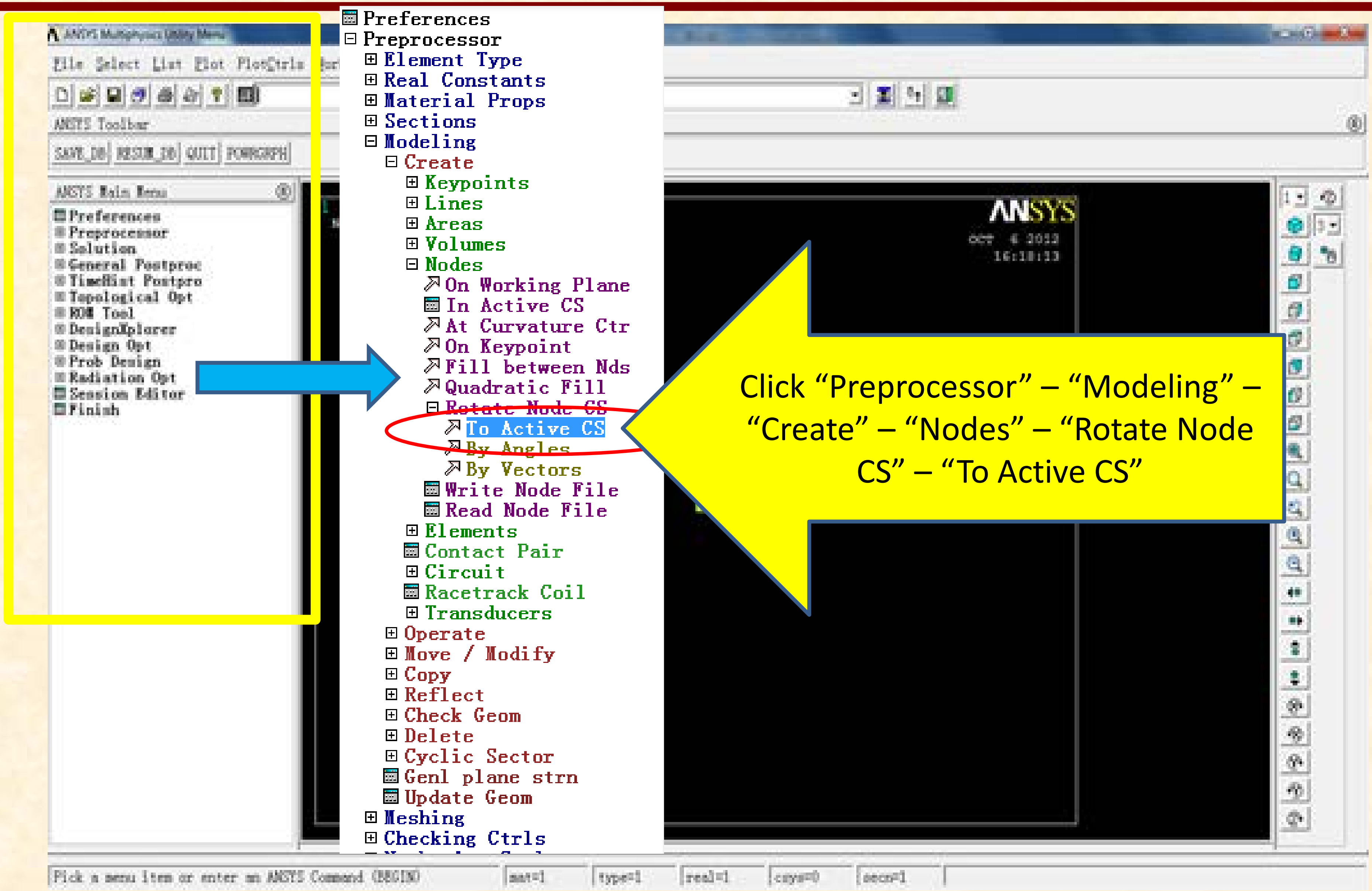
ANSYS Multiphysics Utility Menu
File Select List Plot PlotCtrls
ANSYS Toolbar
SAVE_DB RESUM_DB QUIT POWRGRPH
ANSYS Main Menu
Preferences
Preprocessor
Solution
General Postproc
TimeHist Postpro
Topological Opt
ROM Tool
DesignXplorer
Design Opt
Prob Design
Radiation Opt
Session Editor
Finish
Preferences
Preprocessor
Element Type
Real Constants
Material Props
Sections
Modeling
Create
Keypoints
Lines
Areas
Volumes
Nodes
On Working Plane
In Active CS
At Curvature Ctr
On Keypoint
Fill between Nds
Quadratic Fill
Rotate Node CS
To Active CS
By Angles
By Vectors
Write Node File
Read Node File
Elements
Contact Pair
Circuit
Racetrack Coil
Transducers
Operate
Move / Modify
Copy
Reflect
Check Geom
Delete
Cyclic Sector
Genl plane strn
Update Geom
Meshing
Checking Ctrls
ANSYS
OCT 6 2012
16:18:13
Pick a menu item or enter an ANSYS Command (BEGIN)
mat=1
type=1
real=1
csys=0
secn=1

Click “Preprocessor” – “Modeling” – “Create” – “Nodes” – “Rotate Node CS” – “To Active CS”

Rotate Nodes into CS

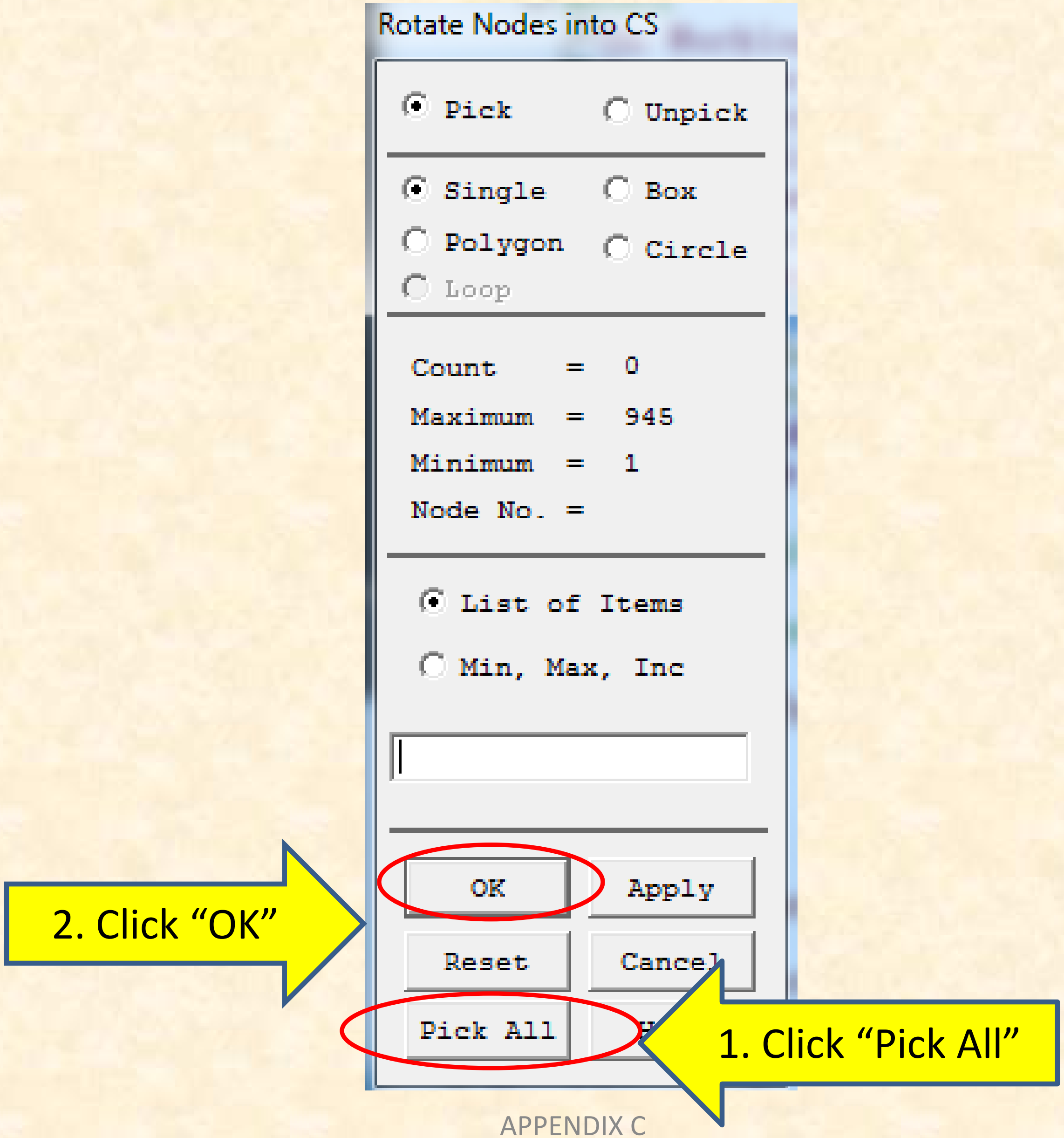

Rotate Nodes into CS

● Pick ○ Unpick

● Single ○ Box
○ Polygon ○ Circle
○ Loop

Count = 0
Maximum = 945
Minimum = 1
Node No. =

● List of Items
○ Min, Max, Inc

OK
Apply
Reset
Cancel
Pick All

2. Click “OK”

1. Click “Pick All”

Main interface

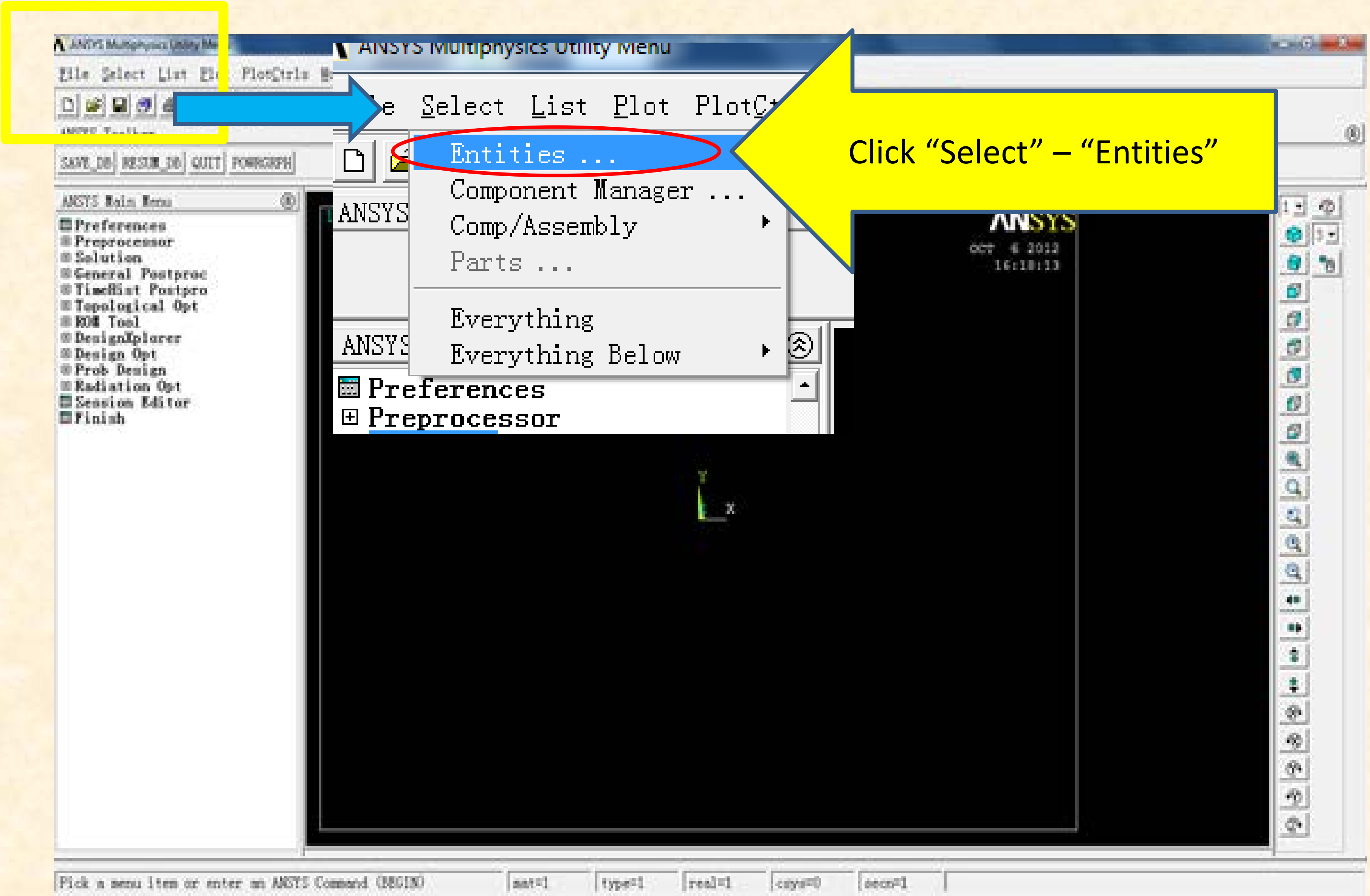
ANSYS Multiphysics Utility Menu
File Select List Plot PlotCtrls
ANSYS Toolbar
SAVE_DB RESUM_DB QUIT POWRGRPH
Entities ...
Component Manager ...
Comp/Assembly
Parts ...
Everything
Everything Below
ANSYS Main Menu
Preferences
Preprocessor
Solution
General Postproc
TimeHist Postpro
Topological Opt
ROM Tool
DesignXplorer
Design Opt
Prob Design
Radiation Opt
Session Editor
Finish
ANSYS
OCT 6 2012
16:18:13
Y
X
Pick a menu item or enter an ANSYS Command (BEGIN)
mat=1
type=1
real=1
csys=0
secn=1

Click “Select” – “Entities”

Select Entities

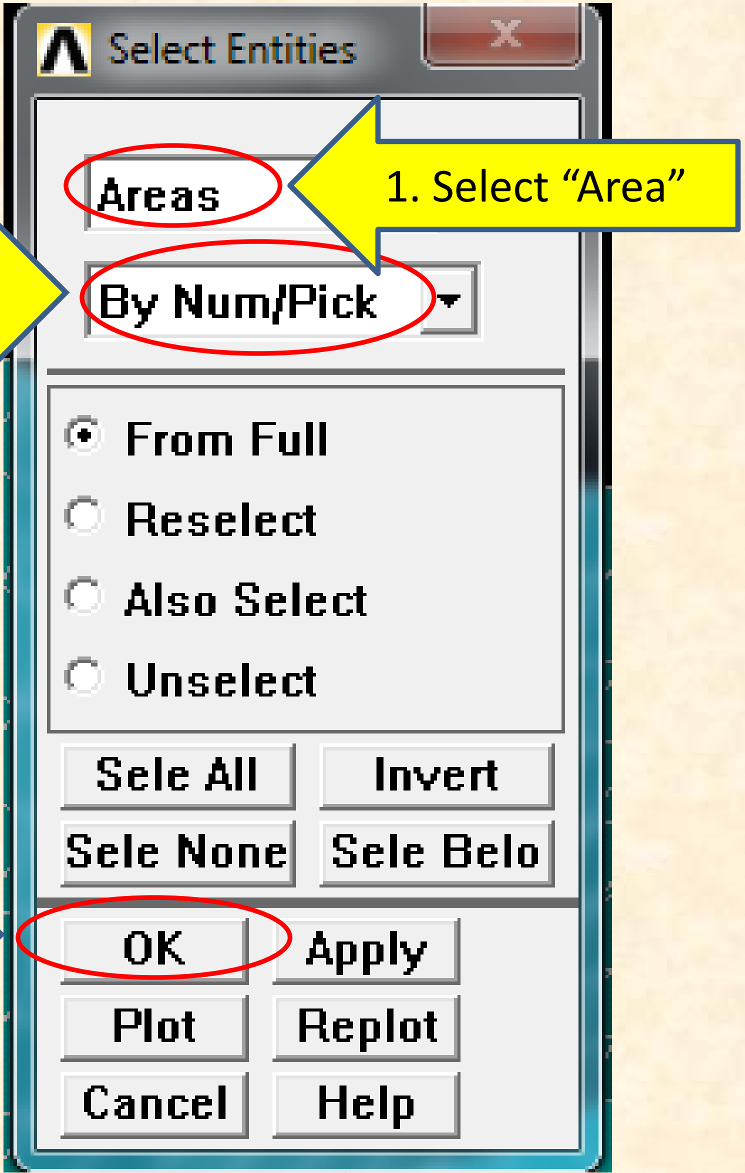

Select Entities
Areas
By Num/Pick
○ From Full
○ Reselect
○ Also Select
○ Unselect
Sele All
Invert
Sele None
Sele Belo
OK
Apply
Plot
Replot
Cancel
Help

1. Select "Area"

2. Select "Num/Pick"

3. Click "OK"

Select areas

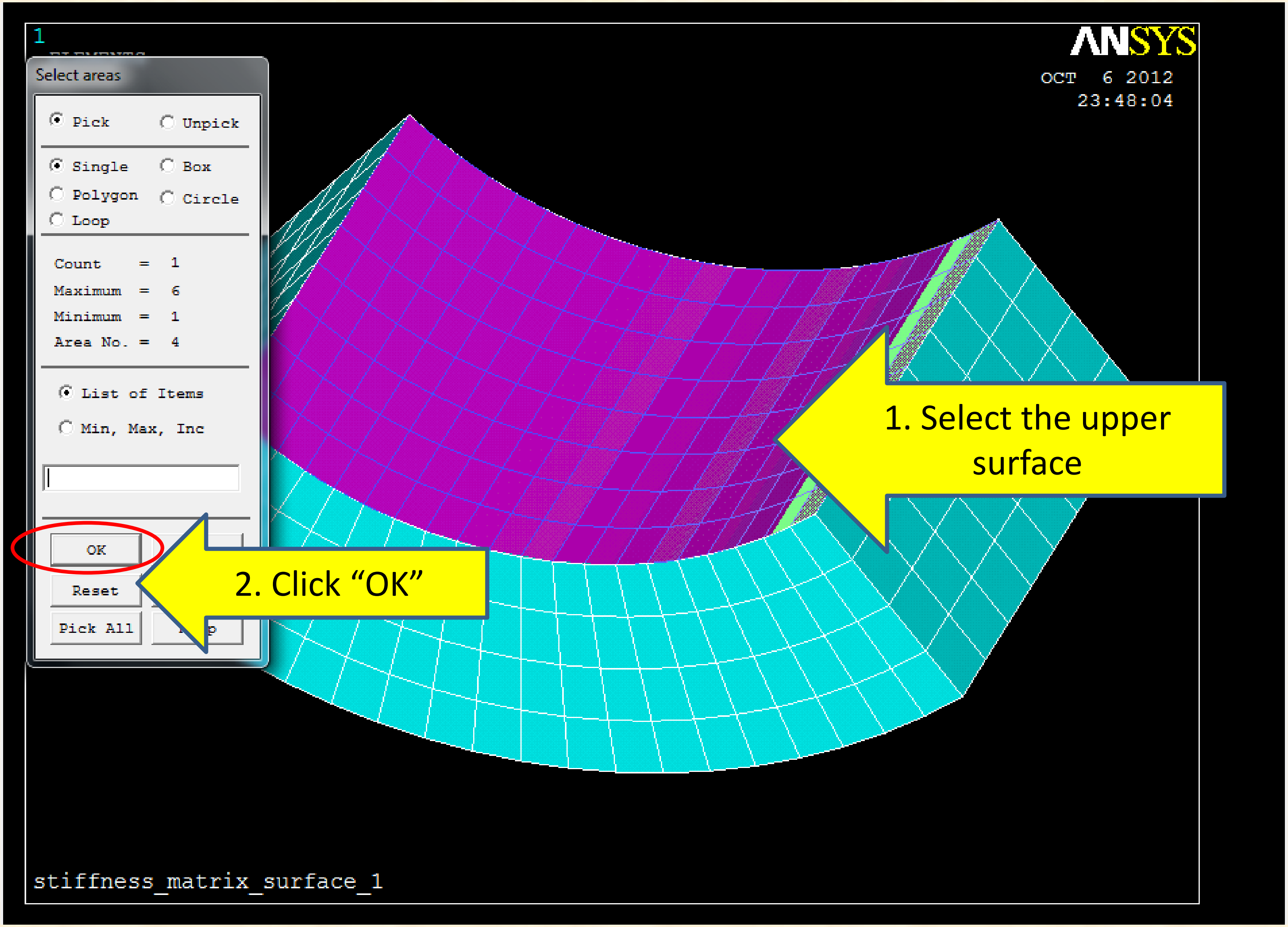

Select areas

● Pick ○ Unpick

● Single ○ Box
○ Polygon ○ Circle
○ Loop

Count = 1
Maximum = 6
Minimum = 1
Area No. = 4

● List of Items
○ Min, Max, Inc

OK
Reset
Pick All
1
ANSYS
OCT 6 2012
23:48:04
stiffness_matrix_surface_1

1. Select the upper surface

2. Click “OK”

Main interface

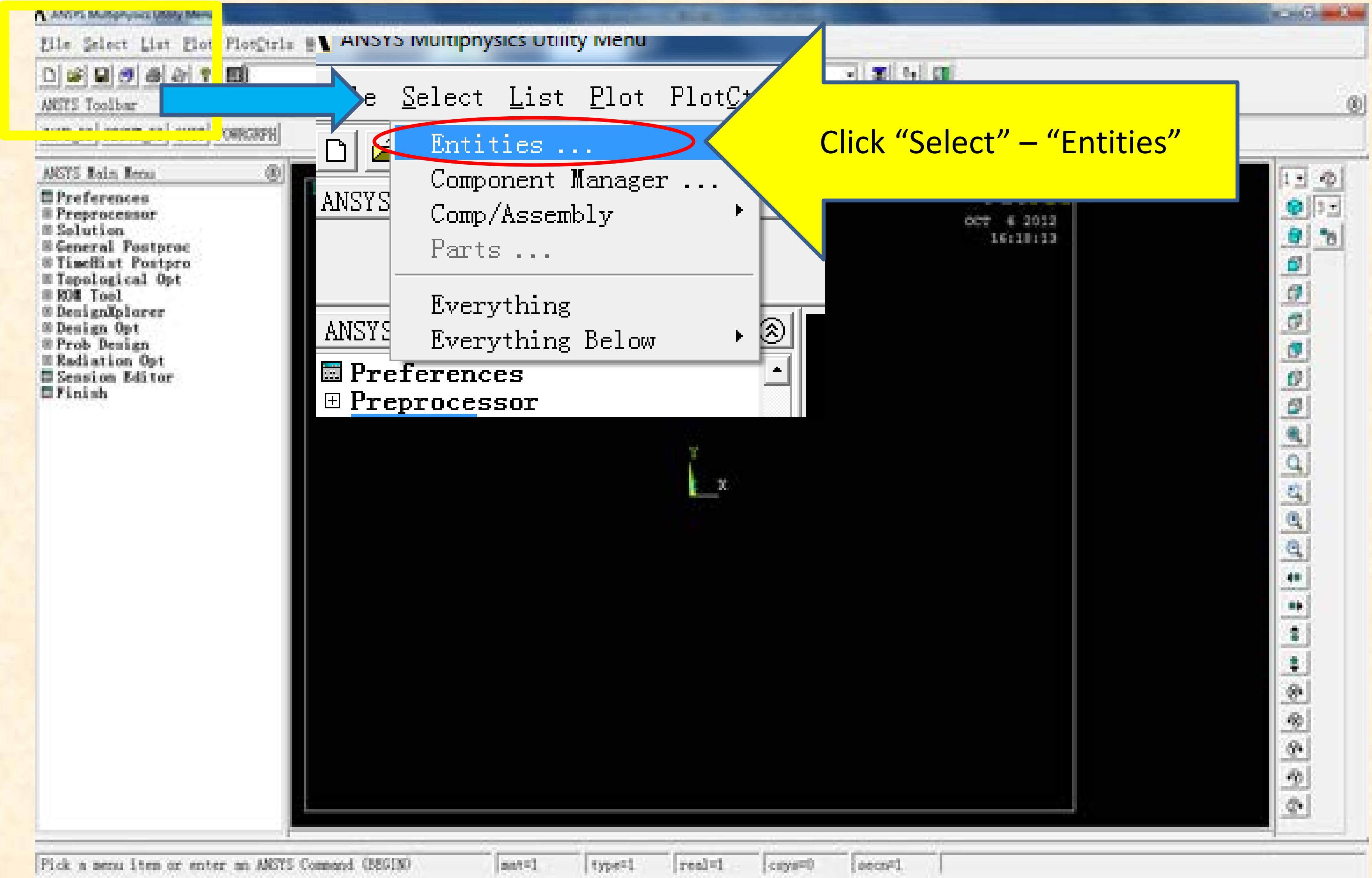

ANSYS Multiphysics Utility Menu
File Select List Plot PlotCtrls
Entities ...
Component Manager ...
Comp/Assembly
Parts ...
Everything
Everything Below
ANSYS Toolbar
ANSYS Main Menu
Preferences
Preprocessor
Solution
General Postproc
TimeHist Postpro
Topological Opt
ROM Tool
DesignXplorer
Design Opt
Prob Design
Radiation Opt
Session Editor
Finish
Pick a menu item or enter an ANSYS Command (BEGIN)
mat=1
type=1
real=1
csys=0
secn=1

Click “Select” – “Entities”

Select Entities

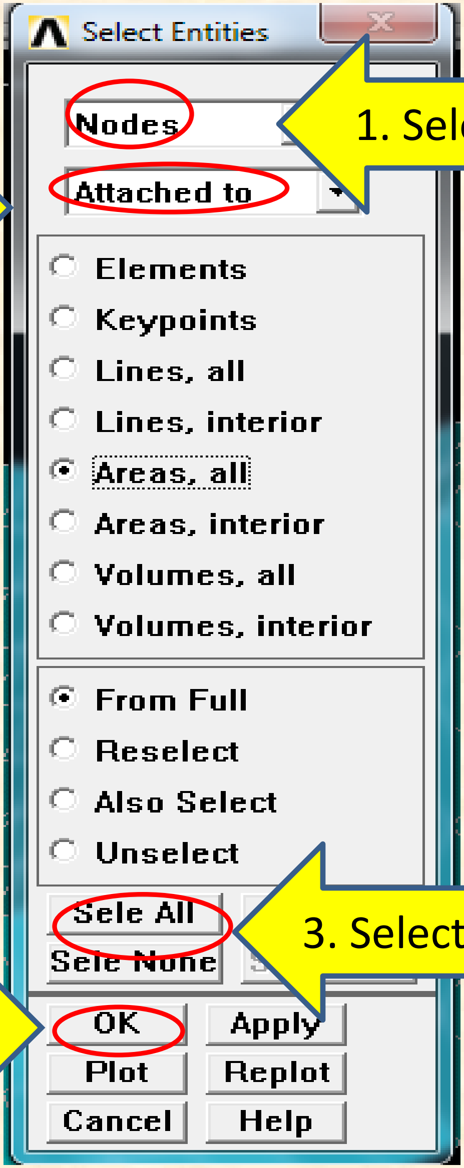

Select Entities

Nodes

Attached to

○ Elements
○ Keypoints
○ Lines, all
○ Lines, interior
● Areas, all
○ Areas, interior
○ Volumes, all
○ Volumes, interior

● From Full
○ Reselect
○ Also Select
○ Unselect

Sele All
Sele None
OK
Apply
Plot
Replot
Cancel
Help

1. Select “Nodes”

2. Select “Attached to”

3. Select “Sele All”

4. Select “OK”

Main interface

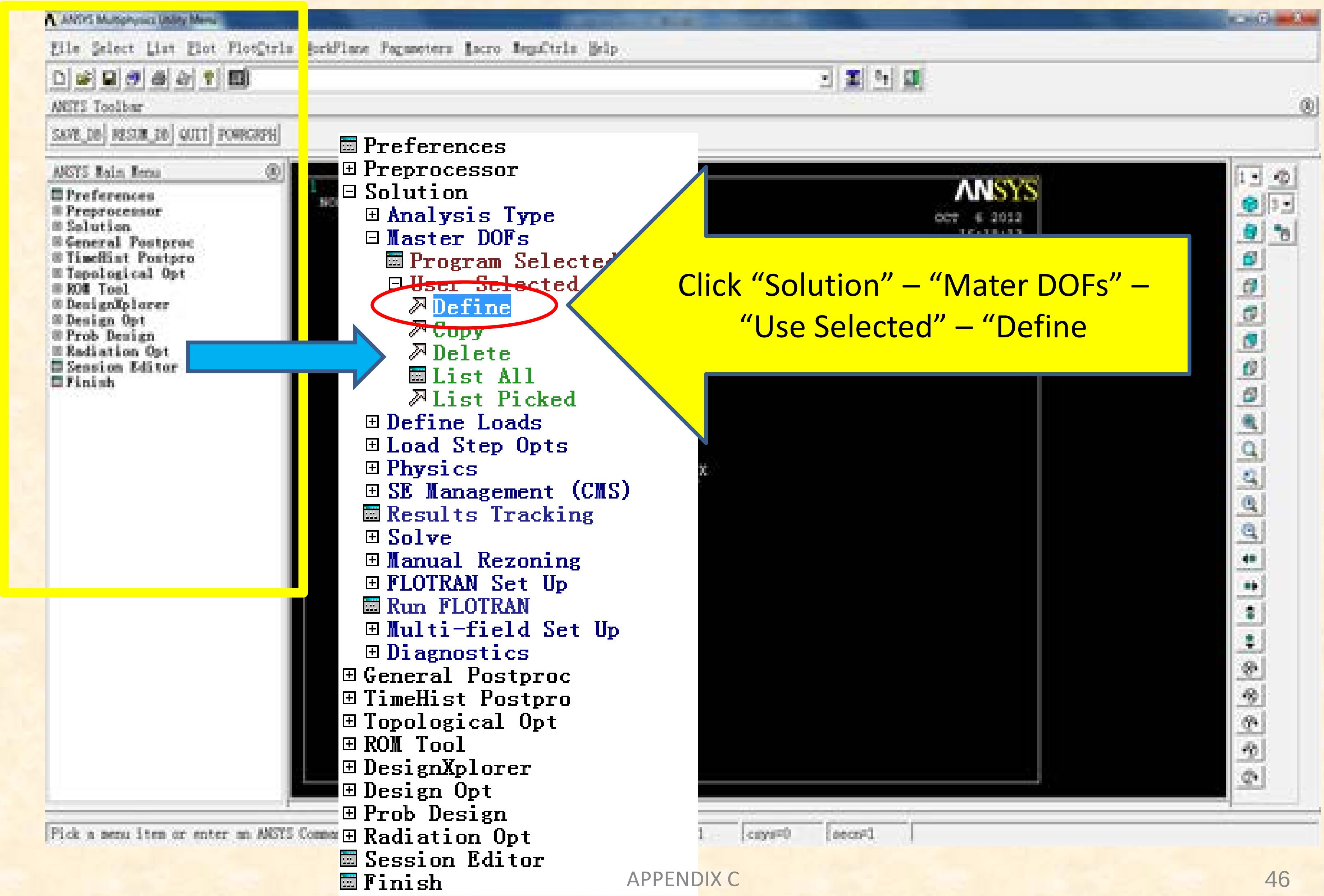
ANSYS Multiphysics Utility Menu
File Select List Plot PlotCtrls WorkPlane Parameters Macro MenuCtrls Help
ANSYS Toolbar
SAVE_DB RESUM_DB QUIT POWRGRPH
ANSYS Main Menu
ANSYS
Preferences
Preprocessor
Solution
Analysis Type
Master DOFs
Program Selected
User Selected
Define
Copy
Delete
List All
List Picked
Define Loads
Load Step Opts
Physics
SE Management (CMS)
Results Tracking
Solve
Manual Rezoning
FLOTRAN Set Up
Run FLOTRAN
Multi-field Set Up
Diagnostics
General Postproc
TimeHist Postpro
Topological Opt
ROM Tool
DesignXplorer
Design Opt
Prob Design
Radiation Opt
Session Editor
Finish
Pick a menu item or enter an ANSYS Command
csys=0
secn=1

Click “Solution” – “Mater DOFs” – “Use Selected” – “Define

Define Master DOFs

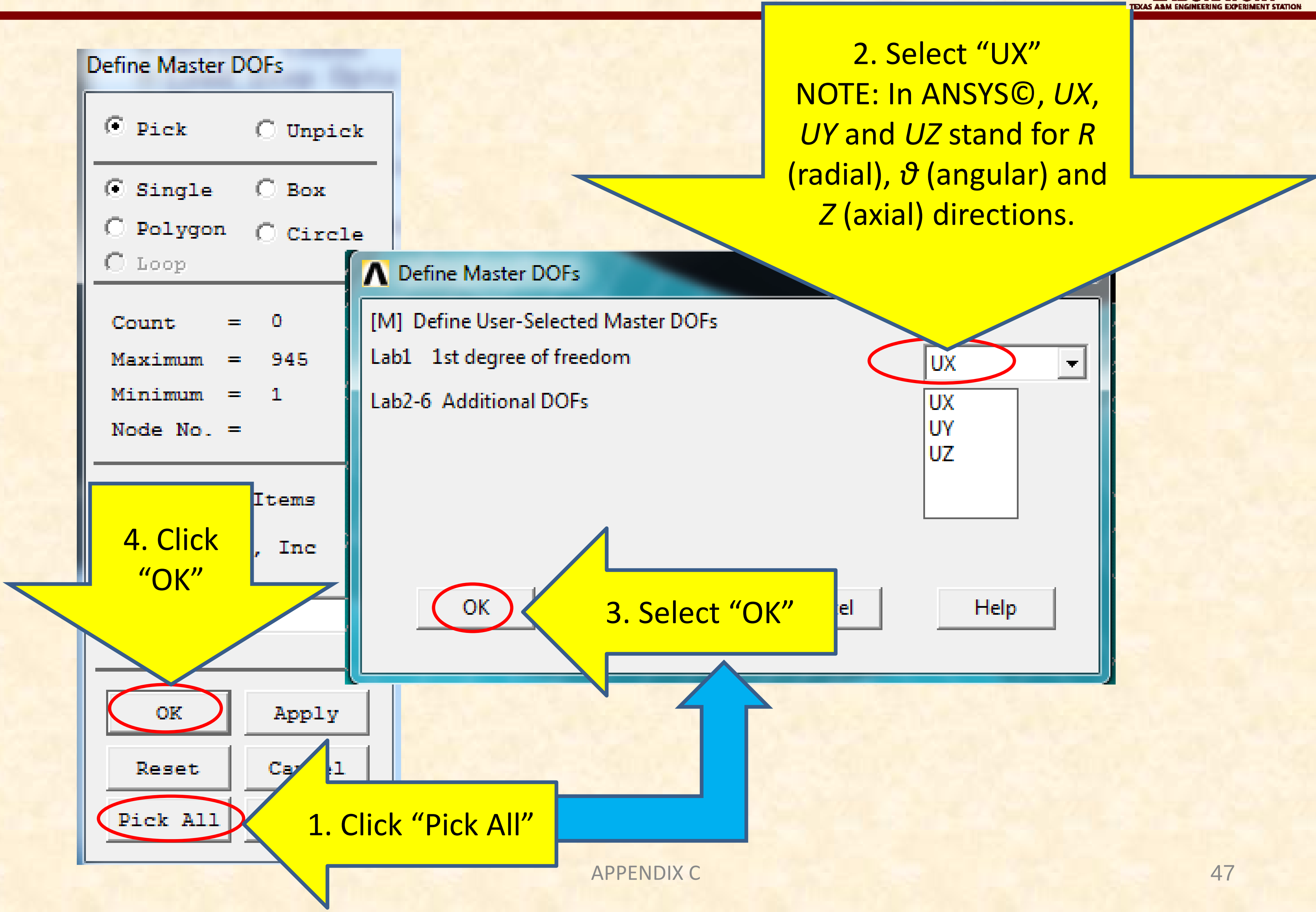

Define Master DOFs

● Pick ○ Unpick

● Single ○ Box
○ Polygon ○ Circle
○ Loop

Count = 0
Maximum = 945
Minimum = 1
Node No. =

Define Master DOFs

[M] Define User-Selected Master DOFs

Lab1 1st degree of freedom UX

Lab2-6 Additional DOFs UX UY UZ

1. Click “Pick All”

2. Select “UX”
NOTE: In ANSYS©, *UX*, *UY* and *UZ* stand for *R* (radial), *ϑ* (angular) and *Z* (axial) directions.

3. Select “OK”

4. Click “OK”

Main interface

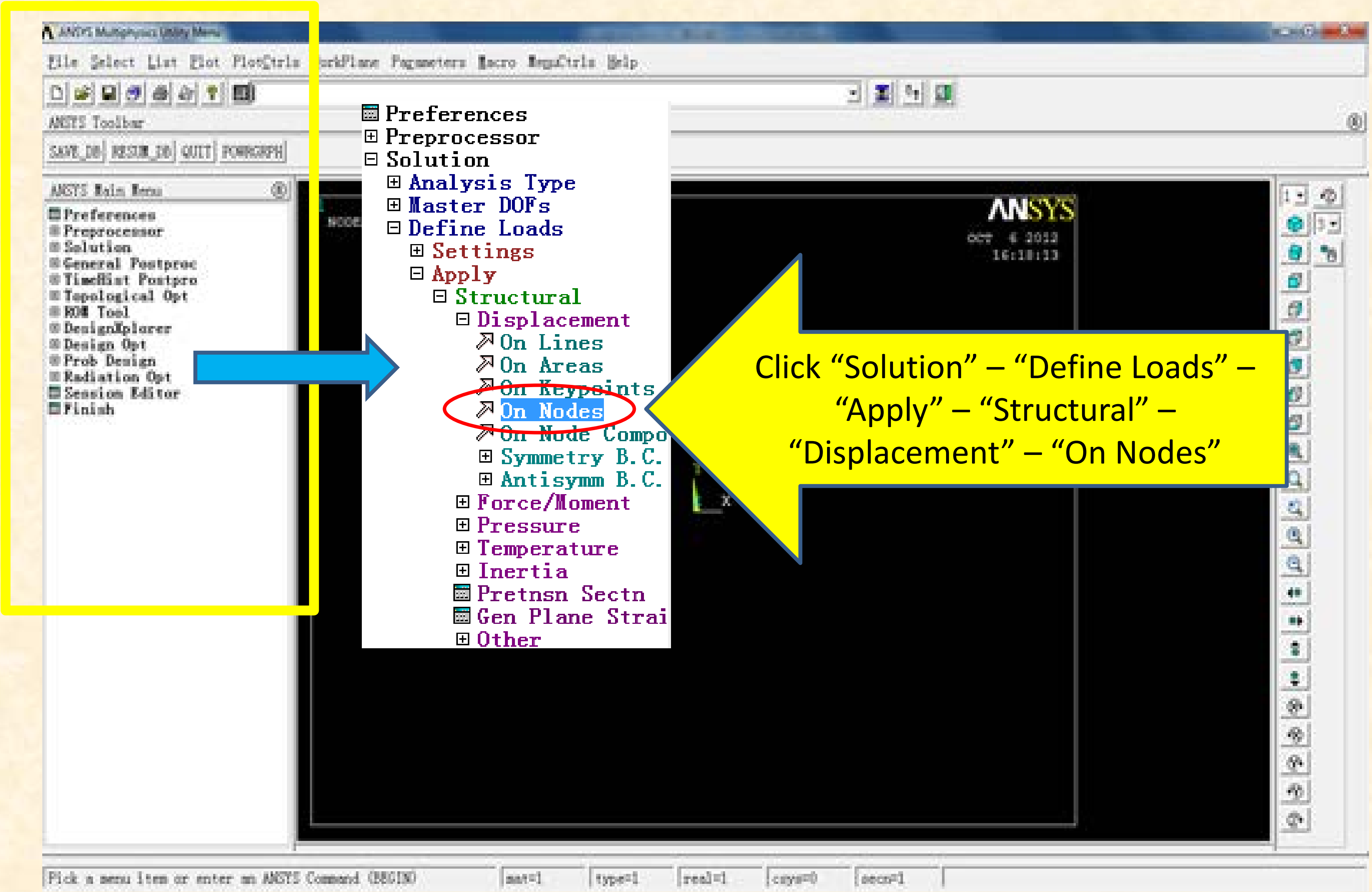
ANSYS Multiphysics Utility Menu
File Select List Plot PlotCtrls WorkPlane Parameters Macro MenuCtrls Help
ANSYS Toolbar
SAVE_DB RESUM_DB QUIT POWRGRPH
ANSYS Main Menu
Preferences
Preprocessor
Solution
General Postproc
TimeHist Postpro
Topological Opt
ROM Tool
DesignXplorer
Design Opt
Prob Design
Radiation Opt
Session Editor
Finish
Preferences
Preprocessor
Solution
Analysis Type
Master DOFs
Define Loads
Settings
Apply
Structural
Displacement
On Lines
On Areas
On Keypoints
On Nodes
On Node Compo
Symmetry B.C.
Antisymm B.C.
Force/Moment
Pressure
Temperature
Inertia
Pretnsn Sectn
Gen Plane Strai
Other
NODES
ANSYS
OCT 6 2012
16:18:13
X
Pick a menu item or enter an ANSYS Command (BEGIN)
mat=1
type=1
real=1
csys=0
secn=1

Click “Solution” – “Define Loads” – “Apply” – “Structural” – “Displacement” – “On Nodes”

Apply U, ROT on Nodes

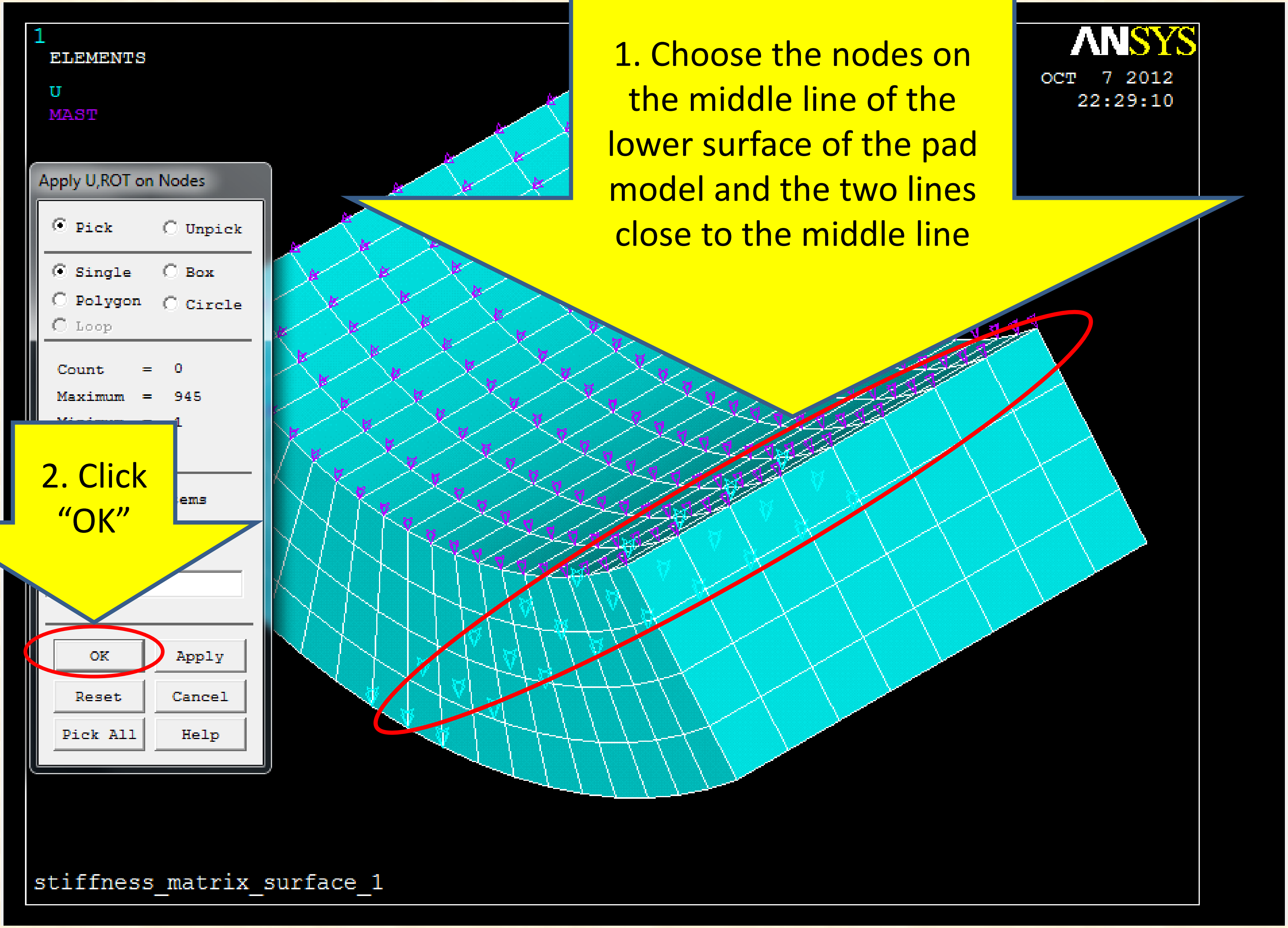
1
ELEMENTS
U
MAST
ANSYS
OCT 7 2012
22:29:10
Apply U,ROT on Nodes
Pick
Unpick
Single
Box
Polygon
Circle
Loop
ems
OK
Apply
Reset
Cancel
Pick All
Help

Count = 0
Maximum = 945

stiffness_matrix_surface_1

1. Choose the nodes on the middle line of the lower surface of the pad model and the two lines close to the middle line

2. Click "OK"

Apply U,ROT on Nodes

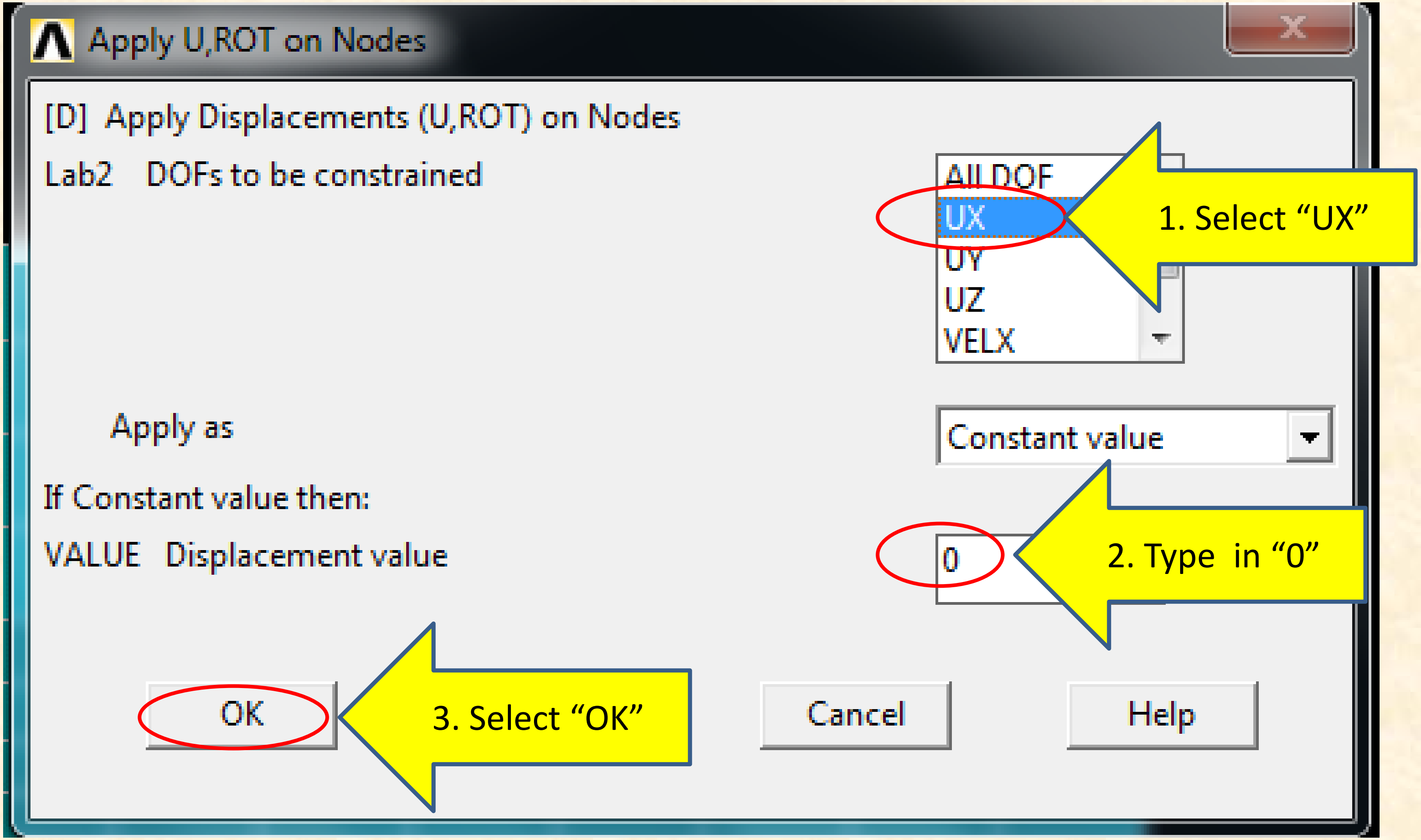

Apply U,ROT on Nodes

[D] Apply Displacements (U,ROT) on Nodes

Lab2 DOFs to be constrained: UX

Apply as: Constant value

If Constant value then:

VALUE Displacement value: 0

All DOF
UX
UY
UZ
VELX
OK
Cancel
Help

1. Select “UX”

2. Type in “0”

3. Select “OK”

Main interface

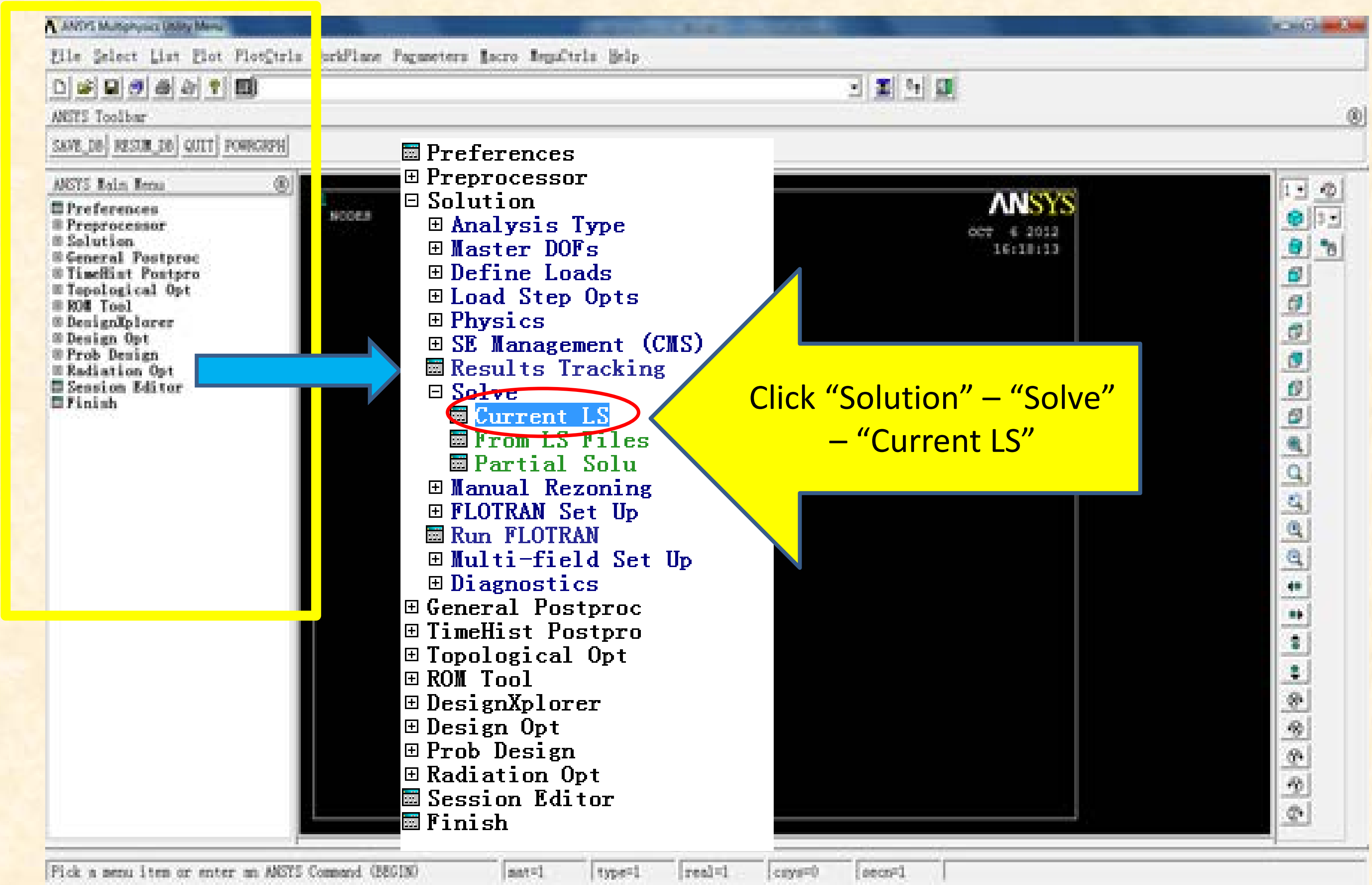
ANSYS Multiphysics Utility Menu
File Select List Plot PlotCtrls WorkPlane Parameters Macro MenuCtrls Help
ANSYS Toolbar
SAVE_DB RESUM_DB QUIT POWRGRPH
ANSYS Main Menu
Preferences
Preprocessor
Solution
General Postproc
TimeHist Postpro
Topological Opt
ROM Tool
DesignXplorer
Design Opt
Prob Design
Radiation Opt
Session Editor
Finish
NODES
ANSYS
OCT 6 2012
16:18:13
Preferences
Preprocessor
Solution
Analysis Type
Master DOFs
Define Loads
Load Step Opts
Physics
SE Management (CMS)
Results Tracking
Solve
Current LS
From LS Files
Partial Solu
Manual Rezoning
FLOTRAN Set Up
Run FLOTRAN
Multi-field Set Up
Diagnostics
General Postproc
TimeHist Postpro
Topological Opt
ROM Tool
DesignXplorer
Design Opt
Prob Design
Radiation Opt
Session Editor
Finish
Pick a menu item or enter an ANSYS Command (BEGIN)
mat=1
type=1
real=1
csys=0
secn=1

Click “Solution” – “Solve” – “Current LS”

Solve Current Load Step

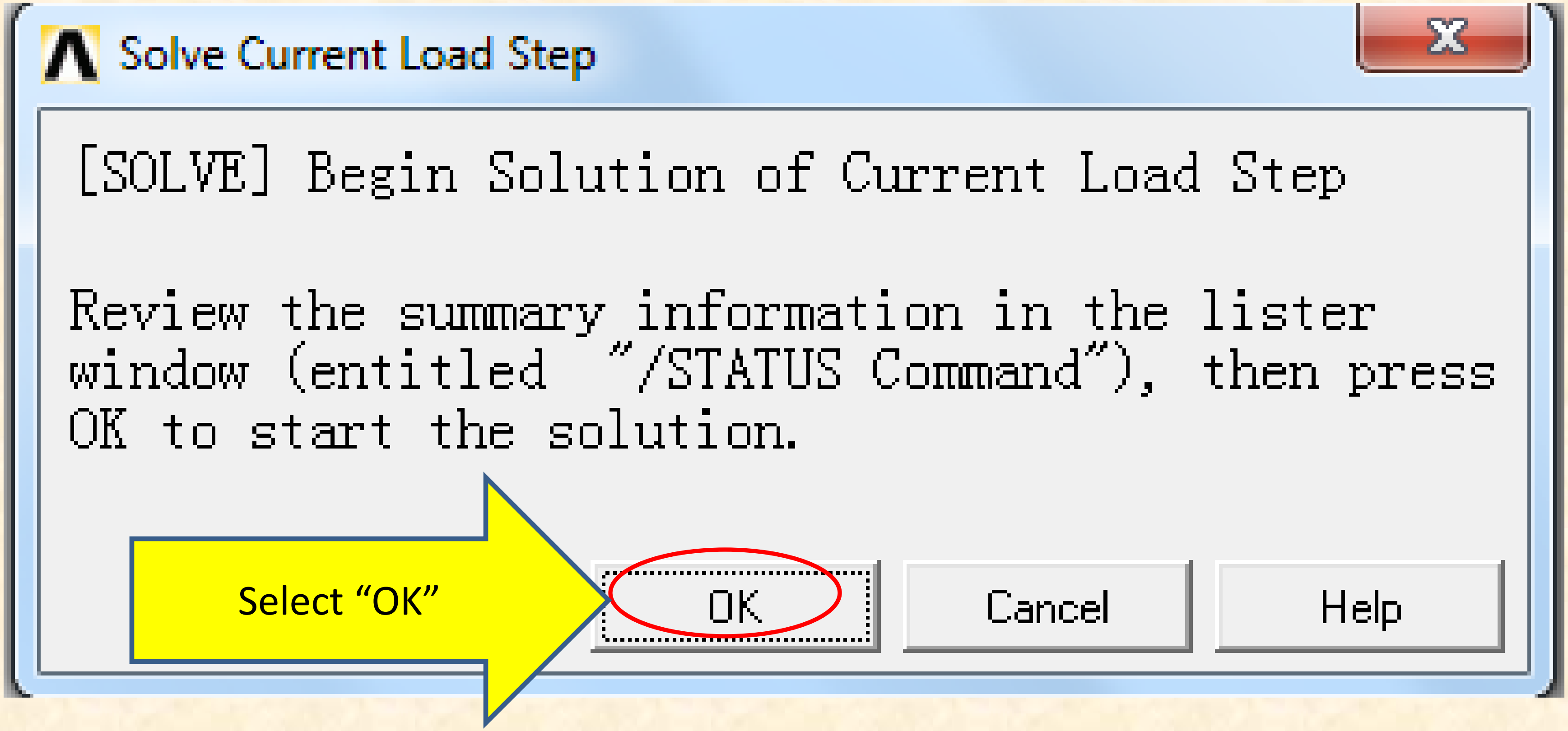
Solve Current Load Step

[SOLVE] Begin Solution of Current Load Step

Review the summary information in the lister window (entitled "/STATUS Command"), then press OK to start the solution.

Select "OK"

Rotate Nodes into CS

After solving the problem, the dialog box showing “Solution is done” will appear. Click “Close” to close the window.

Main interface

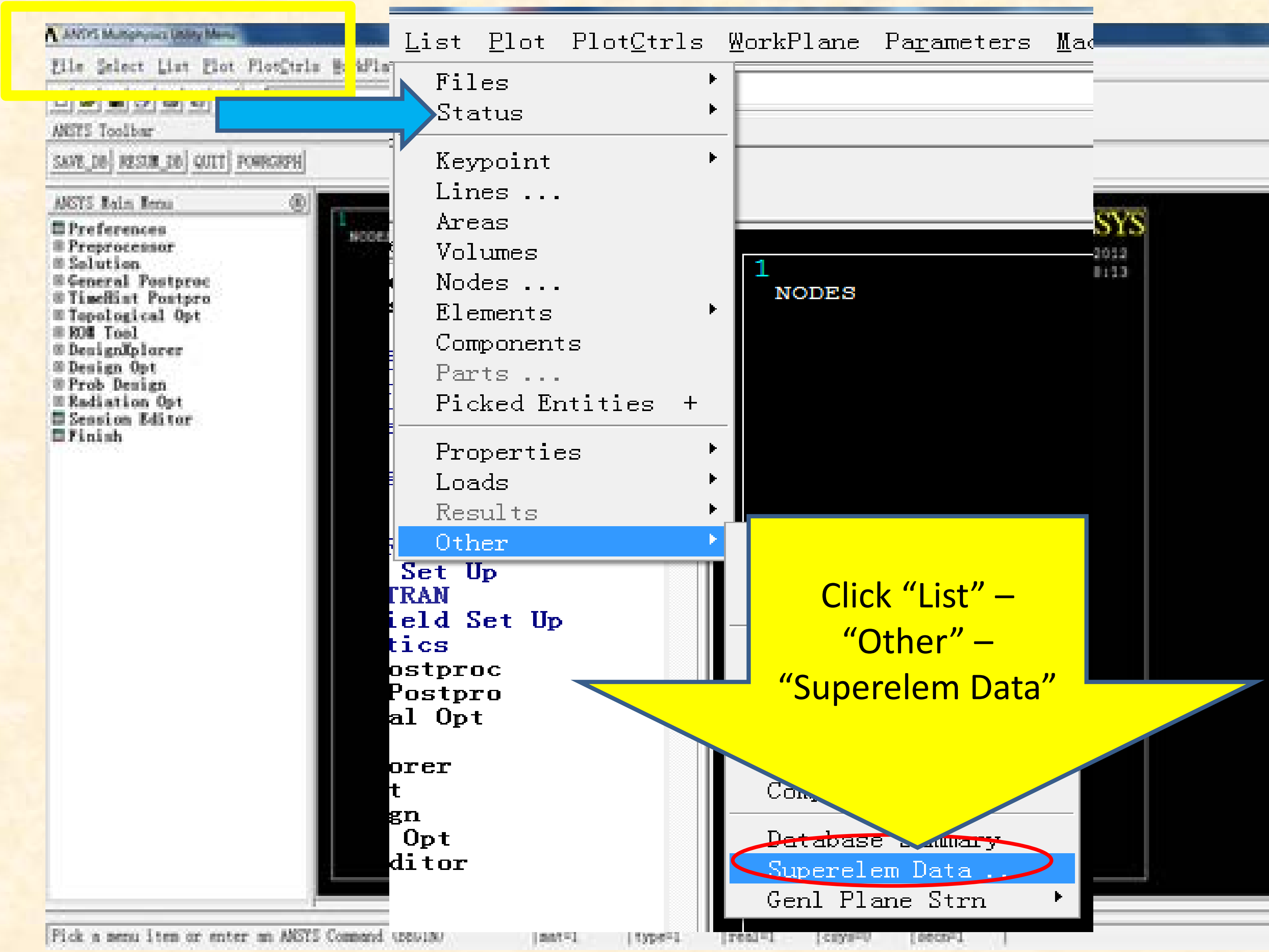
ANSYS Multiphysics Utility Menu
File Select List Plot PlotCtrls WorkPlane Parameters Macro
ANSYS Toolbar
SAVE_DB RESUM_DB QUIT POWRGRPH
ANSYS Main Menu
Preferences
Preprocessor
Solution
General Postproc
TimeHist Postpro
Topological Opt
ROM Tool
DesignXplorer
Design Opt
Prob Design
Radiation Opt
Session Editor
Finish
Files
Status
Keypoint
Lines ...
Areas
Volumes
Nodes ...
Elements
Components
Parts ...
Picked Entities +
Properties
Loads
Results
Other
1
NODES
Database Summary
Superelem Data ...
Genl Plane Strn
Pick a menu item or enter an ANSYS Command

Click “List” – “Other” – “Superelem Data”

List Superelement Data

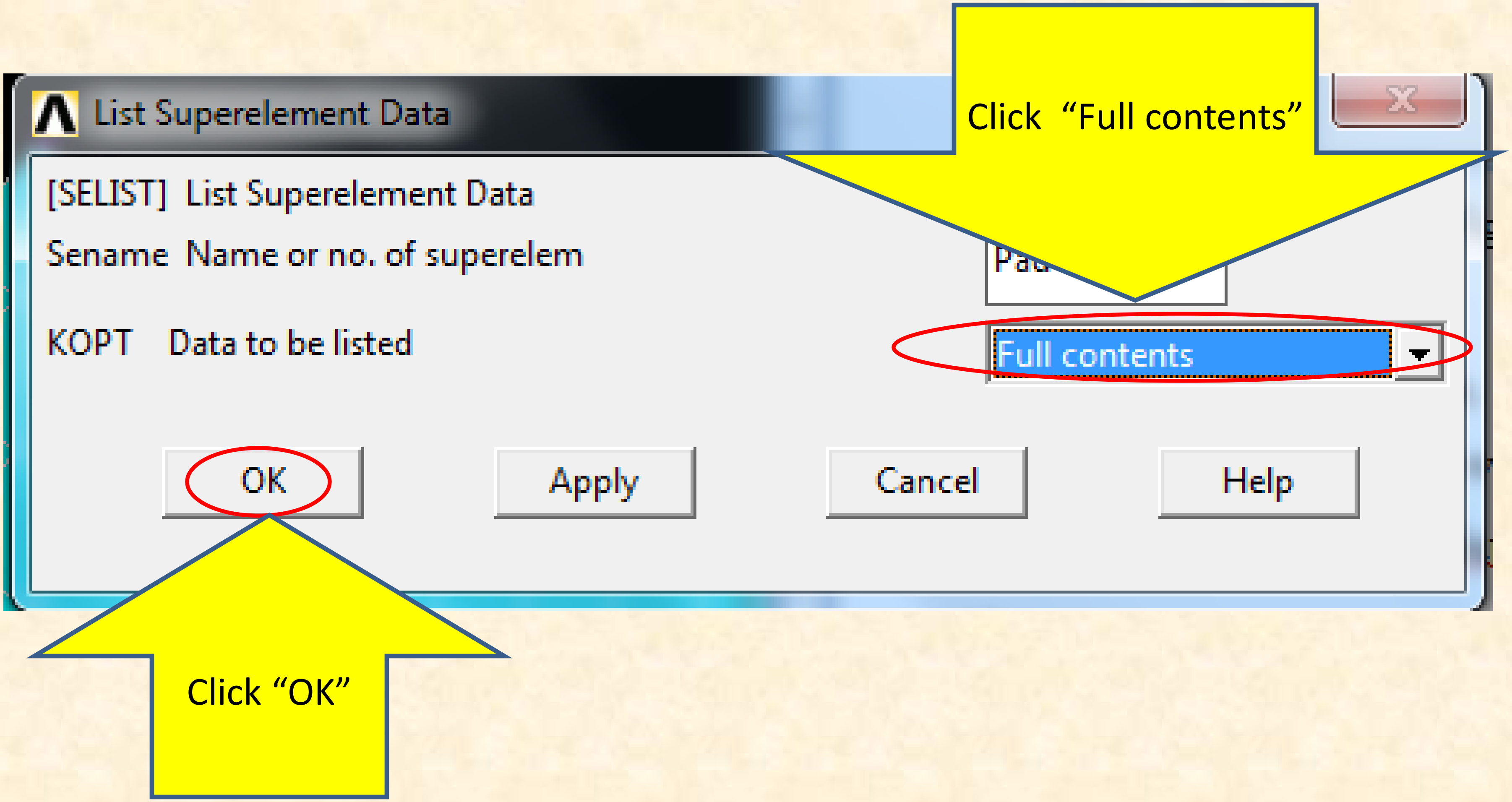

List Superelement Data

[SELIST] List Superelement Data

Sename Name or no. of superelem

KOPT Data to be listed: Full contents

Click “Full contents”

Click “OK”

List of stiffness matrix

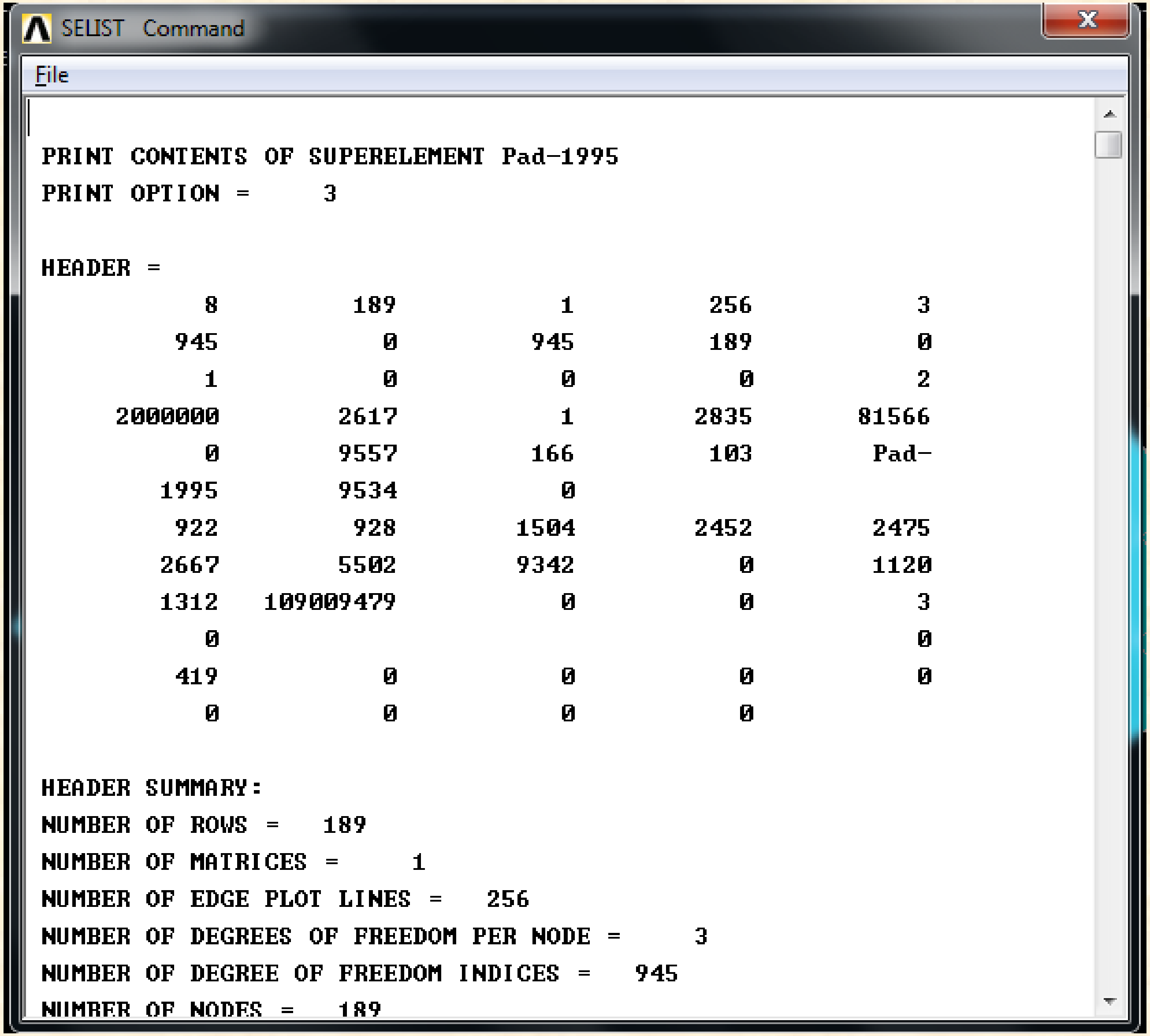

```
PRINT CONTENTS OF SUPERELEMENT Pad-1995
PRINT OPTION =     3

HEADER =
           8         189           1         256           3
         945           0         945         189           0
           1           0           0           0           2
     2000000        2617           1        2835       81566
           0        9557         166         103        Pad-
        1995        9534           0
         922         928        1504        2452        2475
        2667        5502        9342           0        1120
        1312   109009479           0           0           3
           0                                               0
         419           0           0           0           0
           0           0           0           0

HEADER SUMMARY:
NUMBER OF ROWS =   189
NUMBER OF MATRICES =     1
NUMBER OF EDGE PLOT LINES =   256
NUMBER OF DEGREES OF FREEDOM PER NODE =     3
NUMBER OF DEGREE OF FREEDOM INDICES =   945
NUMBER OF NODES =   189
```

TXT file for nodal coordinates

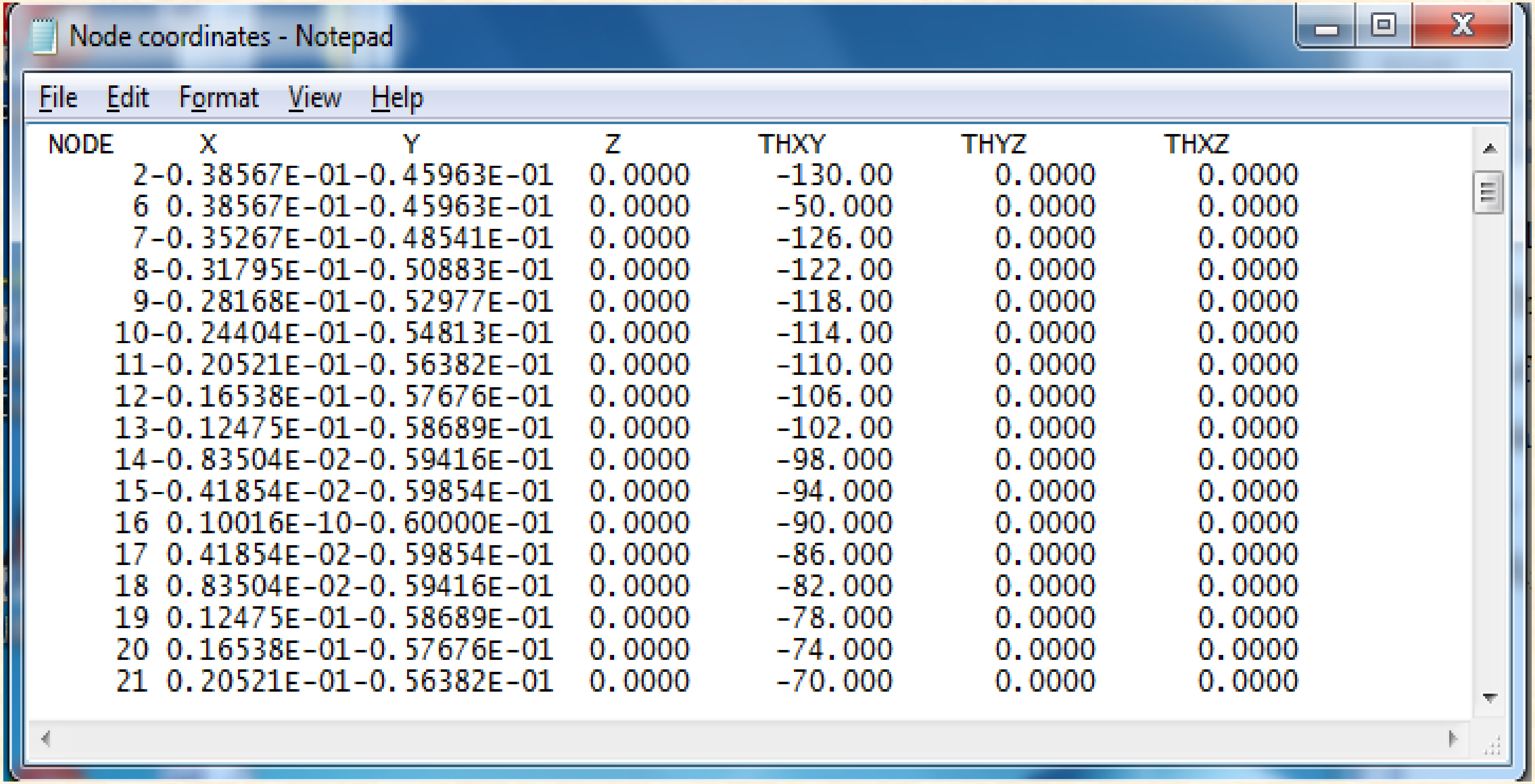

```
 NODE       X              Y              Z           THXY          THYZ          THXZ
      2-0.38567E-01-0.45963E-01  0.0000       -130.00        0.0000        0.0000
      6 0.38567E-01-0.45963E-01  0.0000       -50.000        0.0000        0.0000
      7-0.35267E-01-0.48541E-01  0.0000       -126.00        0.0000        0.0000
      8-0.31795E-01-0.50883E-01  0.0000       -122.00        0.0000        0.0000
      9-0.28168E-01-0.52977E-01  0.0000       -118.00        0.0000        0.0000
     10-0.24404E-01-0.54813E-01  0.0000       -114.00        0.0000        0.0000
     11-0.20521E-01-0.56382E-01  0.0000       -110.00        0.0000        0.0000
     12-0.16538E-01-0.57676E-01  0.0000       -106.00        0.0000        0.0000
     13-0.12475E-01-0.58689E-01  0.0000       -102.00        0.0000        0.0000
     14-0.83504E-02-0.59416E-01  0.0000       -98.000        0.0000        0.0000
     15-0.41854E-02-0.59854E-01  0.0000       -94.000        0.0000        0.0000
     16 0.10016E-10-0.60000E-01  0.0000       -90.000        0.0000        0.0000
     17 0.41854E-02-0.59854E-01  0.0000       -86.000        0.0000        0.0000
     18 0.83504E-02-0.59416E-01  0.0000       -82.000        0.0000        0.0000
     19 0.12475E-01-0.58689E-01  0.0000       -78.000        0.0000        0.0000
     20 0.16538E-01-0.57676E-01  0.0000       -74.000        0.0000        0.0000
     21 0.20521E-01-0.56382E-01  0.0000       -70.000        0.0000        0.0000
```

TXT file for stiffness matrix

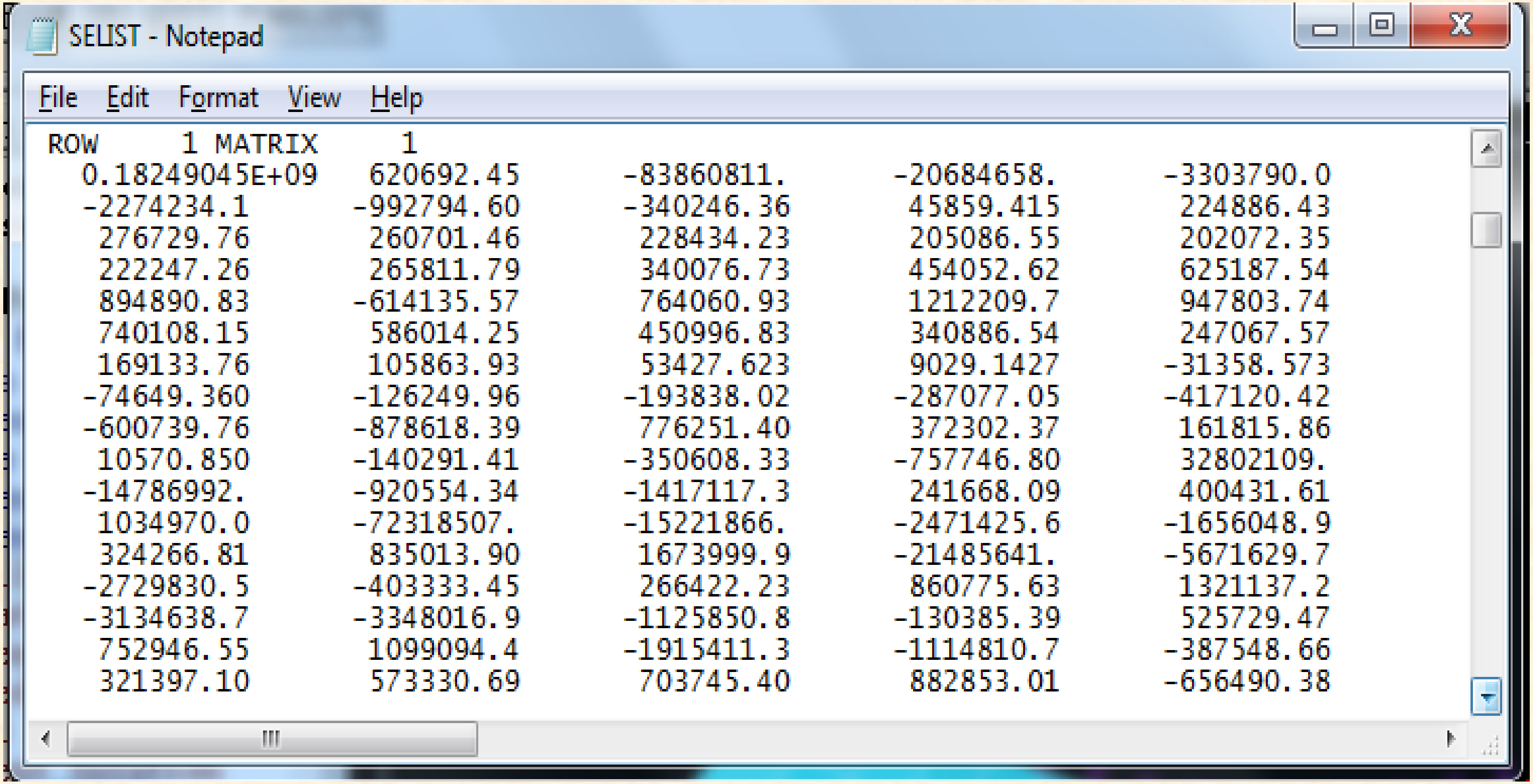

```
ROW      1 MATRIX      1
   0.18249045E+09   620692.45     -83860811.     -20684658.     -3303790.0
   -2274234.1      -992794.60     -340246.36      45859.415      224886.43
    276729.76       260701.46      228434.23      205086.55      202072.35
    222247.26       265811.79      340076.73      454052.62      625187.54
    894890.83      -614135.57      764060.93      1212209.7      947803.74
    740108.15       586014.25      450996.83      340886.54      247067.57
    169133.76       105863.93      53427.623      9029.1427     -31358.573
   -74649.360      -126249.96     -193838.02     -287077.05     -417120.42
   -600739.76      -878618.39      776251.40      372302.37      161815.86
    10570.850      -140291.41     -350608.33     -757746.80      32802109.
   -14786992.      -920554.34     -1417117.3      241668.09      400431.61
    1034970.0      -72318507.     -15221866.     -2471425.6     -1656048.9
    324266.81       835013.90      1673999.9     -21485641.     -5671629.7
   -2729830.5      -403333.45      266422.23      860775.63      1321137.2
   -3134638.7      -3348016.9     -1125850.8     -130385.39      525729.47
    752946.55       1099094.4     -1915411.3     -1114810.7     -387548.66
    321397.10       573330.69      703745.40      882853.01     -656490.38
```

CONCLUSIONS

Accurate characterization of mechanical components presently requires of physical models of ever increasing complexity that include all relevant geometrical aspects, material properties and fluid flow conditions, as per installation and operation, even envisioning operation well beyond their intended original design. This paper extends a computational thin film fluid flow model for tilting pad journal bearings to include both pivot flexibility and pad flexibility on the prediction of the static and dynamic forced performance of typical bearings. Presently, a FE structural commercial model builds the stiffness matrix for pad displacements, further reduced to show only the pad surface deformations due to an applied pressure field. The deformation field is integrated into the evaluation of film thickness for solution of the Reynolds equation delivering the hydrodynamic pressure field. A small amplitude perturbation analysis produces equations for the zeroth and first-order pressure fields from which the load capacity and a multitude of complex stiffnesses coefficients for each pad are determined. A pad assembly with frequency reduction method delivers the 4x4 complex dynamic stiffnesses for lateral or radial displacements of the shaft center. Curve fits of the force/displacement frequency functions delivers the bearing stiffness, damping and force coefficients.

In a parallel program, Gaines [1] performed measurements for three-pad LBP TPJBs. Pad thickness varied to change the pad flexibility. Gaines' test data show that pad flexibility affects little the journal eccentricity and maximum pad temperature, but has an impact on the bearing dynamic force coefficients. Current model predictions for the TPJBs in Ref. [1] correlate favorably with test data, except that the maximum temperature rise is underestimated by up to 40%. The reason may be due to that the oil pushed through the supply holes is not routed efficiently into the bearing pads. Pad flexibility reduces the predicted journal eccentricity and maximum temperature rise.

The real part of the TPJB dynamic stiffnesses (Z) at super-synchronous frequency ($\omega>\Omega$) shows a hardening effect, yet it is nearly constant for frequencies lesser that the shaft angular speed, $\omega<\Omega$. Hence, the virtual mass coefficients identified with a [K-C-

M] model are negative. However, the predicted virtual mass coefficients only affect the dynamic stiffnesses at a high frequency (ω>Ω). The imaginary part of the complex stiffnesses (Z) increases linearly with frequency. However, at 6 krpm (100 Hz), Im(Z) show a decrease at a high frequency (ω>180 Hz).

In general, both the experimental and predicted dynamic force coefficients reduce due to pad flexibility. Pad flexibility causes up to a 20% reduction in predicted bearing stiffness. However, Gaines [1] reports an increase in bearing direct stiffnesses for the TPJB with the more flexible pad. Predicted bearing stiffnesses also show a slightly increase at a low load ($W/(LD)$<689 kPa) due to pad flexibility but decrease at a high load (>689 kPa).

Pad flexibility shows a more significant effect on the predicted dynamic force coefficients than the experimental results evidence, in particular at a high rotor speed (Ω=12 krpm), thus indicating the pad structural FE model delivers a smaller stiffness than that of the actual test pad. Measurements for the stiffness of the pads are needed to further improve the FE model. Predictions including pad flexibility deliver damping coefficients up to 46% lower than those obtained with a rigid pads model. Reducing the pad thickness from 11.5 mm to 8.5 mm causes also a reduction of up to 50% in predicted direct damping.

The paper also includes a parametric study to quantify the influence of pad thickness on the rotordynamic force coefficients of a sample TPJB with three pads of increasing preload=0, 0.25 (baseline) and 0.5. The bearing pads varies from rigid to flexible (k_{pad} = ∞, 3.15 and 7.33). Graphs for journal eccentricity, drag friction coefficient, and dimensionless force coefficients are presented versus Sommerfeld number (0.2<S<2.2). The operating journal eccentricity and the dynamic force coefficients of a TPJB reduce due to pad flexibility, in particular for operation at a large Sommerfeld number (S>0.8). Pad flexibility shows a more pronounced effect for the TPJB with null pad preload.

REFERENCES

[1] Gaines, J., 2014, “Examining the Impact of Pad Flexibility on the Rotordynamic Coefficients of Rocker-Pivot-Pad Tiling-Pad Journal Bearings,” MS. Thesis, Mechanical Engineering, Texas A&M University, College Station, TX.

[2] Nicholas, J.C., Gunter, F.J., and Allaire, P.E., 1979, “Stiffness and Damping Coefficients for the Five-Pad Tilting-Pad Bearing,” ASLE Trans., **22**, pp.113-124.

[3] Rodriguez, L.E. and Childs, D.W., 2006, “Frequency Dependency of Measured and Predicted Rotordynamic Coefficients for a Load-on-Pad Flexible-Pivot Tilting-Pad Bearing,” ASME J. Trib., **128**, pp. 388-395.

[4] Delgado, A., Vannini, G., Ertas, B., Drexel, M. and Naldi, L., 2011, “Identification and Prediction of Force Coefficients in a Five-Pad and Four-Pad Tilting Pad Bearing for Load-on-Pad and Load-Between-Pad Configurations,” ASME J. Eng. Gas Turbines Power, **133**, 092503 1-9.

[5] Carter, C., and Childs, D.W., 2009, “Measurements versus Predictions for the Rotordynamic Characteristics of a Five-Pad Rocker-Pivot Tilting-Pad Bearing in Load- Between-Pad Configuration,” ASME, J. Eng. Gas Turbines Power, **131**, 012507 1-9.

[6] Wilkes, J. C., 2011, “Measured and Predicted Rotor-Pad Transfer Functions for a Rocker-Pivot Tilting-Pad Bearing,” PhD. Thesis, Mechanical Engineering, Texas A&M University, College Station, TX.

[7] Wilkes, J.C., and Childs, D.W., 2012, “Tilting Pad Journal Bearings – a Discussion on Stability Calculation, Frequency Dependence, and Pad and Pivot Flexibility,” ASME J. Eng. Gas Turbines Power, **134**, p. 122508.

[8] San Andrés, L., and Tao, Y., 2013, “The Role of Pivot Stiffness on the Dynamic Force Coefficients of Tilting Pad Journal Bearings,” ASME J. Eng. Gas Turbines Power, **135**, pp. 112505.

[9] San Andrés, L., Tao, Y., and Li, Y., 2014, “Tilting Pad Journal Bearing: On Bridging the Hot Gap Between Experimental Results and Model Predictions,” ASME J. Eng. Gas Turbines Power, **137**, pp.022505.

[10] Nilsson, L., 1978, "The Influence of Bearing Flexibility on the Dynamic Performance of Radial Oil Film Bearings," Proc. 5th Leeds-Lyon Symposium on Tribology, **5**, pp.311-319.

[11] Ettles, C.M., 1980, "The Analysis and Performance of Pivoted Pad Journal Bearings Considering Thermal and Elastic Effects," ASME J. Lubr. Technol., **102**, pp. 182-192.

[12] Lund, J.W. and Pedersen, L.B. 1987, "The Influence of Pad Flexibility on the Dynamic Coefficients of a Tilting Pad Journal Bearing," ASME J. Tribol., **109**, pp. 65-70.

[13] Brugier, D. and Pascal, M.T., 1989, "Influence of Elastic Deformations of Turbo-Generator Tilting Pad Bearings on the Static Behavior and on the Dynamic Coefficients in Different Designs," ASME J. Tribol., **111**, pp. 364-371.

[14] Desbordes. H., Fillon, M., Frene, J. and Chan Hew Wai, C., 1995, "The Effects of Three Dimensional Pad Deformations on Tilting-Pad Journal Bearings under Dynamic Loading," ASME J. Tribol., **117**, pp. 379-384.

[15] Earles, L.L., Palazzolo, A.B. and Armentrout, R.W., 1990 "A Finite Element Approach to Pad Flexibility in Tilt Pad Journal Bearings: Part I – Single Pad Analysis," ASME J. Tribol., **112**, pp. 169-177.

[16] Earles, L.L., Palazzolo, A.B. and Armentrout, R.W., 1990 "A Finite Element Approach to Pad Flexibility in Tilt Pad Journal Bearings: Part II – Assembled Bearing and System Analysis," ASME J. Tribol., **112**, pp. 178-182.

[17] Gaines, J., and Childs, D., 2015, 'The Impact of Pad Flexibility on the Rotordynamic Coefficients of Tilting pad Journal Bearings," ASME Paper No.GT2015-42289, Proc. of the 60th International Gas Turbine, Turbo-Expo Conference, June 15-19, Montreal, Canada (in review).

[18] San Andrés, L., 2010, "Note 16. Analysis of Tilting Pad Bearings," Modern Lubrication Theory, Texas A&M University Digital Libraries, http://repository.tamu.edu/handle/1969.1/93256

[19] San Andrés, L., 2006, "Hybrid Flexure Pivot-Tilting Pad Gas Bearings: Analysis

and Experimental Validation," ASME J. Tribol., **128**, pp.551-558.

[20] Tao, Y., 2012, "A Novel Computational Model for Tilting Pad Journal Bearings with Soft Pivot Stiffnesses," MS. Thesis, Mechanical Engineering, Texas A&M University, College Station, TX.

[21] ASM Handbook, 1990, *Properties and Selection: Nonferrous Alloys and Special-Purpose Materials*, 10th ed., ASM International, Materials Park, OH, pp. 517-526.

[22] Cverna, F., 2002, *ASM Ready Reference: Thermal Properties of Metals*, ASM International, Materials Park, OH, Chapt.2.

[23] Childs, D.W., Delgado, A., and Vannini, G., 2011, "Tilting-Pad Bearings: Measured Frequency Characteristics of their Rotordynamic Coefficients," Proc. 40th Turbomachinery Symposium, September 12-15, Houston, TX.

[24] Someya, T., 1989, "Journal-Bearing Databook," Springer-Verlag, Berlin, Heidelberg, Chap. 1.

[25] Branagan, L.A., 1988, "Thermal Analysis of Fixed and Tilting Pad Journal Bearing Including Cross-Film Viscosity Variations and Deformation," Ph.D. Diss., University of Virginia, Charlottesville, VA.

[26] Gere, J.M., 2013, *Mechanics of Materials*, Cengage Learning, Stamford, Chap.6.

[27] Kassimali, A., 1999, *Structural Analysis*, PWS Pub. Pacific Grove, Chap. 7.

[28] Timoshenko, S., and Goodier, J.N., 1951, *Theory of Elasticity*, McGraw-Hill, New York, Chap.6.

[29] Armenakas, A.E., 2005, *Advanced Mechanics of Materials and Applied Elasticity*, CRC Press, Chap.13.

[30] Reddy, J. N., 2002, *Energy Principles and Variational Methods in Applied Mechanics*, John Wiley & Sons, New York, Chap.5.

[31] Li, Y., 2015, "A Computational Model for Tilting Pad Journal Bearings with Pad Flexibility," M.S. Thesis, Mechanical Engineering, Texas A&M University, College Station, TX.

APPENDIX A. HIRS TURBULENT FLOW MODEL

XLTPJB© uses a laminar flow model to predict the static and dynamic performance of TPJBs. However, turbulent flow may occur in bearings operating at high rotational speeds, especially for bearings of large size, or with a lubricant of low viscosity [A.1]. The turbulent flow model based on Hirs [A.2] is introduced into the predictive model.

According to Ref. [A.3], the fully developed turbulent bulk-flow equations in a thin film are the

Continuity equation:

$$\frac{\partial}{\partial x}\left(hV_x\right)+\frac{\partial}{\partial z}\left(hV_z\right)+\frac{\partial h}{\partial t}=0 \tag{A.1}$$

Circumferential momentum equation:

$$-h\frac{\partial P}{\partial x}=\frac{\mu}{h}\left(\kappa_x V_x-\kappa_J\frac{U}{2}\right)+\rho\frac{\partial\left(hV_x\right)}{\partial t} \tag{A.2}$$

Axial momentum equation:

$$-h\frac{\partial P}{\partial z}=\frac{\mu}{h}\kappa_z V_z+\rho\frac{\partial\left(hV_z\right)}{\partial t} \tag{A.3}$$

where $V_x=\frac{1}{h}\int_0^h \bar{u}dy$ and $V_z=\frac{1}{h}\int_0^h \bar{w}dy$ are bulk flow velocities. $\kappa_J=f_J R_J$, $\kappa_B=f_B R_B$ and $\kappa_x=\kappa_z=\frac{1}{2}\left(\kappa_J+\kappa_B\right)$ are bulk flow turbulence shear parameters. For laminar flows, $\kappa_x=\kappa_z=\kappa_J=\kappa_B=12$. Above, *h* and *P* denote the film thickness and pressure, respectively, and U=ΩR is the journal surface velocity. Note equations (A.2-3) include temporal fluid inertia terms only, with the advection terms omitted.

Substituting the momentum Eqs.(A.2, A.3) into the continuity Eq.(A.1) gives

$$\begin{aligned}\frac{\partial}{\partial x}\left\{\frac{h^3}{\kappa_x\mu_{(T)}}\frac{\partial P}{\partial x}\right\}+\frac{\partial}{\partial z}\left\{\frac{h^3}{\kappa_z\mu_{(T)}}\frac{\partial P}{\partial z}\right\}=\frac{\partial h}{\partial t}+\frac{\Omega}{2}\frac{\partial}{\partial\theta}\left(\frac{\kappa_J}{\kappa_x}h\right)\\-\left\{\frac{\rho h^2}{\kappa_x\mu_{(T)}}\frac{\partial^2 h}{\partial x\partial t}+\frac{\rho h^2}{\kappa_z\mu_{(T)}}\frac{\partial^2 h}{\partial z\partial t}+\frac{\partial\left(hV_x\right)}{\partial t}\frac{\partial}{\partial x}\left(\frac{\rho h^2}{\kappa_x\mu_{(T)}}\right)+\frac{\partial\left(hV_z\right)}{\partial t}\frac{\partial}{\partial z}\left(\frac{\rho h^2}{\kappa_z\mu_{(T)}}\right)\right\}\end{aligned} \tag{A.4}$$

Taking the time derivative of the continuity Eq.(A.1) gives

$$\frac{\partial^2}{\partial t \partial x}\left(hV_x\right)+\frac{\partial^2}{\partial t \partial z}\left(hV_z\right)+\frac{\partial^2 h}{\partial t^2}=0 \tag{A.5}$$

Assume $\kappa_x=\kappa_z=\kappa$. Substituting Eq. (A.5) into Eq.(A.4) yields a Reynolds equation for turbulent flow with temporal fluid inertia effects.

$$\frac{1}{R_J{}^2}\frac{\partial}{\partial\theta}\left\{\frac{h^3}{\kappa\,\mu_{(T)}}\frac{\partial P}{\partial\theta}\right\}+\frac{\partial}{\partial z}\left\{\frac{h^3}{\kappa\,\mu_{(T)}}\frac{\partial P}{\partial z}\right\}=\frac{\partial h}{\partial t}+\frac{\Omega}{2}\frac{\partial h}{\partial\theta}+\frac{\rho h^2}{\kappa\,\mu_{(T)}}\frac{\partial^2 h}{\partial t^2} \tag{A.6}$$

The turbulence shear parameters are

$$\kappa_x=\kappa_z=\kappa=(\kappa_J+\kappa_B)/2 \tag{A.7}$$

According to Refs. [A.3, A.4], κ_J and κ_B are determined from

$$\kappa_i=\begin{cases}12 & \mathrm{Re}_i<1{,}000\\ \dfrac{12}{\mathrm{Re}_i}\left[1-\left(\dfrac{\mathrm{Re}_i-1000}{20000}\right)^2\left(3-2\cdot R_i\right)\right]+f_i\cdot\left(\dfrac{\mathrm{Re}_i-1000}{20000}\right)^2\left(3-2\cdot R_i\right) & 1{,}000\le\mathrm{Re}_i<3{,}000\\ f_i\,\mathrm{Re}_i & \mathrm{Re}_i>3{,}000\end{cases} \tag{A.8}$$

over the flow regimes from laminar, to transition, to fully developed turbulence. Above, $f_i=0.001375\left[1+\left(\dfrac{5\cdot10^5}{\mathrm{Re}_i}\right)^{\frac{1}{3}}\right]$ is Moody's friction factor, and i=J (journal) or B (bearing) surfaces. The bulk-flow Reynolds numbers (Re_i) relative to the bearing (B) and journal (J) surfaces are:

$$\mathrm{Re}_J=\frac{\rho h}{\mu}\left[\left(V_x-\Omega R\right)^2+V_z^2\right]^{\frac{1}{2}},\ \mathrm{Re}_B=\frac{\rho h}{\mu}\left[V_x^2+V_z^2\right]^{\frac{1}{2}} \tag{A.9}$$

The bulk flow thermal energy transport equation with turbulent flow is [A.3]

$$C_p\left[\frac{\partial(\rho HUT)}{\partial x}+\frac{\partial(\rho HWT)}{\partial z}\right]+Q_s=H\frac{\Omega R}{2}\frac{\partial P}{\partial x}+\frac{\mu}{H}\left[\kappa_x\left(U^2+W^2+\frac{\Omega R}{2}U\right)+\kappa_J\Omega R\left(\frac{\Omega R}{4}-U\right)\right] \tag{A.10}$$

Note the drag torque is obtained from

$$T_{Torque}=\iint\left\{\frac{h}{2}\frac{\partial P}{\partial x}+\frac{\kappa_J}{4}\frac{\mu}{h}\Omega R\right\}R\,dx\,dy \tag{A.11}$$

Predictions from the implemented turbulent flow model are compared against the test data and predictions of Taniguchi *et al*. [A.5] collected for a large size four-pad TPJB used in a steam turbine. Ref. [A.5] adopts the turbulent flow model by Ng and Pan [A.6]. Table A.1 lists the geometry and lubricant properties of the test TPJB and Figure A.1 shows a schematic view of the four-pad bearing.

Table A.1 Geometry and lubricant properties of the test TPJB in Ref [A.5]

Rotor diameter, D	479 mm
Pad axial length, L	300 mm
Pad arc angle, θ_P	80°
Pivot offset	0.5
Pad clearance, C_B	612 µm
Pad preload	0
Pad mass, m_p	119 kg
Pad inertia, I_P	2.74 kg.m^2
Lubricant type	**ISO VG32**
Supply lubricant temperature, T_{in}	~40°C
Supply lubricant pressure	1 bar
Lubricant density, ρ	856.2 kg/m^3
Viscosity at 40°C, μ_0	0.0274 Pa·s
Viscosity temperature coefficient, α	0.0296 1/°C
Specific heat capacity at 40 °C	1950.7 J/(kg·K)
Journal speed, Ω	3000 rpm
Surface speed, ΩR	75.24 m/s
Unit load, $W/(LD)$	1,252 kPa
Average shear Reynolds number[6], Re	2,043

---

[6] $\mathrm{Re}=\rho\Omega R C_B/\mu_{average}$ with $\mu_{average}$ is the lubricant viscosity at the average temperature in the fluid film.

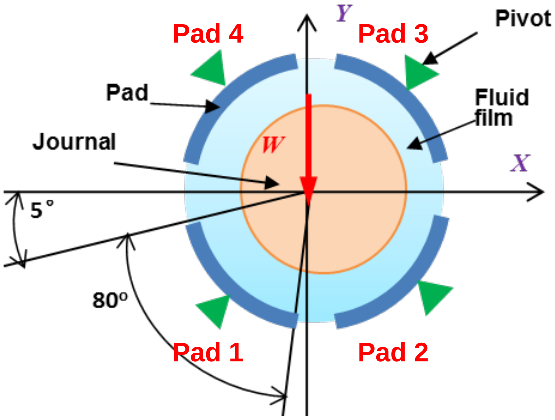

Figure A.1 Schematic view of large four-pad TPJB in Ref [A.5]

Note that the current model predictions do not account for either pivot or pad flexibility, as also in the model stated in Ref. [A.5]. The clearance is assumed constant, not affected by an increase in temperature, to keep consistancy with Ref. [A.5]. The journal and bearing surfaces are taken as adiabatic. The inlet heat carry over coefficient (λ) is 0.8. The average shear Reynolds number (Re=2,043) is higher than 2,000, thus indicating a turbulent flow condition.

Figure A.2 shows the fluid film thickness at the mid-plane of the loaded two pads (#1 and #2). The current predictions and those from [A.5] agree with each other, albeit lower than the test results by 19% at the pad inlet, and correlating well for the magnitude of the minimum film thickness.

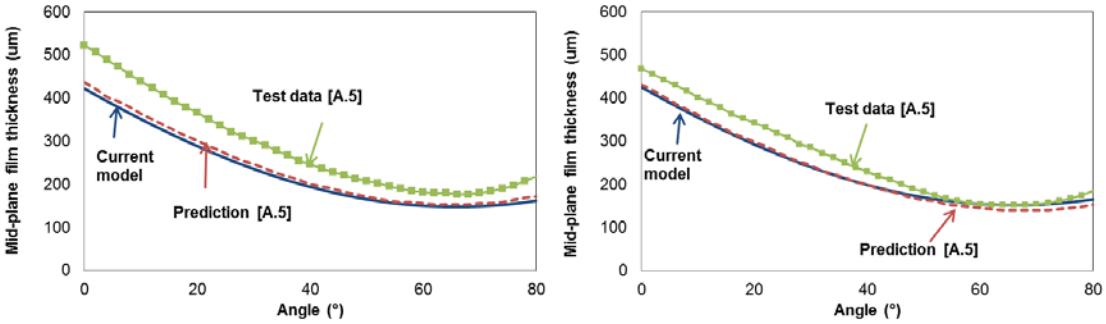

(a) Pad 1 (b) Pad 2

Figure A.2 Film thickness at mid-plane of pads #1 and #2. Current predictions and results in Ref. [A.5]. ***W*/(*LD*)=1,252 kPa,Ω=3 krpm, average Re=2,043.**

Figure A.3 shows the pressure profile at the mid-plane of the loaded pads (#1 and #2). The current predictions give pressure profiles similar to those predicted in Ref. [A.5]. Note the models ignore the pressure rise at the pad inlet due to an entrance fluid inertia effect.

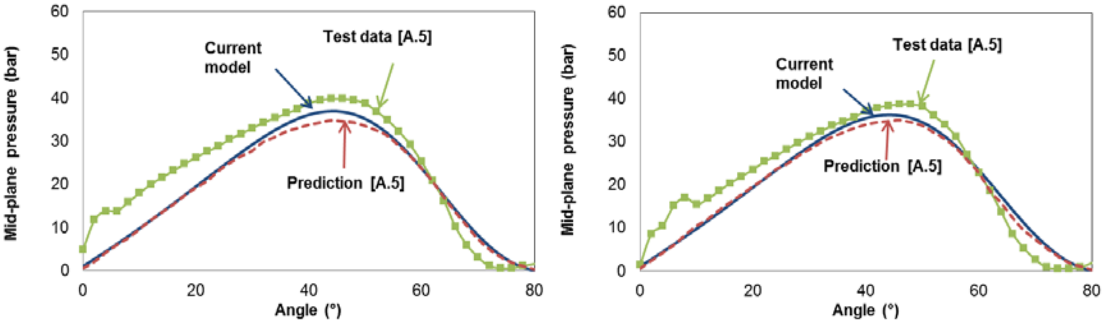

(a) Pad 1 (b) Pad 2

Figure A.3 Pressure profile at the mid-plane of pads #1 and #2. Current predictions and results in Ref. [A.5]. ***W*/(*LD*)=1,252 kPa,Ω=3 krpm, average Re=2,043.**

Figure A.4 depicts the temperature at the mid-plane of the loaded pads (#1 and #2). The current predictions and the data in Ref. [A.5] show good agreement at the pads' leading edges. However, at the pads' trailing edges, the current model delivers a temperature lower than the measured one and the predicted results in Ref. [A.5]. The current model takes a bulk temperature across the film whereas the measurement is obtained at 3 mm under a pad surface.

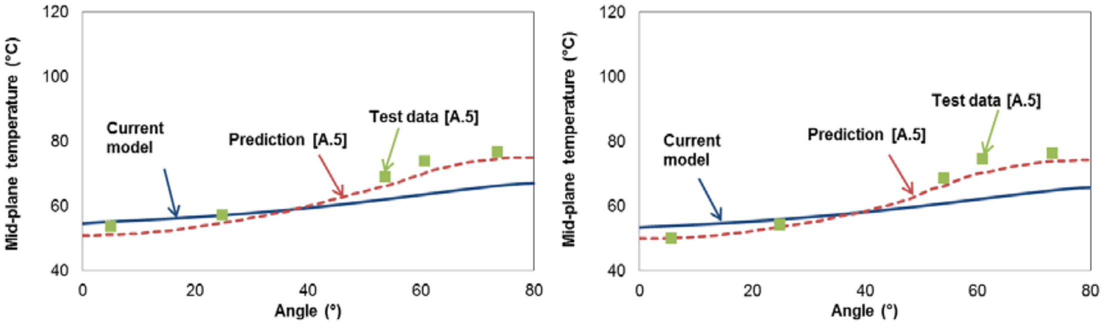

(a) Pad 1 (b) Pad 2

Figure A.4 Temperature at the mid-plane of pads #1 and #2. Current predictions and results in Ref. [A.5]. ***W*/(*LD*)=1,252 kPa,Ω=3 krpm, average Re=2,043.**

Figure A.5 depicts the drag power loss predicted by the current model and those in Ref. [A.5]. For rotor speeds from 1,200 rpm to 3,800 rpm, the predicted power loss agrees with the data in Ref. [A.5]. However, for shaft speeds above 3,800 rpm, the current model overestimates slightly the drag power loss. Note that during its operation, the thin film flow in the bearing is laminar (Re<1,000) for rotor speeds below 2,900 rpm, in the transition flow regime for rotor speeds from 2,900 rpm to 3,700 rpm, and fully turbulent above 3,700 rpm.

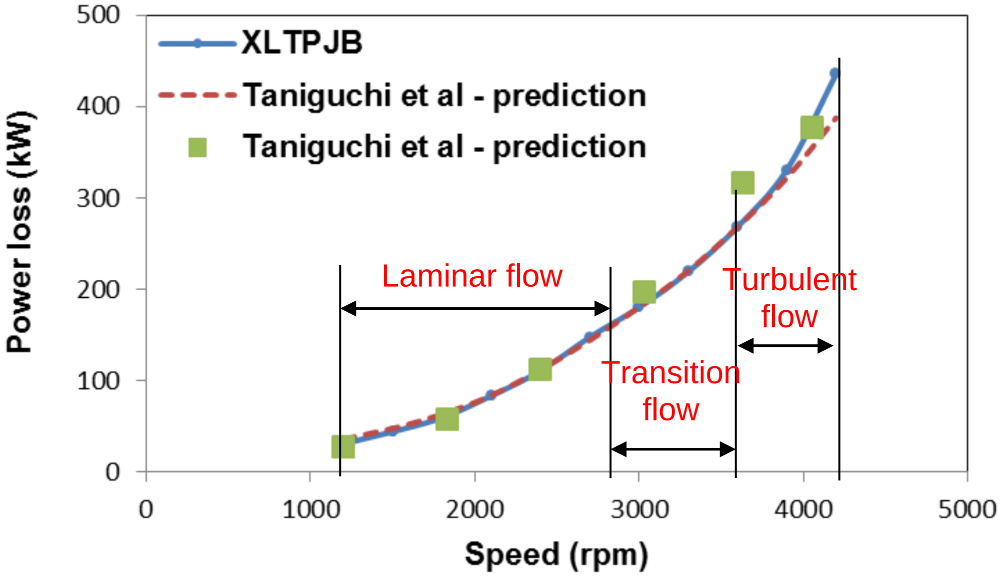

Figure A.5 Bearing friction loss at *W*/(*LD*)=1,252 kPa. Speed varing 1200 rpm to 4200 rpm. Current predictions and results in Ref. [A.5]. average Re from 1201 to 4774.

References:

[A.1] Constantinescu, V.N., 1962, “Analysis of Bearings Operating in Turbulent Regime,” ASME J. Basic. Eng., **85,** pp. 139-156.

[A.2] Hirs, G.G., 1973, “A Bulk-Flow Theory for Turbulence in Lubricant Films,” ASME. J. Tribol., **96**, pp.134-145

[A.3] San Andrés, L., 2009, “Notes 08. Turbulent Flow in Thin Film Bearings: Characteristics and Modeling,” Modern Lubrication Theory, Texas A&M University Digital Libraries, http://repository.tamu.edu//handle/1969.1/93248.

[A.4] Szeri, A.Z., 2011, *Fluid Film Lubrication*, Cambridge University Press.

[A.5] Taniguchi, S., Makino, T., Takeshita, K., and Ichimura, T., “A Thermohydrodynamic Analysis of Large Tilting-Pad Journal Bearing in Laminar and Turbulent Flow Regimes With Mixing,” ASME. J. Tribol., **112**, pp.542-548

[A.6] Ng, C.W., and Pan, C.H.T., 1964, “A Linearized Turbulent Lubrication Theory,” ASME J. Basic. Eng., **87**, pp. 675-688.

APPENDIX B. A MODEL FOR BEARING LINER DEFORMATION

As the external load increases, the fluid film in a hydrodynamic bearing becomes thinner, thus producing an increase in fluid temperature that reduces the oil viscosity, thus further decreasing the oil film thickness [B.1]. Conventional hydrodynamic bearings commonly adopt Babbitt (white metal) as a liner material to protect the surfaces of rotors while ensuring low friction. Though the Babbitt liner provides good conformability and embedability, it loses strength with a raise in temperature, and has a high breakaway friction [B.1]. As a substitute for Babbitt, PTFE (polytetrafluoroethylene) shows better performance at high temperatures with a low breakaway friction [B.2]. However, the high flexibility of PTFE affects the static and dynamic forced performance of a fluid film bearing. Thus, a predictive model for bearings with a PTFE liner should account for its deformation.

The elastic radial deformation (δ) of a liner due to pressure is approximated as a plane strain problem [B.1-B.4],

$$\delta = \frac{s\left(P - P_a\right)}{E} \frac{\left(1+\nu\right)\left(1-2\nu\right)}{1-\nu} \tag{B.1}$$

where P is the hydrodynamic pressure, P_a is the ambient pressure, and s is the thickness of the liner. E and ν denote the elastic modulus and the Poisson's ratio for the liner material, respectively.

Ref. [B.1] also considers the thermal expansion (ΔR) of the liner into account, as

$$\Delta R = -\alpha\, s\, (T - T_a) \tag{B.2}$$

where α is the thermal expansion coefficient of the liner, T is the linear surface temperature and T_a is the ambient temperature. The simple thermal expansion Eq. (B.2) is implemented into the current model as a change in bearing or pad clearance.

Kuznetsov *et al.* [B.1] analyze the effect of liner flexibility on the static performance of a plain journal bearing. Table B.1 lists the geometry and lubrication properties of the bearing in Ref. [B.1], and Figure B.1 shows a schematic view of the plain journal bearing.

Table B.1 Parameters of a plain journal bearing in Ref. [B.1]

Rotor diameter, *D*	198.5 mm
Bearing length, *L*	200 mm
Bearing cold clearance, *C*	237 μm
Bearing supply groove width	29.22°
Supply oil temperature	65°C
Oil viscosity (at 40°C)	0.033 Pa.s
Oil viscosity (at 100°C)	0.0056 Pa.s
Oil density	864.7 kg/m^3
Oil heat capacity	2008.5 J/(kg.K)
Oil thermal conductivity	0.13 W/(mK)
Unit load, *W*/(*LD*)	504-6,297 kPa
Journal speed	900 rpm

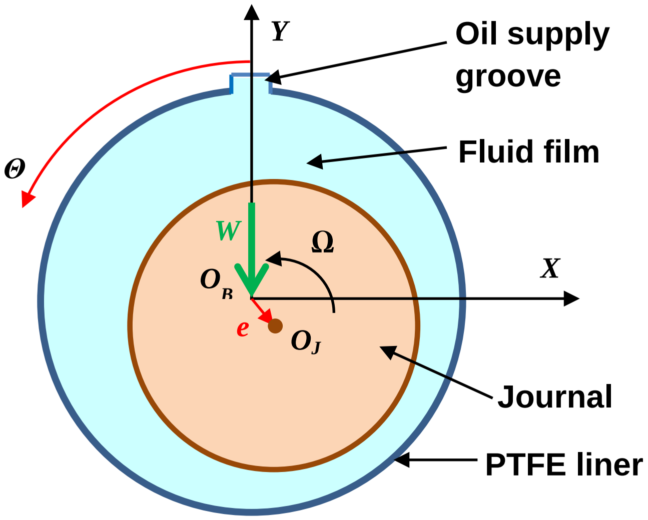

Figure B.1 Schematic view of plain journal bearing with a liner, as per Ref. [B.1]

Table B.2 lists the properties of the PTFE liner. Note that Ref. [B.1] does not inform on the ambient temperature. The current predictions assume the ambient temperature (T_a) to equal the the supply temperature 65°C.

Table B.2 PTFE liner properties in Ref. [B.1].

Elastic modulus, E	0.11 GPa
Poisson ratio, v	0.46
thickness, s	2 mm
thermal expansion coefficient, α	1.35×10^{-4} K^{-1}

Ref. [B.1] also accounts for the thermal expansion of the shaft and bearing housing. Current predictive model offers a function to estimate the thermal expansion of the shaft as well. The equation to estimate the thermal expansion of the shaft is

$$\Delta R = -\alpha_{shaft} R\,(T_{shaft} - T_a) \qquad \text{(B.3)}$$

where α_{shaft} is the thermal expansion coefficient of the shaft, T_{shaft} is the temperature in shaft, and R is the shaft radius. In the current predictions, α_{shaft} is 1.11×10^{-5} K^{-1} for a steel jounal.

Two cases are analyzed and predictions compared to the results in Ref. [B.1] (see Table B.3). Note that the deformation of the PTFE liner contains both the thermal expansion and mechanical deformation.

Table B.3 Cases to assess effect of liner flexibility on the performance of a plain journal bearing.

Case 1	Bearing with rigid liner
Case 2	Bearing with PTFE liner

Figure B.2 shows the fluid film thickness predicted by the current model for a 122 kN static load applied on the bearing ($W/(LD)$=3,073 kPa). For both cases (rigid bearing and bearing with PTFE liner), the fluid film thickness predicted by the current model correlates well with that presented in Ref. [B.1]. The flexibility of PTFE liner tends to reduce the film thickness.

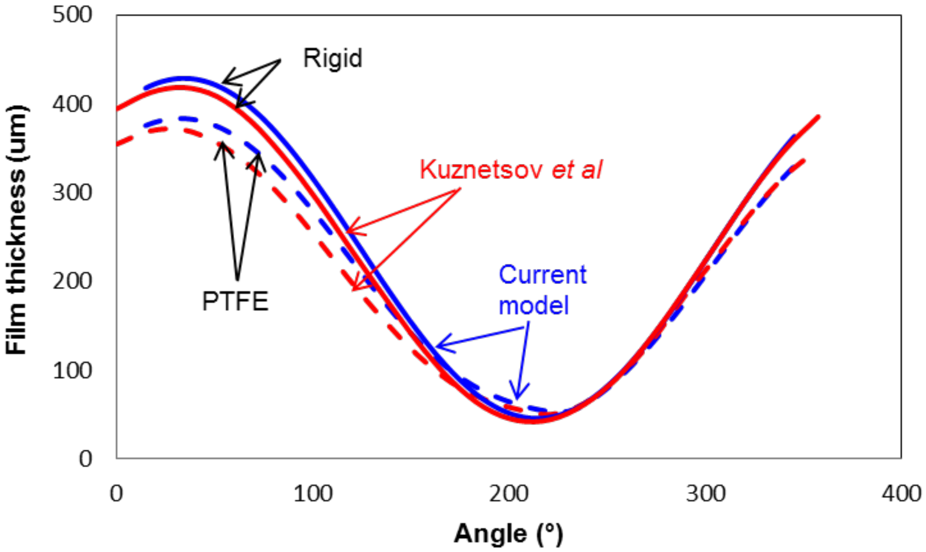

Figure B.2 Fluid film thickness at the bearing mid-plane. Static load *W*/(*LD*)=3,073 kPa, rotor speed Ω=900 rpm. Current predictions and data from Ref. [B.1].

Figure B.3 shows the fluid film pressure at the bearing mid-plane; the current predictions show good correlation with those in Ref [B.1]. For a rigid bearing, the current model predicts a larger peak pressure. The peak fluid film pressure including the elasticity of the PTFE liner is 27% smaller than that assuming a rigid liner.

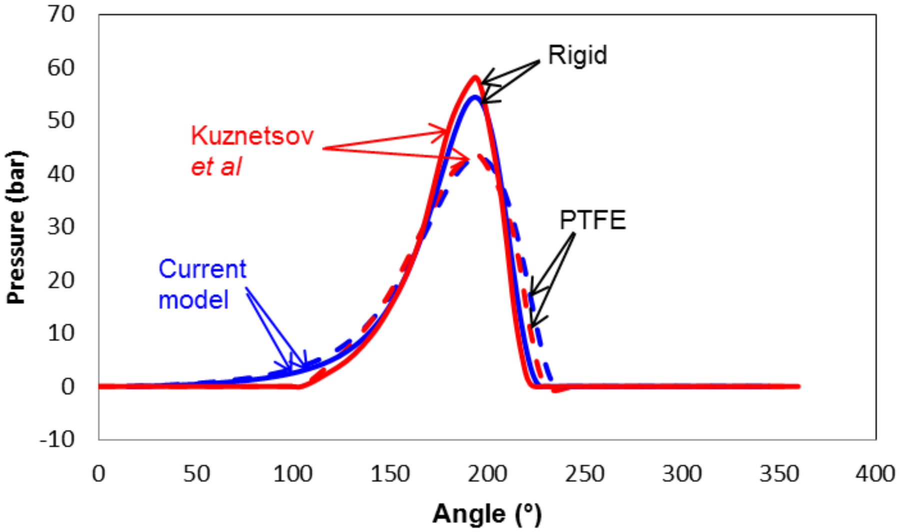

Figure B.3 Fluid film pressure at the bearing mid-plane. Static load *W*/(*LD*)=3,073 kPa, rotor speed Ω=900 rpm. Current predictions and data from Ref. [B.1].

Figure B.4 depicts the maximum pressure, minimum fluid film thickness and eccentricity ratio versus unit load. The current predictions of maximum pressure and minimum fluid film thickness show good agreement with the results in Ref.[B.1]. The current model delivers a larger eccentricity ratio (=eccentricity/cold clearance) than that in Ref. [B.1]. The current predictions for the maximum temperature correlate well with the data in Ref. [B.1] at a low loads, $W/(LD)$<2.5 MPa; but are larger at high loads, $W/(LD)$>4 MPa. The PTFE liner tends to reduce the maximum film pressure and journal eccentricity ratio. The effect of PTFE liner flexibility (with thickness s=2 mm) on the minimum film thickness and maximum temperature is not significant.

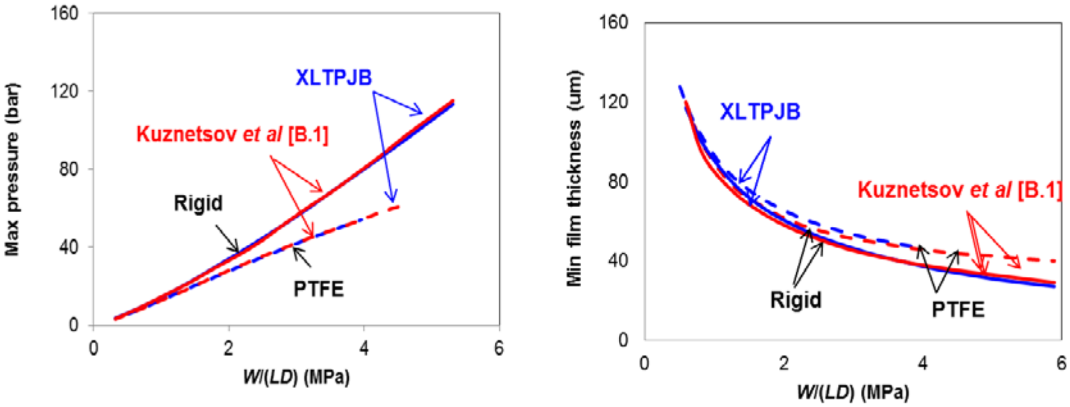

(a) maximum pressure **(b) minimum film thickness**

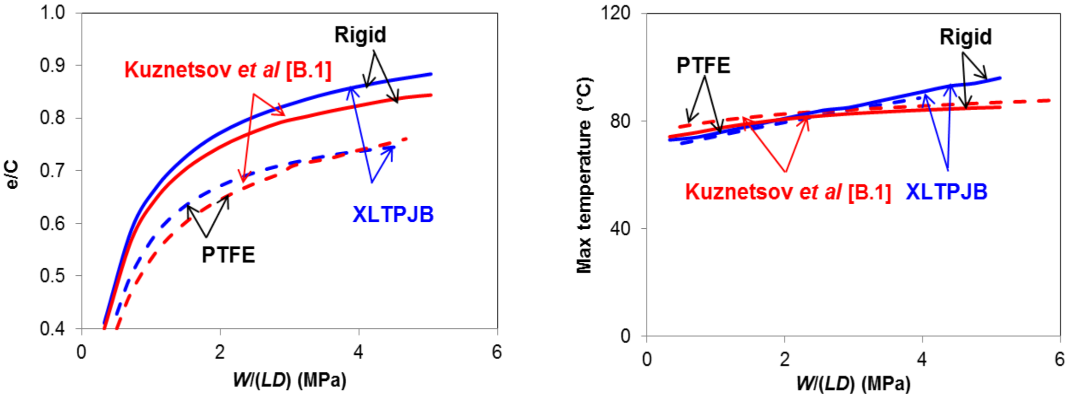

(c) eccentricity ratio (e/C) **(d) maximum temperature**

Figure B.4 (a) Maximum pressure, (b) minimum fluid film thickness and (c) eccentricity ratio and (d) maximum temperature at different load. 504 kPa<$W/(LD)$<6,297 kPa. Ω=900rpm. Current predictions and data from Ref. [B.1].

References:

[B.1] Kuznetsov, E., Glavatskih, S., and Fillon, M., 2011, "THD Analysis of Compliant Journal Bearings Considering Liner Deformation," Tribology International, **44**, pp.1629-1641

[B.2] Golchin, A., Simmons, G.F., and Glavatskih, S.B., 2012, "Beark-away Friction of PTFE Materials in Lubricated Conditions," Tribology International, **48**, pp.54-62.

[B.3] Conway, H.D., and Lee, H.C., 1975, "The analysis of the lubrication of a flexible journal bearing," ASME J. Lubr. Tech., **97**, pp. 599-604

[B.4] Jain, S.C., Sinhasan, R., and Singh, D.V., 1982, "The Performance Characteristics of Thin Compliant Shell Journal Bearings," Wear, **81**, pp.251-261

[B.5] Zhang, M., Zhang, G., and Liu, Z., 2013, "Study on Dynamic Characteristics of Large Ship Rotor-Bearing System Based on an Advanced Water-Lubricated Rubber Bearing Model," Proceedings of the ASME Turbo Expo 2013, Paper GT2013-94901, June 3-7, San Antonio, USA